Smart Additive Manufacturing Using Advanced Data Analytics and Closed Loop Control

Chenang Liu

Dissertation submitted to the faculty of the Virginia Polytechnic Institute and State University in partial fulfillment of the requirements for the degree of

Doctor of Philosophy
In
Industrial and Systems Engineering

Zhenyu (James) Kong, Chair
Navid Ghaffarzadegan
Haibo Zeng
Xiaoyu (Rayne) Zheng

06/20/2019

Blacksburg, VA

Keywords: Additive manufacturing, online quality assurance, data analytics, spectral graph theory, manifold learning, bilateral time series model, closed-loop control

Smart Additive Manufacturing Using Advanced Data Analytics and Closed Loop Control

Chenang Liu

ABSTRACT

Additive manufacturing (AM) is a powerful emerging technology for fabrication of components with complex geometries using a variety of materials. However, despite promising potential, due to the complexity of the process dynamics, how to ensure product quality and consistency of AM parts efficiently during the process still remains challenging. Therefore, the objective of this dissertation is to develop effective methodologies for online automatic quality monitoring and improvement, i.e., to build a basis for smart additive manufacturing.

The fast-growing sensor technology can easily generate a massive amount of real-time process data, which provides excellent opportunities to address the barriers of online quality assurance in AM through data-driven perspectives. Although this direction is very promising, the online sensing data typically have high dimensionality and complex inherent structure, which causes the tasks of real-time data-driven analytics and decision-making to be very challenging.

To address these challenges, multiple data-driven approaches have been developed in this dissertation to achieve effective feature extraction, process modeling, and closed-loop quality control. These methods are successfully validated by a typical AM process, namely, fused filament fabrication (FFF). Specifically, four new methodologies are proposed and developed as listed below,

(1) To capture the variation of hidden patterns in sensor signals, a feature extraction approach based on spectral graph theory is developed for defect detection in online quality monitoring of

AM. The most informative feature is extracted and integrated with a statistical control chart, which can effectively detect the anomalies caused by cyber-physical attack.

(2) To understand the underlying structure of high dimensional sensor data, an effective dimension reduction method based on an integrated manifold learning approach termed multi-kernel metric learning embedded isometric feature mapping (MKML-ISOMAP) is proposed for online process monitoring and defect diagnosis of AM. Based on the proposed method, process defects can be accurately identified by supervised classification algorithms.

(3) To quantify the layer-wise quality correlation in AM by taking into consideration of reheating effects, a novel bilateral time series modeling approach termed extended autoregressive (EAR) model is proposed, which successfully correlates the quality characteristics of the current layer with not only past but also future layers. The resulting model is able to online predict the defects in a layer-wise manner.

(4) To achieve online defect mitigation for AM process, a closed-loop quality control system is implemented using an image analysis-based proportional-integral-derivative (PID) controller, which can mitigate the defects by adaptively adjusting machine parameters during the printing process in a timely manner.

By fully utilizing the online sensor data with innovative data analytics and closed-loop control approaches, the above-proposed methodologies are expected to have excellent performance in online quality assurance for AM. In addition, these methodologies are inherently integrated into a generic framework. Thus, they can be easily transformed for applications in other advanced manufacturing processes.

Smart Additive Manufacturing Using Advanced Data Analytics and Closed Loop Control

Chenang Liu

GENERAL AUDIENCE ABSTRACT

Additive manufacturing (AM) technology is rapidly changing the industry; and online sensor-based data analytics is one of the most effective enabling techniques to further improve AM product quality. The objective of this dissertation is to develop methodologies for online quality assurance of AM processes using sensor technology, advanced data analytics, and closed-loop control. It aims to build a basis for the implementation of smart additive manufacturing.

The proposed new methodologies in this dissertation are focused to address the quality issues in AM through effective feature extraction, advanced statistical modeling, and closed-loop control. To validate their effectiveness and efficiency, a widely used AM process, namely, fused filament fabrication (FFF), is selected as the experimental platform for testing and validation. The results demonstrate that the proposed methods are very promising to detect and mitigate quality defects during AM operations.

Consequently, with the research outcome in this dissertation, our capability of online defect detection, diagnosis, and mitigation for the AM process is significantly improved. However, the future applications of the accomplished work in this dissertation are not just limited to AM. The developed generic methodological framework can be further extended to many other types of advanced manufacturing processes.

ACKNOWLEDGEMENTS

I would like to gratefully acknowledge and thank my advisor, Dr. Zhenyu (James) Kong, for his guidance and supervision. I have learned a lot from him and I am so lucky to have such a great professor as my advisor. Without his help and support, I could not accomplish my dissertation work with good quality. I also thank my wonderful Ph.D. advisory committee members, Dr. Navid Ghaffarzadegan, Dr. Haibo Zeng, and Dr. Xiaoyu (Rayne) Zheng, for their valuable advice and constant support with my research.

During my graduate study, I have also received lots of help and encouragement from many other individuals. Particularly, I would like to thank my fellow lab members, Dr. Kaveh Bastani, Dr. Jia Liu, Mr. David Roberson, Mr. Andrew Law, Mr. Rongxuan Wang, Mr. Jihoon Chung, and Mr. Bo Shen, for their selfless friendship, help, and unconditional support.

Very importantly, I must thank all my family members, for their constant love and support throughout over these years, although most time I cannot physically be with them. I love them very much.

Finally, I also wish to acknowledge my department, Grado Department of Industrial and Systems Engineering. It is a great and delightful experience for me to study and work with every person in the department.

Table of Contents

List of Figures

List of Tables

1 Introduction

1.1 Background and motivation

Additive manufacturing (AM), also called 3D printing, refers to a family of processes where a bulk shape is formed by progressively adding material in the form of layers [1]. This layer-by-layer addition of material leads to revolutionary design flexibility and applications. As one of the fastest growing emerging technologies, AM provides powerful solutions in a large variety of industrial areas, such as aerospace, automotive industry, healthcare, etc. [2-4]. Nowadays there are various technologies which can implement AM using different kinds of materials, such as fused filament fabrication (FFF), selective laser sintering (SLS), stereolithography (SLA), etc. [5, 6]. With the rapid development of these innovative AM processes, more and more complex geometric structures with advanced materials can be fabricated [7, 8].

Despite the enormous development achieved in AM so far, to consistently produce high-quality products using AM still remains challenging. Consequently, although with promising potential, the relatively poor quality and inconsistency of AM parts may hinder their broader applications in some mission critical industries where the product quality is very essential. Thus, it is imperative to develop new techniques for online process monitoring and quality assurance of AM.

The traditional quality monitoring approaches, such as geometric dimensioning and tolerancing (GD&T) and other surface metrology techniques, are primarily applied for offline quality inspections [9, 10]. This is not sufficient for quality assurance of AM. Online quality control for AM becomes necessary since it is very quick and can also avoid failure of products. The rapid development of high resolution and fast frame rate of sensor technologies in recent decades offers

new research opportunities to address the challenges in online quality assurance by providing rich data to enable data-driven perspectives. Through instrumentation of online sensors, massive real-time data from AM operations are easily available for in-depth analysis. For example, we may install heterogeneous sensors such as thermocouples and accelerometers to collect the data for process variables, and utilize some image-based sensing devices such as cameras and 3D scanners to inspect the quality status of printing parts. Due to the high dimensionality and complex inherent structure of sensor data, it is challenging to extract the most valuable information and make optimal decisions therein. Therefore, how to create an effective methodological framework to analyze and understand sensor data plays a critical role in successful implementation of online quality assurance of AM.

1.2 Research objectives

As mentioned in Section 1.1, AM process complexity poses a great challenge for process monitoring and product quality assurance. Thus it is difficult to directly apply traditional quality monitoring methods for AM applications. Therefore, the overall research goal of this dissertation is to develop enabling methods for smart AM systems that can detect, diagnose, and mitigate the product defect automatically during printing. More specifically, the above goal consists of four research objectives regarding sensor data analytics and online decision making and control in AM,

(1) **Online defect detection:** If unexpected defects/anomalies occurred during AM processes, how to detect the defects timely and effectively?

(2) **Online defect diagnosis:** Using sensor data captured curing AM processes, how to extract the most effective information regarding the types of process/part defects in a real time manner?

(3) **Online defect forecasting:** How to model the complex layer-wise interaction in AM and further forecast the layer-wise defects (quality characteristics) in an online manner?

(4) **Online defect mitigation:** Once detects are detected and diagnosed during AM processes, then how to adjust the machine parameter automatically and mitigate the defects efficiently using closed-loop control?

By achieving these four objectives, the contribution of this dissertation work can be summarized as the following four aspects,

(1) First, this work builds a novel framework to recognize the variation of hidden patterns in sensor signals for defects/anomalies detection based on a data-driven feature extraction approach using spectral graph theory.

(2) Second, it provides effective solutions for online defect diagnosis of AM, which are based on a proposed new dimension reduction approach.

(3) Third, an innovative bilateral time series modeling approach is developed for online layer-wise quality/defect forecasting which takes a unique physical phenomenon in AM called reheating into consideration.

(4) Finally yet importantly, an effective online closed-loop quality control approach is developed to implement online process adjustment and defect mitigation.

These developed methods are not limited to one specific type of AM process. In practice, they also have great potential to be applied to other advanced manufacturing processes with online sensor technologies.

1.3 Dissertation organization

The rest of this dissertation is organized as follows. An overview of the overall proposed research methodologies and a brief review of the recent related literature as well as a research gap analysis are provided in Chapter 2. Then Chapter 3 presents the proposed data-driven spectral feature extraction approach to identify the variation of hidden patterns in sensor signals for online defect detection. In Chapter 4, an integrated manifold learning-based dimension reduction method to understand the underlying structure of high dimensional sensor data is developed for online defect diagnosis of AM. Afterwards, a new bilateral time series modeling approach for online layer-wise defect/quality forecasting of AM with the consideration of reheating effects is proposed in Chapter 5. Subsequently, an image analysis-based closed-loop quality control approach for online defect mitigation is introduced in Chapter 6. Finally, Chapter 7 summarizes the contribution of the research, and expresses the potential future research directions.

2 Research overview and literature review

2.1 Research overview

As introduced in Chapter 1, this dissertation aims to build a basis for smart AM which is able to achieve online process monitoring and quality improvement using online sensor data. Therefore, as shown in Figure 2-1, the proposed research methodologies are focused on creating an effective and efficient methodological framework which integrates online sensing, advanced data analytics and closed-loop control techniques. In this research framework, the instrumented online sensing system provides a large amount of real-time process data. Subsequently, several advanced data analytics methods are developed to extract the compact but effective information from the sensor data, and correlate it with AM product quality. Afterwards, closed-loop control techniques are implemented to make decisions timely and effectively for defect mitigation.

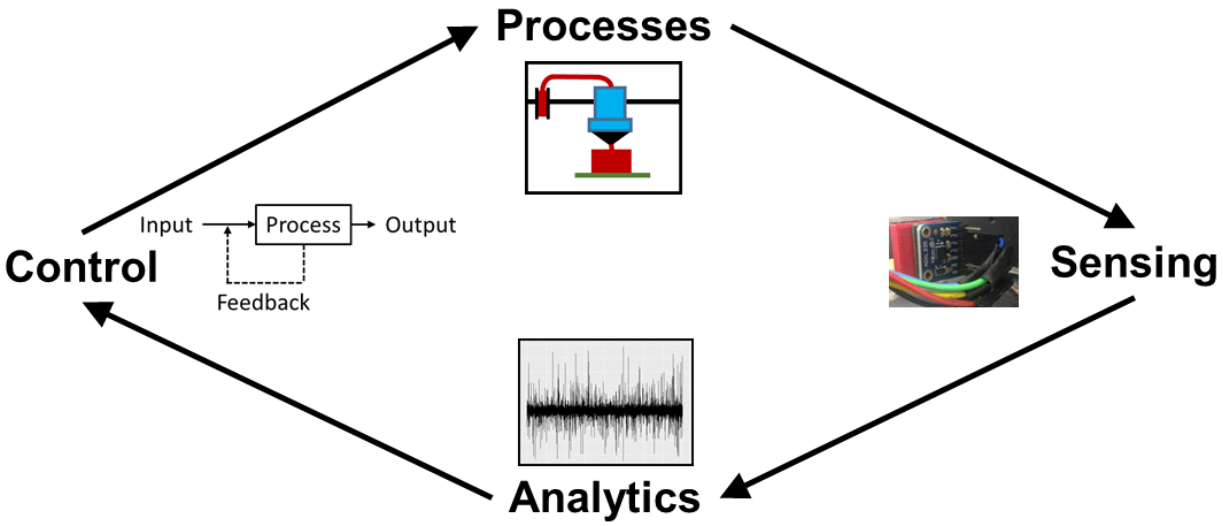

Figure 2-1: The overview of the proposed research framework.

Following this framework, the overall research in this dissertation consists of four specific tasks, as shown in Figure 2-2.

- **Task 1:** For the sensor data, develop a data-driven feature extraction approach using spectral graph theory that is integrated with statistical control charting techniques to implement online anomaly detection for AM (Chapter 3).
- **Task 2:** Achieve effective feature extraction from the high dimensional online sensing data to diagnose the defects occurring during the AM process based on a proposed new integrated manifold learning approach (Chapter 4).
- **Task 3:** Based on the reheat effects in AM, quantify the layer-wise correlation of quality characteristics with an implementation of online defect/quality forecasting framework, which considers the reheating phenomenon through a proposed bilateral time series modeling approach (Chapter 5).
- **Task 4:** Based on image analysis for defect detection, develop an online closed-loop quality control approach to implement automatic defect mitigation during the printing process (Chapter 6).

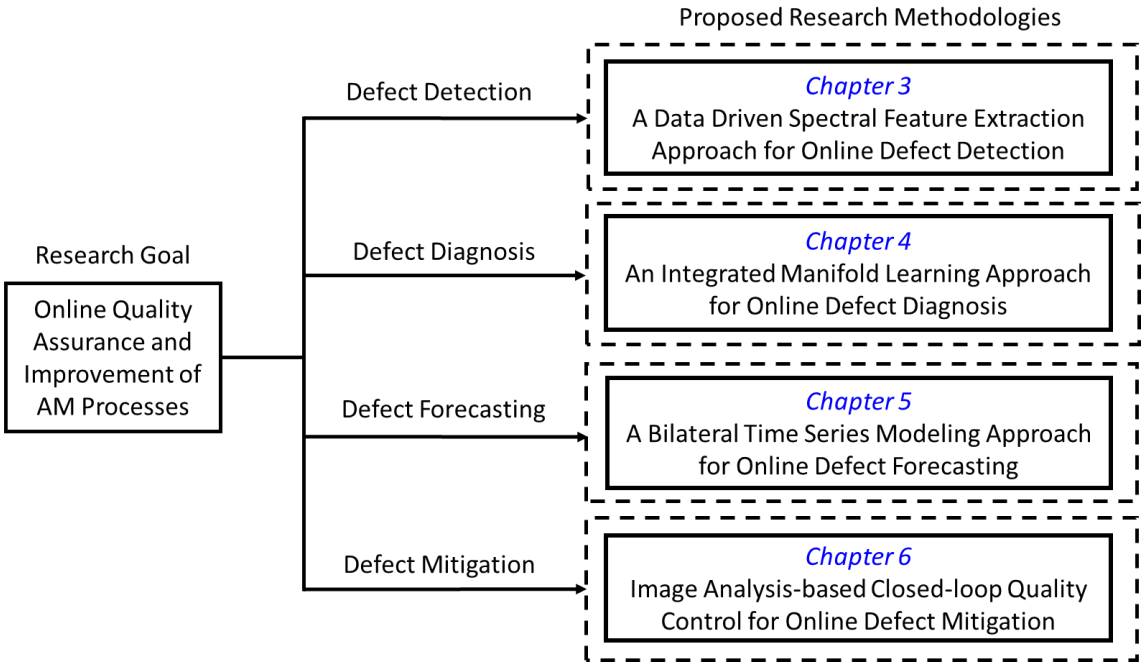

Figure 2-2: The overall structure of the proposed research methodologies in this dissertation.

With these four research tasks, three major online sensing systems are developed and utilized in this dissertation research:

(1) A combination of heterogeneous sensors (including vibration, temperature, IR sensor, etc.);

(2) High-resolution digital microscopes-based real-time image acquisition system;

(3) A high-speed digital 3D scanner for online layer-wise surface scanning.

By exploring the data collected from these sensors, innovative data analytics methods and statistical models are developed in this dissertation to achieve online quality assurance and process improvement in AM.

2.2 Literature review

This research is motivated by the online quality assurance of AM processes using advanced data analytics. Therefore, this section first introduces the related studies on online sensing and process monitoring for AM processes in Section 2.2.1, followed by a brief review of the data analytics and statistical modeling based quality assurance approaches for AM and other related applications in Section 2.2.2. Subsequently, Section 2.2.3 presents the existing experimental studies for analysis of AM product quality. At the end, the shortcomings in the current literature are identified in Section 2.3.

2.2.1 Online sensing for monitoring of AM processes

Online sensing-based process monitoring approaches for AM have been studied in the recent years. In terms of sensing strategies, the existing research works in this direction can be categorized into the three broad areas as follows.

(1) *Multi-sensor integration.* During AM processes, multiple sensor measurements such as

thermal and displacement may be directly related to the actual printing quality [11]. Following this direction, how to integrate multiple sensors for AM process online monitoring has been studied. Tapia *et al.* [12] reviewed the existing sensor-based process monitoring approaches for metal AM processes, such as temperature sensors and displacement sensors, etc., which are capable to monitor other common AM processes as well. Recently, more advanced online sensing approaches were investigated. For instance, by using acoustic emission sensor, Wu *et al.* [13] proposed an *in situ* monitoring framework for FFF to identify both normal and abnormal states of the printing conditions. In addition, Kousiatza *et al.* [14] investigated an approach to monitor the strain and temperature distributions of FFF by an integrated fiber Bragg grating (FBG) sensing system. Regarding heterogeneous sensing systems, Rao *et al.* [15] developed an effective method to achieve online real-time process monitoring for FFF, based on the combination of vibration sensors, thermocouples, and IR sensors. In addition, for metal-based AM, Dunbar *et al.* [16] demonstrated the capability of measuring distortion and temperature measurements online using a differential variable reluctance transducer (DVRT) and thermocouple during the laser powder bed fusion (LPBF) process.

(2) *Thermal imaging-based sensing system.* Thermal variation is a critical physical phenomenon in most common AM processes. To achieve effective online process monitoring, infrared thermal cameras have been widely utilized in AM processes. Khanzadeh *et al.* [17] used a thermal camera to capture the melt pool images and implement porosity monitoring in the directed energy deposition (DED) process. For the LPBF-based AM process, Mahmoudi *et al.* [18] applied high speed thermal imaging to capture melt pool temperature and implemented online layer-wise anomaly detection. In addition, Schwerdfeger *et al.* [19] demonstrated *in situ* capability to detect the flaws that are visible in images using an infra-red (IR) camera during a powder bed, beam-

based AM process. Grasso *et al.* [20] illustrated that the information from IR image is effective to detect possible flaws during *in situ* monitoring in the selective laser melting (SLM) process.

(3) *Optical imaging-based quality monitoring*. Apart from thermal imaging techniques, with the rapid development of optical sensing technologies, high resolution image-based online sensing has been explored for the monitoring of AM processes as well. For the applications in the FFF process (or the processes resembling FFF), Fang *et al.* [21] applied machine vision techniques to detect defects based on optical imaging of each layer; which can evaluate the geometrical integrity of the build via comparing the optical imaging result and its corresponding original CAD design. Fang *et al.* [22] further developed a related online signature analysis-based monitoring approach to detect the process anomalies. Cheng *et al.* [23] proposed an online approach to monitor the surface pattern by using image intensity information, and were able to classify the randomly occurring defects and anomalies from assignable causes. Subsequently, for metal AM, Craeghs *et al.* [24] implemented a real-time optical process monitoring system for the Layer-wise Laser Melting (LLM) process by instantaneously mapping the melt pool data with relative position on the printing plane. Kanko *et al.* [25] deployed a low-coherence interferometric imaging technique to achieve *in situ* surface defect detection of the SLM process. Grasso *et al.* [26] also develop an online defect detection method for SLM process via image analysis. Zhang *et al.* [27] customized an *in situ* fringe projection system, which combines the projector and camera of the LPBF process to monitor layer-by-layer surface quality.

2.2.2 Data analytics and statistical modeling for quality assurance of AM processes

As discussed in Section 2.1, development of advanced sensing systems for AM provides effective solutions to achieve better performance of online process monitoring. Meanwhile, it also provides great opportunities to develop more effective quality control strategies using data analytics-based

approaches. To achieve a highly accurate process quality diagnosis, Bastani *et al.* [28] developed an online sparse estimation-based classification approach to effectively identify different printing quality status. Khanzadeh *et al.* [29] proposed a tensor decomposition-based method to analyze the thermal image streams for process monitoring of a metal AM process. Using image profiles, Yao *et al.* [30] developed a multifractal analysis-based approach to detect defects in AM. In addition, for 3D point-cloud data. Law *et al.* [31] presented a curvature-based threshold method to achieve in process monitoring for the polymer-based powder bed fusion (PBF) process. Then in order to further improve the printing quality, Sun *et al.* [32] developed functional quantitative and qualitative models to quantify the correlation between machine parameters and online process variables in FFF. In addition, Liu *et al.* [33] proposed a layer-wise spatiotemporal modeling approach to predict porosity in a powder-based AM process.

Although currently the application of time series analysis-based modeling approaches for AM is very limited in the existing literature, it is a powerful option for online quality control and process forecasting [34]. As one of the most widely used time series models, ARIMA model-based methods are applied in a large variety of applications for process quality control and forecasting. In the applications of quality inspection and fault diagnosis, Yao *et al.* [35] developed a statistical pattern recognition algorithm based on an autoregressive (AR) model to achieve damage detection in civil structures. Lu *et al.* [36] implemented an autoregressive exogenous inputs (ARX) model-based method for structural damage diagnosis using time series analysis of vibration signals. For the control chart development, Jiang *et al.* [37] proposed a control chart based on an autoregressive moving average (ARMA) model. Vander Wiel [38] developed a process monitoring approach using an integrated moving average (IMA) model. Consider the high dimensional cases, in which Jarrett *et al.* [39] utilized the vector autoregressive (VAR) model to develop a new type of control

chart for multivariate auto-correlated processes. As another popular time series model, the GARCH model is also very effective for quality control. For example, Ord *et al.* [40] proposed a method to monitor processes with changing variances based on the GARCH model.

2.2.3 Experimental studies for product quality in AM

Surface defects are often observed during AM processes. Several experimental studies have been conducted to correlate surface defects with machine parameters or process variables. Wang *et al.* [41] proposed and experimentally validated a mathematical model for warp deformation in FFF parts. They identified the significance of process variables and machine parameters on the occurrences of surface defects, such as ambient chamber temperature, extruded temperature, layer thickness, deposition speed, geometric structure of the part, and tool path.

Anitha *et al.* [42] applied a robust design method to correlate certain process parameters with the surface roughness (i.e., Ra value) of a sample part. Process parameters such as road width, layer thickness, and extrusion speed are studied and the testing results are statistically significant. Agarwala *et al.* and Armillotta [43, 44] summarized that FFF errors may result from the material deposition rate, continuing start-stop sequence, shrinkage and residual stresses, warping [45], or nozzle clogging. The existing literatures also investigated the approaches of ensuring part quality by implementing error compensation of the extrusion path [46, 47], identifying the optimal build direction [48, 49], and considering trade-off between accuracy and completion time by adaptively adjusting the size of outer build layers [50, 51].

Peng *et al.* [11] examined the influence of the process variables in FFF that are focused in this dissertation research, including extrusion temperature, feed rate, and material flow rate, etc. They experimentally obtained appropriate temperature range of ABS material for the FFF process. In

addition, they also commented that part defects can be reduced when the ratio of feed rate and flow rate approaches one [11, 52].

2.3 Research gaps analysis

The related research work introduced in Section 2.2.1 is mainly focused on the sensing system design and utilization with anomaly detection for AM processes. However, the in-depth analysis for the collected real-time data is very limited, so that comprehensive online process monitoring and quality improvement analysis are still insufficient. Although the research efforts summarized in Section 2.2.2 have provided comprehensive foundation for quality control and assurance strategies in AM based on sensor data analytics, a key shortcoming is the lack of effective feature extraction and statistical modeling strategies to precisely capture the most critical information and process dynamics. Section 2.2.3 summarizes insights on multiple common quality issues in AM, but none of them are capable of online inspection and diagnosis. In addition, these existing studies do not take into consideration the strategies for online defect mitigation. Therefore, the proposed research methodologies in this dissertation seek to address these gaps by developing new advanced data analytics methodologies and quality control strategies.

3 A spectral feature extraction approach for online anomaly detection

Due to the process complexity of AM, most of the existing statistical quality control methods are not able to provide a timely and effective detection by using sensing signals directly when a process anomaly occurs. Therefore, the objective of this chapter is to develop an effective process anomaly detection method through feature extraction from sensor data. To achieve this objective, a data-driven feature extraction approach based on spectral graph theory is proposed for analysis of online sensing signals. Then the anomaly detection can be successfully achieved by integrating the extracted features with statistical control charting techniques. After the validation based on numerical simulation data, the proposed method is also applied to an actual AM platform for online cyber-physical attack detection. Both the simulation and real case study results demonstrate that the proposed method is superior for detecting the process anomalies over the traditional SPC methods.

3.1 Introduction

With the rapid development of advanced manufacturing technologies, products with complex geometric structures and new materials can be fabricated effectively and efficiently [53-55]. However, the unexpected process changes (i.e., anomalies) during manufacturing processes still always pose a significant threat for ensuring the quality of products. Therefore, it becomes more and more critical to achieve effective online process anomaly detection.

As a powerful technique for online process anomaly detection, statistical process control (SPC) charts [56] have very broad applications, including manufacturing process monitoring [57, 58],

production systems inspection [59], disease surveillance [60], environmental monitoring [61], etc. With the capability of online sensing technologies, a large variety of available control charts are able to provide effective solutions, such as X-bar chart, CUSUM chart, EWMA chart, etc. [62]. Although SPC techniques are very popular in the manufacturing industry, the traditional SPC methods typically require very strong assumptions regarding the statistical distributions of the in-control (IC) data [63], which significantly limit their effectiveness in some applications. In addition, another significant issue is that their capability to handle noisy and high dimensional data still needs to be improved.

For the applications of advanced manufacturing processes, e.g., additive manufacturing (AM), it is very common that the distribution of IC data is unknown or inappropriate to be described by an explicit parametric form, which may impact the performance of SPC charts. In addition, due to the complexity dynamics of the process, the online sensing data may have some hidden patterns. To detect the process anomaly, it is valuable to track the consistency of these patterns. However, the changes of these patterns may not result in significant mean shift or variance change in practice, hence it is challenging to detect a process anomaly by using the traditional SPC charts directly.

One typical example is the online process monitoring for AM processes. Based on the results from literature, multiple sensors can be mounted into the AM machine [15]. Then with supervised machine learning algorithms, the process quality condition can be identified effectively in a real-time manner [15, 28]. However, the sensor signals under normal printing status may also have different patterns due to the dynamic changes of printing path, i.e., hidden patterns. If the design of the printing parts changed but the printing process still remains normal, then the existing SPC or machine learning methods may not be able to detect the process change timely.

To address this challenge, the objective of this chapter is to develop an effective online anomaly detection approach through feature extraction and control charting to track the variation of sensor data patterns. Based on real-time sensor data acquisition, this objective is realized by a proposed spectral graph theory-based data-driven feature extraction and selection method. Through appropriate integration with a statistical control charting technique, this proposed method is able to overcome the aforementioned shortcomings in the existing traditional SPC and machine learning approaches for online process anomaly detection.

The rest of this chapter is organized as follows. The proposed methodology is presented in detail in Section 3.2; Sections 3.3 and 3.4 provide numerical examples and actual case studies from real-world applications, respectively, to demonstrate the effectiveness of the proposed method. Finally, the conclusion is provided in Section 3.5.

3.2 Research methodology

In this section, a data-driven spectral feature extraction-based online process anomaly detection method is proposed, which is suitable for the online sensing signals with hidden patterns. As shown in Figure 3-1, the overall framework of the proposed methodology consists of four steps: (1) Use graph to represent the sequential real-time sensor data (Section 3.2.1); (2) extract the topologic features to quantify the graph based on spectral graph theory (Section 3.2.2); (3) select the most effective and informative feature to describe the inherent patterns of sensor data (Section 3.2.3); and (4) integrate the selected feature with an appropriate SPC chart to detect process anomaly (Section 3.2.4).

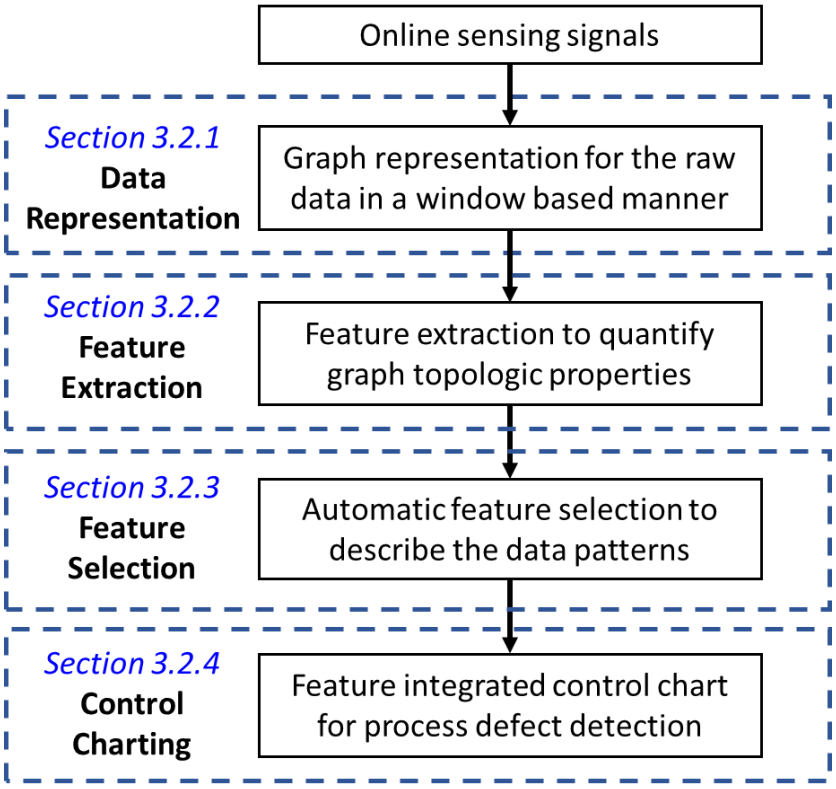

Figure 3-1: The overall research framework for the developed spectral feature extraction based online process defect detection approach.

3.2.1 Graph representation for real-time sensor data

As discussed in Section 3.1, this chapter is focused on process anomaly detection using online sensing signals. Typically the sensor data in the time domain can be represented by a time series $\{\mathbf{x}_t\}$, where t is the time index and $\mathbf{x}_t$ could be either a scalar for single sensor channel, or a column vector for multiple sensor channels. Assume all sensor channels have the same sampling frequencies. Pre-processing techniques such as up/down-sampling approaches [64] are potentially needed to relax this assumption in a general case.

Then the objective is to quantify the inherent pattern of $\{\mathbf{x}_t\}$ and monitor the real-time variability for anomaly detection. Since the proposed method is targeted for online application, a natural and

cost-effective choice is to analyze the sensor data sequentially in a window-based manner. Specifically, with a pre-defined window size, denoted as n, the sensing signals within each window can be represented as a row vector (single channel) or a matrix (multiple channels) defined by Eq. (3-1), and perform the analysis for each window sequentially.

$$\mathbf{X} = (\mathbf{x}_1, \mathbf{x}_2, \cdots, \mathbf{x}_n) \tag{3-1}$$

Subsequently, to quantify the inherent pattern of each window, the key is to capture the similarity between each pair of data points, i.e., to create a symmetric similarity matrix **S** with an appropriate distance metric. Specifically, **S** can be created by Eqs. (3-2) and (3-3),

$$d_{ij} = D(\mathbf{x}_i, \mathbf{x}_j) \tag{3-2}$$

$$\mathbf{S}^{n\times n} = [s_{ij}] = [d_{ij}] \tag{3-3}$$

where $D(\cdot)$ represents the operator to quantify the distance (i.e., similarity, [65]) between two data points. In general, the following three types of distance metrics are commonly used,

- Minkowski distance: This is a generalized metric defined in normed vector space which can be formulated as Eq. (3-4), where x_{ik} represents the kth element of $\mathbf{x}_i$. In order to satisfy the triangle inequality, typically it requires $p \geq 1$. In particular, when $p = 2$, the metric becomes Euclidean distance. In practice, to make the metric consistent with the intuition (the higher the similarity, the closer the two points), another common choice is to further convert the Euclidean distance by a kernel function such as the radial basis function (RBF) to describe the similarity [66, 67], as demonstrated in Eq. (3-5), which is applied in the simulation and actual case studies.

$$d_{ij} = ||\mathbf{x}_i - \mathbf{x}_j||_p = (\sum_{k=1}^{n} |x_{ik} - x_{jk}|^p)^{1/p} \tag{3-4}$$

$$d_{ij} = e^{-\left(\frac{||\mathbf{x}_i - \mathbf{x}_j||_2^2}{2\sigma^2}\right)} \tag{3-5}$$

- Cosine distance: This metric is to measure the degree of angle between two points (as shown in Eq.(3-6)). It is preferred to be applied when the magnitude between points does not matter but the orientation plays a critical role.

$$d_{ij} = \frac{\mathbf{x}_i \cdot \mathbf{x}_j}{||\mathbf{x}_i|| \cdot ||\mathbf{x}_j||} \tag{3-6}$$

- Mahalanobis distance: In this distance metric, from a statistical perspective, it considers the covariance matrix S into the measurement of similarity, which is represented as Eq. (3-7). In addition, several other types of statistical distance metrics also become popular in practice, such as Wasserstein distance [68], Cramér–von Mises distance [69], etc.

$$d_{ij} = \sqrt{(\mathbf{x}_i - \mathbf{x}_j)^T S^{-1} (\mathbf{x}_i - \mathbf{x}_j)} \tag{3-7}$$

Based on the similarity matrix built by a selected distance metric, then there is a unique undirected graph $G(V, E)$ to represent **S** without information loss. Specifically, V represents each data point as a node in G, and E is the edges with weight $\{d_{ij}\}$ to link the nodes. Afterwards, to further determine whether two nodes are connected or not, a threshold value r could be applied and then update the elements of **S**. Based on the similarity defined by Eq. (3-5) (selected in this study), this

transformation can be presented by Eq. (3-8). To determine the value of r, typically it can be set as the average of d_{ij} based on the existing studies with good performance [70, 71].

$$s_{ij} = \begin{cases} 1, \ d_{ij} \geq r \\ 0, d_{ij} < r \end{cases} \tag{3-8}$$

Therefore, using the above mentioned approach, the online sensor data $\{\mathbf{x}_t\}$ can be effectively represented as a series of unweighted undirected graphs in the time domain for analysis.

3.2.2 Graph topologic feature extraction

After mapping the time series sensor data to a series of graphs, the next step is to effectively quantify the properties of the graphs. Based on a created graph G, a commonly applied matrix representation for G called the Laplacian matrix (denoted as **L**) can be determined [72], which is applicable for both weighted and unweighted graphs. Then various in-depth analysis and inference can be further performed using the information in **L**. For example, clustering analysis (e.g., spectral clustering [73], etc.) and manifold learning (e.g. Laplacian embedding [74], etc.).

In this study, in order to detect the process changes using the graph representation, it is critical to find an effective quantification for the graph properties which is related to the process. Based on the spectral graph theory [72], the eigenvalues $\{\lambda_i\}$ (in an increased order, i.e., λ_i represents the ith smallest eigenvalue) of **L** (as shown in Eq. (3-9)), which contain the topological information of the graph, are utilized for further analysis (termed spectral features in this study).

$$\mathbf{L}\boldsymbol{v} = \lambda \boldsymbol{v} \tag{3-9}$$

Typically, the second smallest eigenvalue (λ_2) is termed the Fiedler number, also known as algebraic graph connectivity [75]. Although the application of the Fiedler number for online

process monitoring has been reported from several existing literatures [66, 67, 76], the limitation is that only using λ_2 for analysis may result in a significant information loss, since the Fiedler number could not always capture the effective inherent structure information of sensing signals. For example, if the signals within a window have more than two significant clusters, then λ_2 is always close to zero, which is ineffective to detect the potential process changes. In addition, another limitation is the lack of investigation for the underlying distribution of spectral features, which may impact the performance of anomaly detection.

On the other hand, it is also unnecessary to use all eigenvalues together for analysis, otherwise the monitoring effectiveness and computational efficiency will be significantly reduced due to the potential large amount of invalid and redundant information. Consequently, to find the most informative topologic representation from the spectral features, a clustering-based automatic feature selection method is proposed, which is presented in Section 3.2.3.

3.2.3 Clustering based feature selection

As introduced in Section 3.2.2, the eigenvalues $\{\lambda_i\}$ of the Laplacian matrix **L** is a group of features to quantify the graph topologic properties. However, with the high dimensionality of sensor data and large scale of the window size, it is usually impractical and unnecessary to apply all the features for online monitoring. Therefore, to determine the most effective and informative feature among the eigenvalues, a data-driven approach for automatic feature selection is presented in this section.

The motivation of this proposed approach is based on the fact that only a few spectral features are effective for process change detection. For example, considering a graph with several isolated nodes or separated clusters, then the value of λ_2 is just zero, regardless of the pattern of the major

part. In addition, with a relatively large number of nodes, typically there is no significant variation for most of the large eigenvalues when the graph pattern changes. Consequently, it is necessary to find the most effective topologic measurement among the eigenvalues.

Based on spectral graph theory, the topologic properties described by $\{\lambda_i\}$ are highly related to the graph clustering effect and connectivity [72]. Theoretically, the number of zero eigenvalues indicates the number of individual (i.e., not connected) clusters. In practice, since some clusters may be still connected, the number of relatively small eigenvalues is more appropriate to represent the cluster numbers in a graph. Therefore, to select the informative spectral feature in a quantitative way, the number of clusters should be identified first. Inspired by the spectral clustering method [73], it can be determined by finding the maximum value of the Eigengaps $\{\Delta\lambda_i\}$, which is defined by Eq. (3-10),

$$\Delta\lambda_i = \lambda_{i+1} - \lambda_i \tag{3-10}$$

As demonstrated in Figure 3-2, based on the maximum Eigengap $\Delta\lambda_k$, the value of k is able to represent the cluster numbers of the data, and then the corresponding eigenvalue λ_k is an effective topologic measurement (i.e., the connectivity) for the graph to quantify the pattern of data. Specifically, if the data have a trend to merge together, then λ_k will become larger since the connectivity is increasing; on the contrary, if the trend is to split the data into more clusters or even new clusters come in, then λ_k will decrease due to the lower connectivity. Consequently, λ_k is informative in general for the application of online anomaly detection (described in Section 3.2.4). The only special case is $\lambda_k = 0$. For example, if $k = 1$, since λ_1 is always 0, then λ_2 (the Fiedler number) will be used instead of λ_1. The main reason is that the change of data patterns in this case

will result in the change of overall graph connectivity. In general, if $\lambda_k = 0$, which implies that the graph has k independent unconnected clusters, then λ_{k+1} will be selected instead of λ_k.

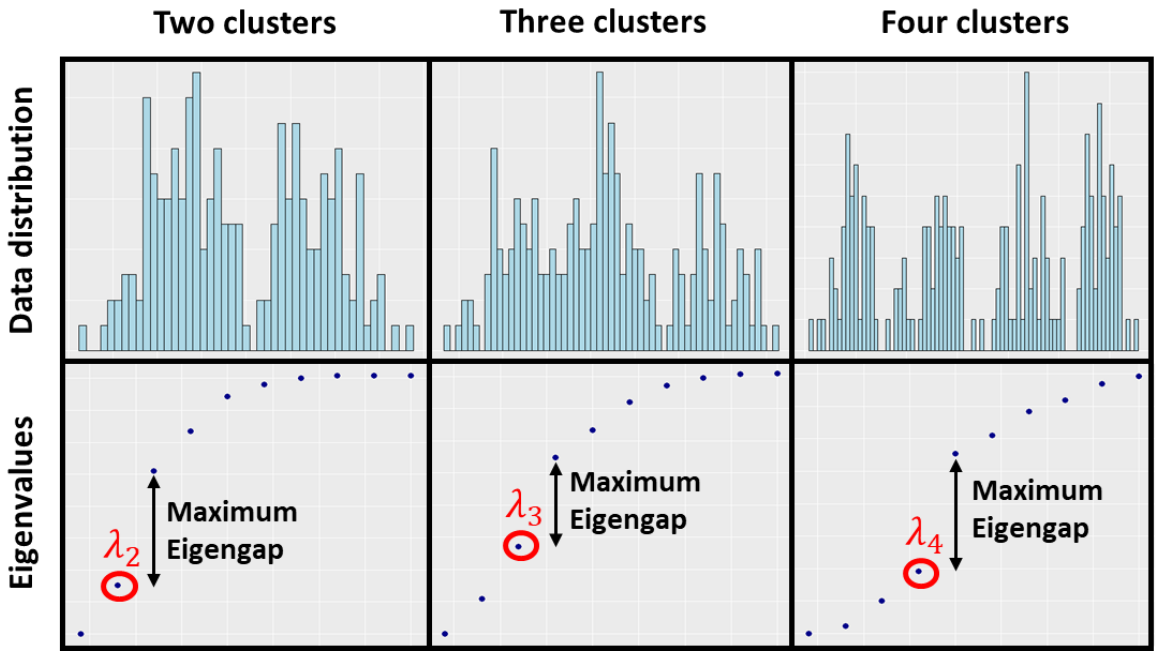

Figure 3-2: A justification of the proposed spectral feature selection approach based on the maximum Eigengap.

3.2.4 Design of control chart for process anomaly detection

To achieve online process anomaly detection, a natural direction is to integrate the selected spectral features with an appropriate statistical control chart. However, the challenge is that the underlying distribution of the selected feature is actually unknown and difficult to be quantified. To address this challenge, a developed control chart embedding approach is presented in this section, which consists of three steps.

(1) Determine the monitoring statistics: The statistics to be monitored by control chart should be identified first. In this study, to track the variation of the underlying distribution, two monitoring statistics are utilized based on the selected spectral feature.

i. Mean value of the selected spectral feature: It is necessary to detect the existence of mean shift for the selected λ_k. In this case, the EWMA chart could be applied since it is sensitive for small shifts [62] and also relatively robust for the non-Gaussian data based on several existing studies [77, 78]. Theoretically, the selected λ_k represents the graph connectivity by considering the clustering effect. Then in practice, the mean shift of λ_k indicates the change of cluster numbers, which is validated in the simulation study (Section 3.3).

ii. Quantile-based statistics: Apart from tracking the mean shift, it is also needed to monitor other changes regarding the underlying distribution of λ_k. To detect the small but critical anomalies such as cyber-physical attacks, this part is mainly focused on the change of distribution tails for λ_k. In statistics, the quantile function is commonly applied to describe the probability distribution and its tails [79], for example, the application of risk management in the finance area [80, 81], etc. Therefore, a quantile-based statistic for process monitoring is developed in this study. Specifically, a pre-defined quantile level (e.g., 80%) should be determined at first, and then the corresponding quantile value for the entire phase I data will be treated as a threshold for analysis. Afterwards, by using a window-based approach for the feature series, the number of features that fall outside of the quantile value (i.e., threshold) within each window will be counted as monitoring statistics. Since window size is consistent, this monitoring statistic is equivalent to evaluating the heaviness of the distribution tail. The effectiveness of this developed statistic is validated in the real-world case study (Section 3.4).

(2) Build a control chart: Based on the above determined monitoring statistics, the next step is to identify the baseline and control limits, which are the key components of a control chart. Typically, a well investigated control chart can be applied directly. To monitor the mean-shift of λ_k, the family of EWMA chart or CUSUM chart is able to handle. Then for the monitoring of the proposed quantile-based statistics, p chart or np chart related approaches [82]are appropriate to be applied. Then the control chart performance could be evaluated by the in control and out of control testing data.

(3) Optimize chart and define control rules: In general, a control chart usually has several input parameters. For example, if a EWMA chart is selected, it is critical to find an appropriate exponential weight λ [62]. Then the control rules [62] should be defined in a good way as well based on the specific real-world problems. In practice, the strategies to optimize parameters and define control rules are usually in terms of making a balance between false alarms and missed detection rate.

By these three steps for online application, the process anomaly can be detected in a timely manner based on the alarm from the control chart. In addition, to further improve the performance, more evolved advanced techniques in data analytics, such as Neural Networks [83, 84], ensemble learning methods [85], Bayesian approaches [86, 87], etc., can be potentially integrated with the developed anomaly detection framework as well.

3.3 Numerical simulation studies

The objective of the numerical simulation studies is to validate the effectiveness of the proposed spectral feature extraction-based online control charting approach. In comparison, two widely applied statistical control charts, namely, the X-bar chart (with S chart) and EWMA chart are selected as benchmark methods.

Without loss of generality, this simulation study is focused on the univariate data by considering two cases. At first, the phase 1 data (i.e., IC data) that is applied to build baseline and control limits are sequentially generated from a mixture Gaussian distribution with three clusters as described below,

$$x_t \sim 0.3N(3,1) + 0.4N(6,1) + 0.3N(9,1) \tag{3-11}$$

Then the phase 2 data with two different cases are generated subsequently. For case 1 (C1), the data follows a new mixture distribution as Eq. (3-12), which describes the case that three clusters merge to two clusters.

$$x_t \sim 0.5N(3.68,1) + 0.5N(8.32,1) \tag{3-12}$$

On the contrary, the phase 2 distribution in case 2 (C2) is presented in Eq. (3-13), which implies that three clusters split into four clusters.

$$x_t \sim 0.18N(2,0.2) + 0.32N(5,0.2) + 0.32N(7,0.2) + 0.18N(10,0.2) \tag{3-13}$$

Based on the above pre-defined distributions, 6000 signals are generated for both phase 1 and phase 2 data (including C1 and C2), respectively. Since the traditional SPC approaches already have strong capability to detect mean/variance shift effectively, to demonstrate the effectiveness of the proposed method clearly, there is no significant mean/variance shift in both of the two cases based on the simulated distributions (see Table 3-1).

Table 3-1: The mean and variance of the simulation data.

Simulation Data	Numerical Characteristics	
	Mean	Variance
Phase 1	6	6.4
Phase 2 – C1	6	6.38
Phase 2 – C2	6	6.44

Subsequently, to perform the proposed method, the window size n is set as 60 without overlap, and the radial basis function (using Euclidean distance) is applied to quantify the similarity between data points. Afterwards, to determine the edge connection, the mean value of similarity is utilized as threshold. Then λ_3 is selected based on the developed maximum Eigengap criterion. For the design of the control chart, an EWMA chart with $\lambda = 0.25$, which is a common choice in practice, is applied for change detection. The control limits are defined by the traditional three-sigma rule. Then the results are presented in Figure 3-3. For both C1 and C2, the anomaly can be detected immediately when the changes occur, and there is no false alarm in phase 1 status. Therefore, the proposed method is not only sensitive for detecting the changes, but also robust for the IC status (no false alarm).

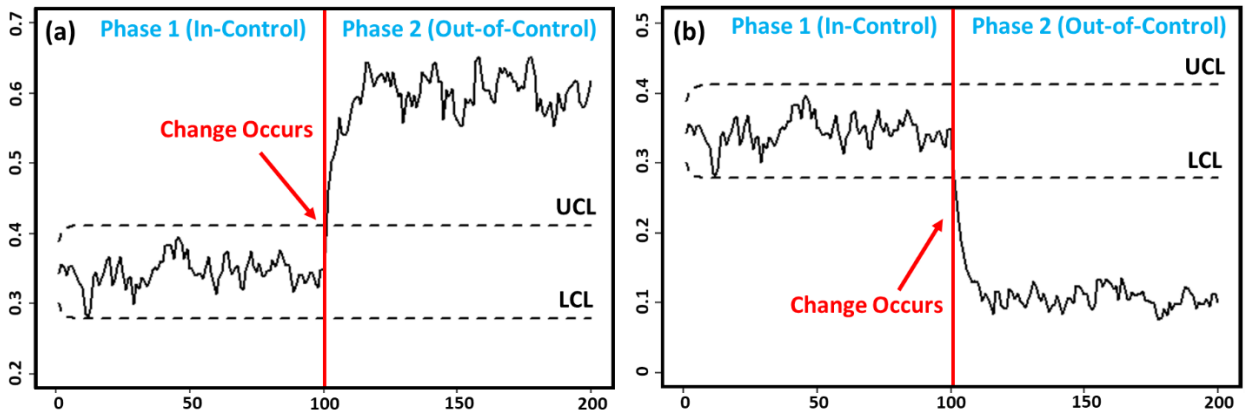

Figure 3-3: The anomaly detection performance of the proposed method. (a) The results of C1; (b) the results of C2.

On the other hand, the results for the benchmark methods are presented in Figure 3-4. By using the same three-sigma control limits, both the X-bar (and S chart) and EWMA chart are not able to detect the anomaly effectively. Consequently, the proposed method significantly outperforms the benchmark methods.

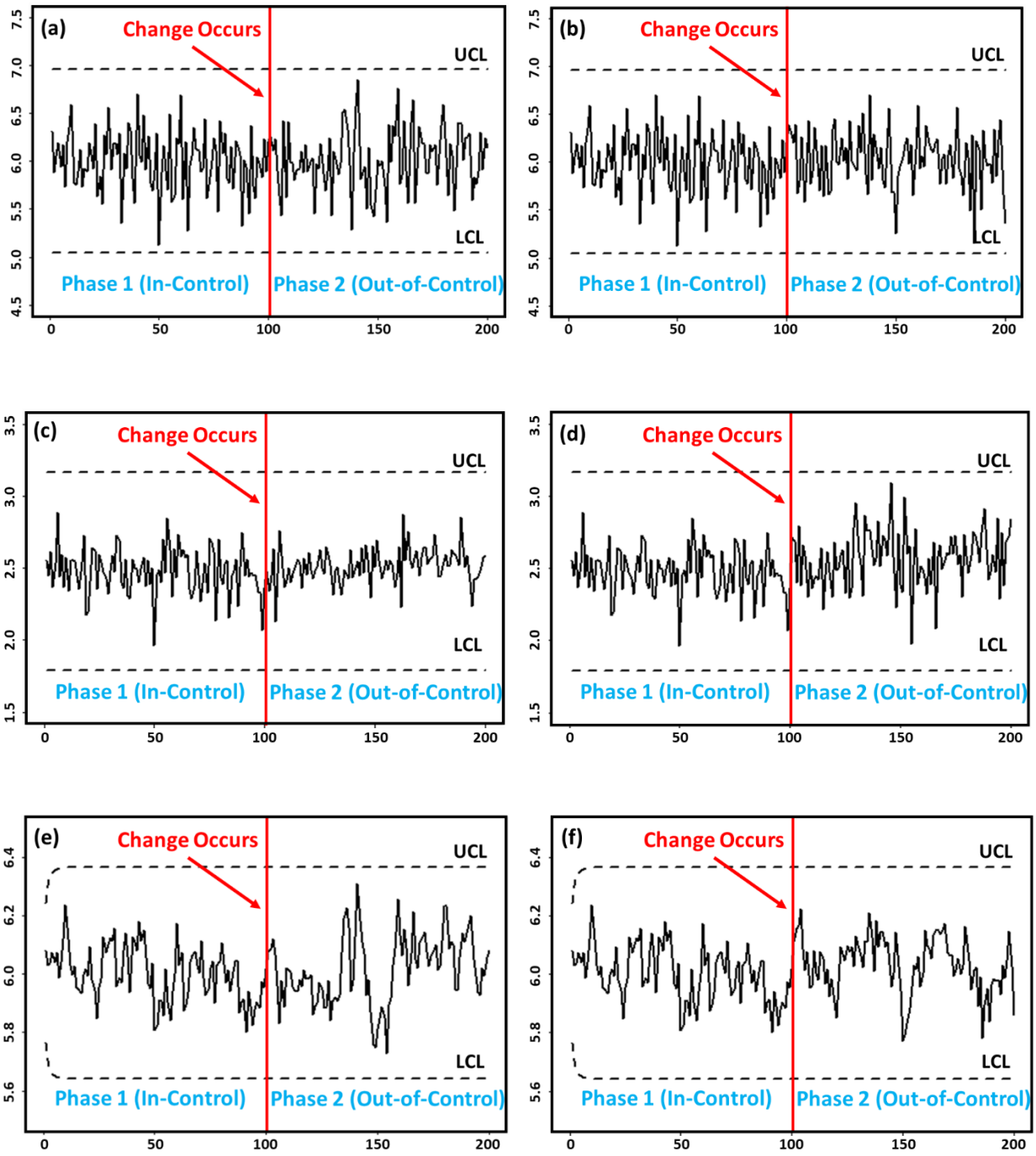

Figure 3-4: The results of the benchmark methods. (a) X-bar chart for C1; (b) X-bar char for C2; (c) S chart for C1; (d) S chart for C2; (e) EWMA chart for C1; (f) EWMA chart for C2.

3.4 Case study

In this section, the proposed data-driven spectral feature extraction approach for process anomaly detection is applied in an actual FFF 3D printing platform, by using the *in situ* vibration sensing signals (side channel). The real-world problem and experimental setup are introduced in Section 3.4.1, followed by the results interpretation and discussion in Section 3.4.2.

3.4.1 Problem introduction and experimental setup

The objective of this case study is to detect the unintended process anomalies in AM caused by cyber-physical attacks based on side channel monitoring. Nowadays, with the rapid development of Internet and smart systems, the cyber-physical security concern has become one potential important risk for manufacturing systems [88-90], including AM systems [91-93]. For instance, a cyber-physical attack may insert a small void in the STL file (i.e., the 3D design) before printing (Figure 3-5). Compared with the case study problems that are investigated in Chapter 4, the major difference is that the process itself is still healthy (i.e., no quality issue from the machine side) in this problem. Therefore, it is impractical to directly apply the existing methods in this case.

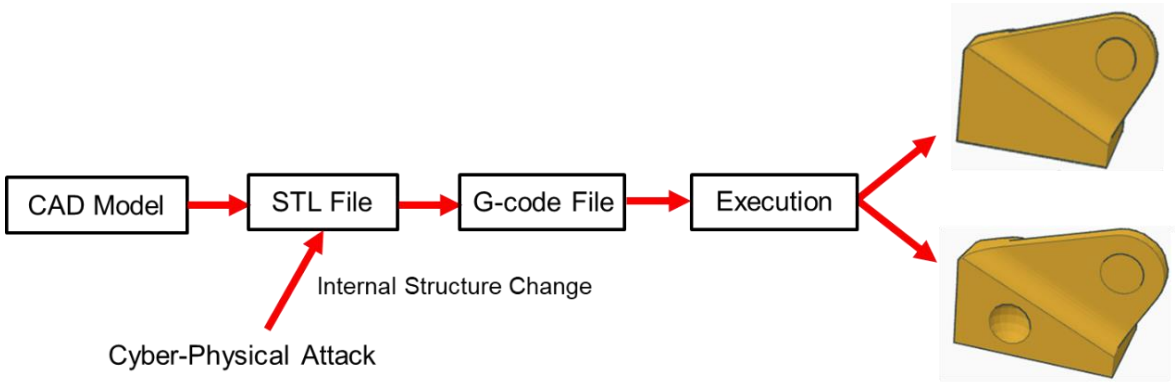

Figure 3-5: Demonstration for an example of cyber-physical attack to the AM process.

On the other hand, due to the high complexity of the AM process, when the design is changed, the variability of inherent patterns in the sensor signals under healthy printing may also exist. Although

the process is still under the same printing condition, the cyber-physical attack may change the patterns due to the significant difference of G-code, which will be apparent in the variation of the underlying distribution for the spectral features. Therefore, the proposed anomaly detection method could be an effective solution for this problem.

In this case study, a desktop FFF-based 3D printer (detailed information for this experimental platform is demonstrated in Chapter 6), namely, Hyrel System 30M, is applied to conduct the experiments. Then to monitor the process, two vibration sensors (i.e., MEMS accelerometers) are mounted to the extruder and printer hot bed (see Figure 3-6) as side channels, respectively, which are capable of tracking the real-time vibrations in terms of x, y, z three axis with 4Hz sampling frequency.

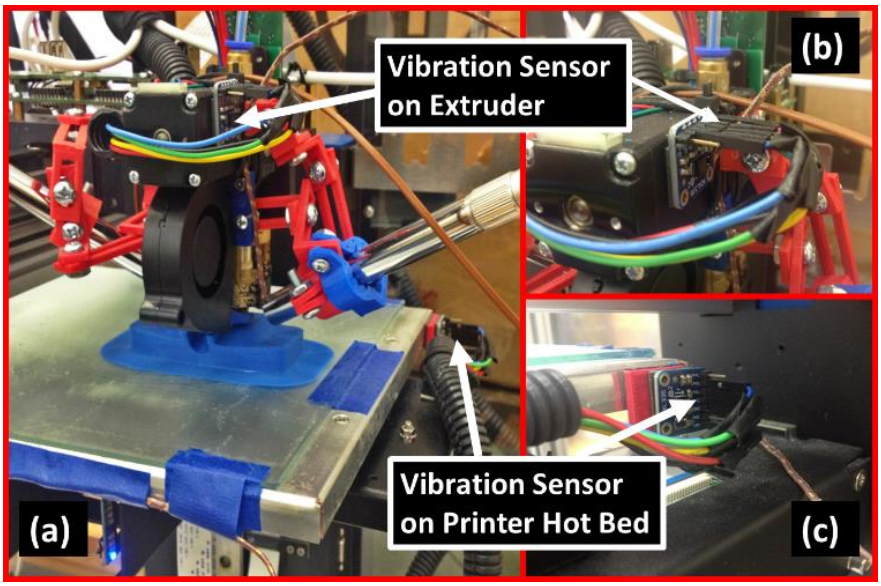

Figure 3-6: The configuration of the FFF printer along with the locations of the accelerometers. Both accelerometers are three-axis Micro-Electro Mechanical System (MEMS) accelerometers.

For the testing part of this case study, a replicate of a General Electric (GE) aviation jet engine bracket is designed. The original design is used to affix jet engines for an airplane, which is from a GE aviation CAD competition [94] and scaled down for the investigation purpose. The reason to use a CAD model based on commercially available parts is to bring attention to the vulnerability

in the current applications. Embedding a void in this bracket may cause significant damages for the real-world applications. Therefore, to simulate a cyber-physical attack for this case, a void (a small hole) that is approximately 5% of the volume of the part is embedded in the center of the part through the change of STL file. Consequently, as demonstrated in Figure 3-7(a), the printing process for this case can be summarized as three stages, where the stage 2 is attacked and stage 3 is also impacted by the attack. This instance may result in debilitating consequences because the difference after attack is hidden from view and it will be susceptible to pass traditional human inspection. As displayed in Figure 3-7(b), it is very difficult to distinguish the printed normal and attacked parts. In addition, since the volume of void is very small, it is also hard to identify the attacked parts by comparing the weight.

To perform the experimental study, six normal parts (i.e., no void) were printed and then three "attacked" parts were printed. Meanwhile, the side channel information, i.e., vibration sensor data, is also collected from the extruder and hot bed. Then based on the real-time sensing signals for both the normal and attacked parts, the analysis and detection performance are presented in Section 3.4.2.

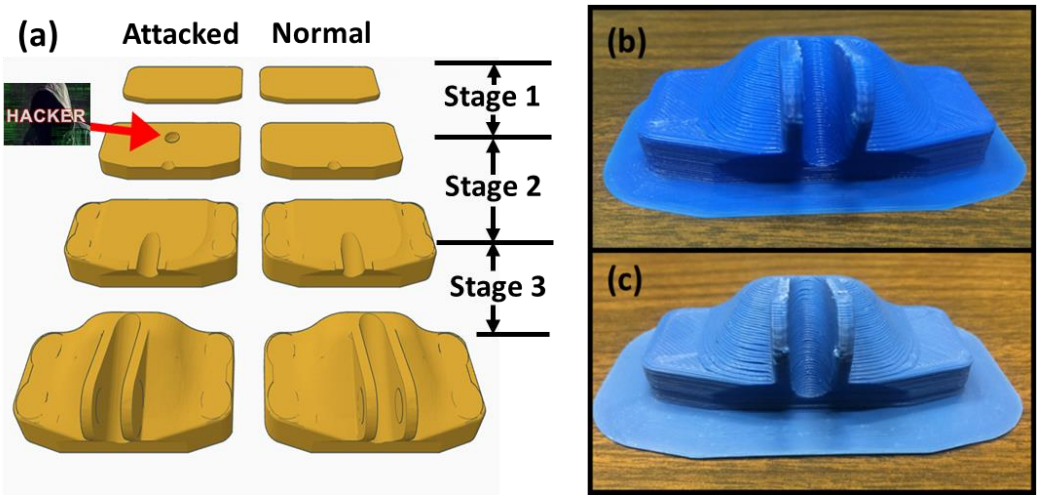

Figure 3-7: (a) The difference between normal and attacked parts; (b) printed sample of the normal part; (c) printed sample of the attacked part.

3.4.2 Sensor signal analysis and detection results

As introduced in Section 3.4.1, sensing signals from two vibration sensors are applied for analysis. The format of sensor output is in the form of "x", "y", and "z" coordinates stored in discrete time increments with a sampling frequency of 4 Hz. Then based on the experimental setup (see Section 3.4.1), six normal parts and three attacked parts are printed for analysis. To validate the performance of the proposed method, four of the normal parts and one of the attacked part are applied to build the control chart (i.e., to determine the input parameters and control limits), and the other parts (i.e., two normal and two attacked parts) are used to test the detection sensitivity and false alarm rate.

To represent the sensor data as a graph, the window size is set as 20 without overlap and the radial basis function-based similarity (using Euclidean distance) with the threshold using the overall median of the similarity matrix is applied. The reason to use median instead of mean in this case is that typically median is a more robust statistic in practice. Then for the feature extraction step, λ_3 is extracted based on the maximum Eigengap-based feature selection rule. Afterwards, as discussed in Section 3.2.4, to investigate the underlying distribution change of λ_3 when attack occurs, the developed quantile-based statistics are utilized to detect the cyber-physical attack. In this case, a 30% lower quantile is selected. Then to calculate the monitoring statistics for control charting, window size 60 with overlap 59 (i.e., to perform consecutive windows) is applied for online application.

Subsequently, for the design of the control chart, due to high complexity dynamics, the baseline and control limits during the process will change dynamically. Since the applied monitoring statistic is essentially a type of attribute, a np chart with dynamic control limits is designed for

process anomaly detection. The detailed procedure for control charting in this case is described below.

- Baseline: for each time instant t, calculate the average of the monitoring statistics among the four training normal parts (i.e., to estimate $\widehat{np(t)}$, where $n = 60$) as the baseline.
- Control limits: estimate the control limits based on np chart (see Eq. (3-14)), where $k = 2.5$ based on the performance evaluated by training data (i.e., the selected four normal and one attacked parts).

$$\begin{aligned} \mathrm{UCL}(t) &= \widehat{np(t)} + k\sqrt{\widehat{np(t)}(1-\widehat{p(t)})} \\ \mathrm{LCL}(t) &= \widehat{np(t)} - k\sqrt{\widehat{np(t)}(1-\widehat{p(t)})} \end{aligned} \tag{3-14}$$

- Control role: for online application, if the monitoring statistic is out of lower or upper control limits, then a cyber-physical attack alarm will be given.

Afterwards, to validate the effectiveness of the proposed method, two aspects are considered: (1) the detection sensitivity for the three attacked parts; and (2) the false alarm rate for the two normal parts. The detection results for these five tests are demonstrated in Figure 3-8. It can be seen that all three attacked parts are detected successfully and there is no false alarm for the two normal parts. Therefore, the analysis and results demonstrate that instances of abnormal behavior can be detected effectively.

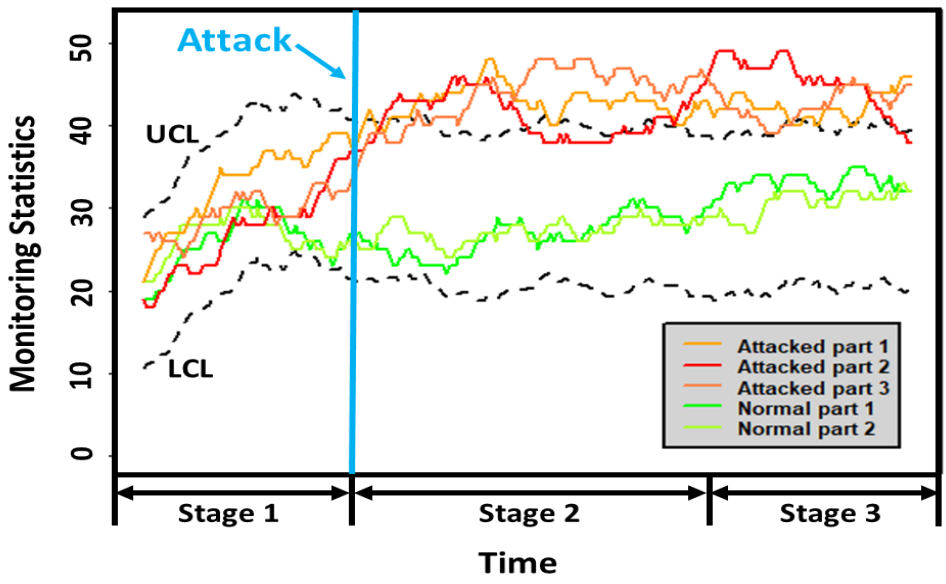

Figure 3-8: The performance of the developed online anomaly detection method for cyber-physical attack detection in AM.

3.5 Conclusions

This chapter develops a data-driven feature extraction-based online process anomaly detection approach using spectral graph theory. Compared with the existing process monitoring and change detection methods, the novelty and contribution of this study is to take consideration of the variation of inherent structure inside the sensing signals based on a graph perspective. Then the change of inherent structure can be effectively tracked by control charts using appropriate feature-based monitoring statistics. The numerical simulation study with different cases demonstrates that the proposed method is capable of effectively detecting the process anomaly with high sensitivity but low false alarm rate, which significantly outperforms the benchmark methods. For the real-world application in AM, the preliminary results show that the proposed method is very promising to implement effective online process anomaly detection in AM, such as the detection of cyber-physical attacks.

For the future work, there are two potential directions. First, it is necessary to find an effective rule to optimize the input parameters such as window size and window overlap. Second, the preliminary studies show that the proposed method is very effective, but the number of experiments is still limited. Therefore, with more experimental studies, more data sets will be collected to further validate this proposed method, which could make the results more convincing.

4 An integrated manifold learning approach for online defect diagnosis

As a powerful dimension reduction technique, manifold learning algorithms have been widely applied to high-dimensional data analytics. With the rapid development of sensor technologies, one of the most critical potential applications for manifold learning is online sensing signal analytics. Consequently, the objective of this chapter is to develop a manifold learning-based online process defect diagnosis method for AM using online sensing data. However, due to the limitation of the existing manifold learning research, how to improve the performance of metric preserving and noise resistance in analytics is still very challenging. To address this issue, this chapter develops a new integrated manifold learning approach termed the multi-kernel metric learning embedded isometric feature mapping (MKML-ISOMAP) method for online real-time dimension reduction. With the application of supervised machine learning algorithms, an online process monitoring framework for AM is enabled to identify the defective printing status. In the numerical simulation and real-world case studies, the proposed method demonstrates excellent performance in data compression and feature extraction. In addition, it is also applicable to extend the current generic integrated learning framework to other real-world dimension reduction problems that involve different types of manifold learning algorithms.

4.1 Introduction

As introduced in Chapter 1, AM technologies have great potentials in a large variety of applications. [2]. However, how to effectively monitor the process and printing status still remains challenging due to the inherent complexities of AM.

To address this challenge, the objective of this chapter is to develop an effective methodology for online process monitoring of AM processes. Based on the AM experimental apparatus with online sensing capabilities [15], massive real-time data with the process quality information are available for analysis. Therefore, it is very promising to identify the quality status through appropriate supervised machine learning algorithms, particularly, the classification algorithm. Nowadays a large variety of research in machine learning has been accomplished in classification, such as support vector machine (SVM), k-nearest neighbors (k-NN), discriminant analysis (e.g., LDA/QDA), neural networks (NN), etc. [95]. However, in real world applications, such as AM and other related advanced manufacturing processes, since the online sensing signals are usually high dimensional and very noisy, the existing classification algorithms may provide inaccurate results, e.g., false alarm or miss detection, which may result in waste of resources and reduce the monitoring effectiveness significantly. The key reason is that the direct application of classification algorithms cannot effectively utilize the most useful information for the noisy high dimensional sensing data, so that the classification performance may be negatively impacted. Therefore, an effective dimension reduction algorithm for feature extraction is needed for this study.

Manifold learning [96-98] is an effective approach to implement non-linear dimensionality reduction, and has been applied in many real-world applications. The main idea of manifold learning is to seek an appropriate embedding of the original observed data from high-dimensional space $\mathcal{X}$ into a lower dimensional space $\mathcal{Y}$, while still preserving the structure of the underlying manifold of the raw data.

$$\mathcal{X} \xrightarrow{mapping} \mathcal{Y} + \epsilon \tag{4-1}$$

In general, the basic assumption is that input data sets lie on a lower dimensional smooth manifold which is embedded in the ambient Euclidean space. The first two manifold learning algorithms were reported in [99, 100], and nowadays a large number of related methods have been proposed based on different types of problems [96]. Compared with the traditional linear approaches, manifold learning has a superior capability in capturing the true data structure of nonlinear data sets (Figure 4-1).

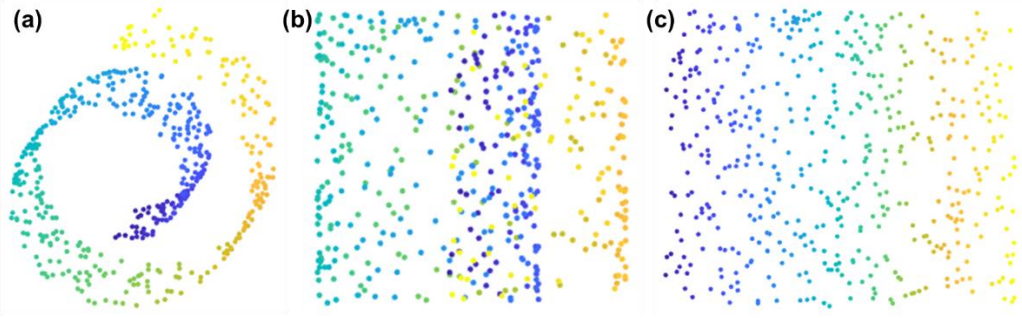

Figure 4-1: A demonstration of effective manifold learning; (a) "Swiss roll" shaped data (2D manifold in a 3D space), (b) PCA results (failed), (c) manifold learning results.

However, most of the existing manifold learning algorithms assume that the data has a very low level of noise and a sufficient number of sample points are available. Unfortunately, in practice, these assumptions are hardly satisfied. Furthermore, due to the requirement of real-time process monitoring, fast computation is also an important aspect of the algorithm, which is another limitation of the current manifold learning work due to intensive computation caused by the non-parametric nature.

Thus, to overcome the above challenges, it is necessary to develop a novel manifold learning methodology, and apply it to AM process monitoring. To achieve this goal, this chapter proposes a new integrated manifold learning approach for dimension reduction, which is realized by a developed multi-kernel metric learning embedded isometric feature mapping (MKML-ISOMAP) algorithm. This proposed MKML-ISOMAP algorithm is to overcome the above shortcomings by

achieving the following three aims: (1) improve the classification accuracy and computational efficiency for real-time applications; (2) provide more timely diagnosis information in the extracted features, e.g., the severity of incurred defects; and (3) identify the invalid input data points (e.g., online sensor signals and real-time images) automatically.

The rest of this chapter is structured as follows: the proposed research methodology is discussed in detail in Section 4.2; Section 4.3 presents the numerical simulation study, followed by the validation of real-world case studies in AM, which is demonstrated in Section 4.4; finally, the conclusions are summarized in Section 4.5.

4.2 Research methodology

The overall research approach of this work is summarized in Figure 4-2. It has two main aspects: (1) a high accuracy dimension reduction method by an integrated manifold learning framework; and (2) online process monitoring implementation based on fast and accurate sample extrapolation with classification algorithms.

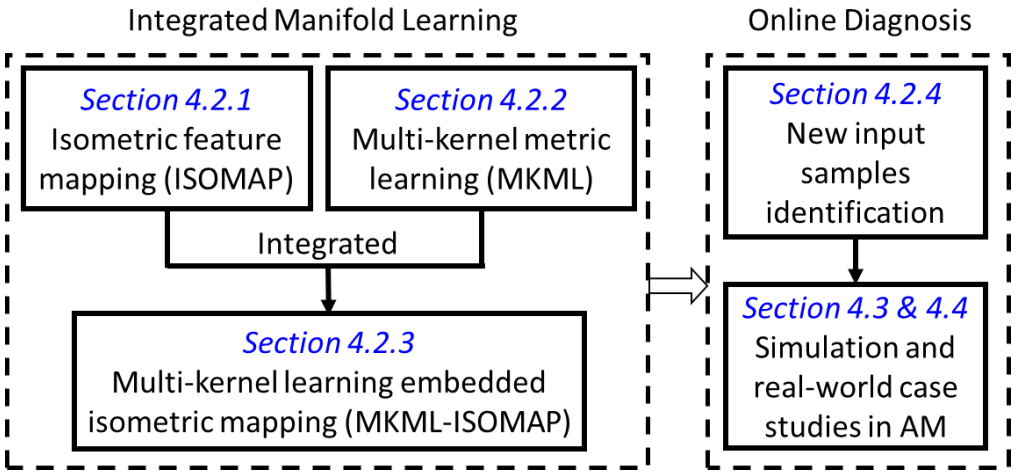

Figure 4-2: The overall research framework for the proposed online process monitoring method.

4.2.1 Isometric feature mapping (ISOMAP)

Isometric feature mapping (ISOMAP) [99] is one of the most popular global approaches in manifold learning that aims to preserve the metrics at all scales, thereby offering an appropriate embedding. The key idea to implement the ISOMAP is to estimate the geodesic distance between faraway points instead of using the Euclidean distance in linear dimension reduction (Figure 4-3(a)). More specifically, from the input data, a distance matrix **D** can be obtained based on a specified distance metric such as the Euclidean distance,

$$\mathbf{D}(i,j) = d_{ij} = ||x_i - x_j|| \tag{4-2}$$

where x_i and x_j are two sample points in the input high-dimensional space. Afterwards, a neighborhood graph can be constructed. The connection relationship between each pair of nodes is summarized by a similarity matrix **S**, as shown in Eq. (4-3),

$$\mathbf{S}(i,j) = s_{ij} = \begin{cases} d_{ij}, & d_{ij} \leq \epsilon \\ \infty, & d_{ij} > \epsilon \end{cases} \tag{4-3}$$

where ϵ is a threshold, termed the neighborhood size, to determine the connection. Then the geodesic distance between two points, i.e., the two nodes in the constructed neighborhood graph, is computed by the shortest path algorithm [101]. Based on this geodesic distance matrix, the low-dimensional embedding can be implemented by using existing linear dimension reduction methods, e.g., classical multidimensional scaling (MDS) [99]. Figure 4-3(b) summarizes the procedure of the ISOMAP method. For the detail of this manifold learning approach, please refer to Ref. [99].

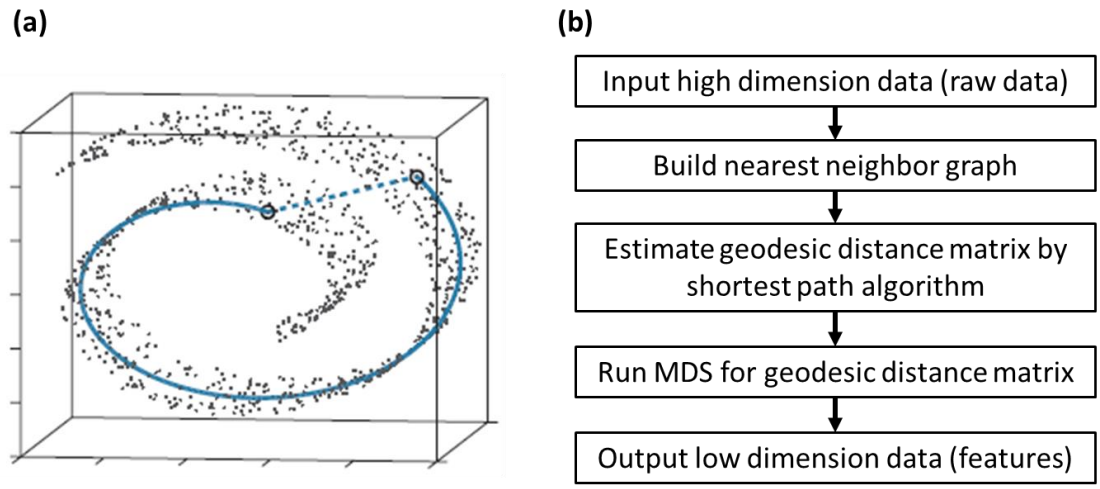

Figure 4-3: (a) The key idea of ISOMAP is to use the estimated geodesic distance instead of Euclidean distance [99]; (b) the procedure of ISOMAP.

Due to the excellent properties and convergence, ISOMAP has been widely applied to a large variety of areas. However, it also requires high sampling rate and low noise level to guarantee its performance [102], which are very difficult to satisfy for the data collected from AM processes. Consequently, a direct application of ISOMAP for AM process monitoring does not work well.

4.2.2 Proposed multi-kernel metric learning (MKML) method

As an important direction of manifold learning, kernel embedding based methods have also been reported in the literature [103, 104] to implement nonlinear mappings. The general idea is to use the kernel trick [105] to reformulate the manifold learning method as a linear projection problem (e.g., PCA, MDS, etc.). More specifically, the original data samples $\{x_i\}$ are mapped into an unknown Hilbert space $\mathcal{H}$ through a nonlinear feature mapping ψ: $\mathbb{R}^n \rightarrow \mathcal{H}$, and then the k-th component of the embedded samples $\{y_i\}$ can be written in term of $\psi(x_i)$ as Eq. (4-4),

$$y_i^k = w_k^T \psi(x_i) \tag{4-4}$$

Although it is usually difficult to provide an explicit mapping, the dimension reduction algorithms just need the distance metric between variables or samples. Fortunately, the inner product, which is one of the most common metric in the feature space $\mathcal{H}$, can be represented via a symmetric function $K: \mathcal{X} \times \mathcal{X} \to \mathbb{R}$ named as kernel function,

$$K_{ij} = K(x_i, x_j) = (\psi(x_i), \psi(x_j))_{\mathcal{H}} \tag{4-5}$$

Based on the general properties of the kernel function, the distance metric in $\mathcal{H}$ also can be formulated as follows,

$$\left|\left|\psi(x_i) - \psi(x_j)\right|\right|_{\mathcal{H}} = (\psi(x_i) - \psi(x_j), \psi(x_i) - \psi(x_j))_{\mathcal{H}} = K(x_i - x_j, x_i - x_j) \tag{4-6}$$

Since the dimension of $\mathcal{H}$ is usually high enough, it can be further considered that the sample distance in $\mathcal{H}$ is equal to the metric in the embedded lower dimension space $\mathcal{Y}$, i.e.,

$$\left|\left|\psi(x_i) - \psi(x_j)\right|\right|_{\mathcal{H}} = ||x_i - x_j||_{\mathcal{Y}} \tag{4-7}$$

Then the embedding problem can be implemented by a linear reduction algorithm if the kernel function is determined. One promising advantage of the kernel embedding based methods is that it can utilize the existing kernel extrapolation (KE) [106] techniques to determine the location of new data samples in the low-dimensional space. However, the challenge is how to obtain the optimal kernel function for a specific data set. Weinberger *et al*. [103] proposed the semidefinite embedding (SDE) algorithm, which learns a kernel matrix for the input samples. However, the output is only a kernel matrix rather than an explicit expression of kernel function.

As discussed in Section 4.2.1, the ISOMAP algorithm may not provide a high learning accuracy for the data with low sampling rate or relative high noise level. One of the reasons is that the shortest path based distance metric cannot filter the noise in the raw data. Also if the data sample is not dense enough, the estimated geodesic distance will not be the best approximation. Therefore,

the key issue is how to improve the accuracy of the estimated distance matrix for the proposed method.

In order to satisfy the above requirement, this proposed method utilizes the geodesic distance learned from ISOMAP as an initial metric, based on which a multi-kernel metric learning (MKML) algorithm is developed. This integration of non-parametric (ISOMAP) and parametric (MKML) aspects will improve the accuracy of distance matrix, and also achieve a fast computation for online application enabled by MKML. In the proposed approach, the multi-kernel function $K(x_i, x_j)$ is created by a linear combination of multiple kernel basis as follows,

$$K(x_i, x_j) = \sum_{n=1}^{p} \beta_n K_n(x_i, x_j, \Theta_n) \tag{4-8}$$

Then the distance metric in $\mathcal{Y}$ can be represented as Eq. (4-9),

$$D_{\mathcal{Y}}(x_i, x_j) = ||x_i - x_j||_{\mathcal{Y}} = K(x_i - x_j, x_i - x_j) = \sum_{n=1}^{p} \beta_n K_n(x_i - x_j, x_i - x_j, \Theta_n) \tag{4-9}$$

Suppose the input data X can obtain a topology-preserving mapping based on ISOMAP, and then by considering the effect of noise ϵ, the geodesic distance metric D_g measured by ISOMAP can be further denoted by $D_g = D_{\mathcal{Y}} + \epsilon$, i.e.,

$$D_g(x_i, x_j) = \sum_{n=1}^{p} \beta_n K_n(x_i - x_j, x_i - x_j, \Theta_n) + \epsilon \tag{4-10}$$

where $\{\beta_n\}$ and $\{\theta_n\}$ are the groups of parameters to be estimated. Based on this relationship between D_g and $D_{\mathcal{Y}}$, the parameters estimation can be solved by the following optimization problem,

$$\arg\min ||D_g(x_i, x_j) - \sum_{n=1}^{p} \beta_n K_n(x_i, x_j, \Theta_n)|| \tag{4-11}$$

$$s.t.\ \beta_n \geq 0$$

Since the objective function is nonlinear, the optimization process may be computationally intensive by using a traditional optimization algorithm. An iterative approach is proposed to solve the above optimization problem, which is based on orthogonal matching pursuit (OMP) [107] and Broyden–Fletcher–Goldfarb–Shanno (BFGS) algorithm [108]. OMP is an effective and fast sparse approximation algorithm [109] which can be applied to estimate the coefficients $\{\beta_n\}$ in the kernel function. BFGS is a popular numerical optimization algorithm for solving unconstrained nonlinear optimization problems [110], i.e., obtain the optimal $\{\theta_n\}$ when the values of $\{\beta_n\}$ are assigned by OMP. The procedures of the proposed MKML is summarized in Figure 4-4.

Algorithm 4-1: MKML algorithm

Input: Initial distance matrix D_g, the basis kernel functions with initial parameters $\{\theta_n\}$

Output: Estimated coefficients $\{\beta_n\}$, parameters $\{\theta_n\}$ and the updated distance matrix D_y

Step 1 Initialize $\{\theta_n: 1,2,\cdots,p\}$

Step 2 Compute the sparse solution for $\{\beta_n: 1,2,\cdots,p\}$ by non-negative OMP

Step 3 Solve the unconstraint optimization for $\{\theta_n: 1,2,\cdots,p\}$ by BFGS algorithm and update θ_k

Step 4 If the residual is lower than the target value or the local minimal is achieved, stop and output D_y. Otherwise go back to step 2

Figure 4-4: MKML algorithm for kernel metric learning.

In the following, a mathematical proof (i.e., Theorem 4-1) is provided to delineate the correctness of MKML method.

- **Theorem 4-1.** The fitting residual $r = ||\widehat{D}_y - D_g||$ can be continuously reduced and finally converges with the increase of iterations.
- **Proof:** Denote the residual as $r(\tilde{\beta}^i, \tilde{\theta}^i)$, where i is the number of iteration. The theorem is equivalent to

$$r(\tilde{\beta}^i, \tilde{\theta}^i) \geq r(\tilde{\beta}^{i+1}, \tilde{\theta}^{i+1}) \tag{4-12}$$

First, considering the updated residual $r(\tilde{\beta}^{i+1}, \tilde{\theta}^{i})$ after step 2 in i-th iteration, since $\{\beta_n\}$ is improved under same $\{\theta_n\}$, $(\tilde{\beta}^{i+1}, \tilde{\theta}^{i})$ should be a better solution compared with $(\tilde{\beta}^{i}, \tilde{\theta}^{i})$, i.e., $r(\tilde{\beta}^{i}, \tilde{\theta}^{i}) \geq r(\tilde{\beta}^{i+1}, \tilde{\theta}^{i})$. Similarly, under identical $\{\beta_n\}$, since $\{\theta_n\}$ is optimized, then $r(\tilde{\beta}^{i+1}, \tilde{\theta}^{i+1}) \leq r(\tilde{\beta}^{i+1}, \tilde{\theta}^{i})$. Therefore, the following inequality can be achieved,

$$r(\tilde{\beta}^{i}, \tilde{\theta}^{i}) \geq r(\tilde{\beta}^{i+1}, \tilde{\theta}^{i}) \geq r(\tilde{\beta}^{i+1}, \tilde{\theta}^{i+1}) \tag{4-13}$$

Also since the fitting residual has lower bound, $r(\tilde{\beta}^{i}, \tilde{\theta}^{i})$ is a convergent series. Q.E.D.

4.2.3 Integrated manifold learning framework: MKML-ISOMAP

Based on the developed MKML method, the proposed integrated manifold learning framework MKML-ISOMAP consists of two phases. Phase 1 provides a global data structure estimation based on geodesic distance measurement using the classical ISOMAP algorithm. In this phase, the input high dimensional data will be converted to a weighted nearest neighbor graph based on an appropriate neighborhood size, and then an estimated distance matrix D_g will be calculated by the shortest path algorithm. Phase 2 applies the proposed MKML approach to refine the estimated distance metric in phase 1. More specifically, D_g will be utilized as a reference to learn the optimal kernel distance metric and a refined distance matrix D_y by Algorithm 4-1 (see Figure 4-4). The final embedding Y can be effectively achieved by classical MDS. The procedure of MKML-ISOMAP is described in Figure 4-5.

Algorithm 4-2: MKML-ISOMAP algorithm
Input: Input data matrix X, the basis kernel functions with initial parameters θ_k
Output: Low dimensional data Y, learned kernel functions
Assumption: There exists a mapping between high and low dimensional representations
Step 1 Compute D_g by ISOMAP with neighborhood size optimization
Step 2 Learn the optimal kernel metrics by MKML and obtain D_y (i.e. Algorithm 1)
Step 3 Implement low dimensional embedding by classical MDS (i.e., get Y)

Figure 4-5: The proposed integrated manifold learning approach MKML-ISOMAP algorithm.

4.2.4 The implementation of online process monitoring

In order to achieve online process monitoring, one of the most important aspects is to identify the location of the online input data samples in the learned manifold, i.e., out of sample extrapolation [111]. For the proposed algorithm, a natural idea is to embed the online collected sample into the low dimensional manifold by learned kernel function. Since the explicit expression of the learned kernel function has been obtained via the MKML algorithm (see Figure 4-5), it can effectively measure the similarity between the new input and original samples in an efficient manner.

In real world applications such as AM process monitoring using a machine vision system, a challenging problem is that sometimes the observation may be invalid or useless. For example, some data observations are collected from an unrelated object, or the sensing environment has changed (the process itself is still healthy) if a machine vision system is being used. Therefore, it is necessary to identify the homogeneity of the new data point before embedding it into the low dimensional space. To achieve that, an identification procedure is implemented as below:

- Nearest distance vector v: $v_i = ||x_i - x_{nn}||$, where x_{nn} is the nearest neighbor of x_i

- Hypothesis: X are uniformly sampled from $\mathcal{X}$, if the new sample x_{new} is significantly far away from X, then it should be invalid.
- Evaluation index: The distance d_e between x_{new} and its nearest neighbor in X.
- Decision rule: If d_e is high than 95% quantile of v, then reject x_{new}, otherwise accept.

After the sample identification, the accepted sensor observations can be embedded into the lower dimensional space by the learned kernel metric, and then be used to determine the quality status of the manufacturing processes, or products based on some simple classification methods.

4.3 Numerical simulation studies

In the numerical simulation study, the classical nonlinear data set "Swiss roll" [99] is generated with different levels of noise and sample size. One sample set of the simulation data is shown in Figure 4-6. To demonstrate the effectiveness of the proposed method, the classical ISOMAP is selected as the benchmark method. Then the performance between ISOMAP and the proposed MKML-ISOMAP is compared using RMSE based on different level of Gaussian noise (i.e., σ^2) and sample size.

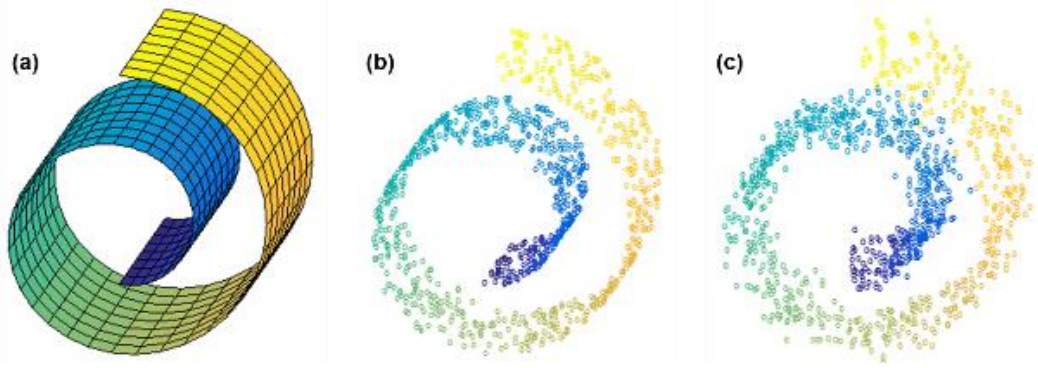

Figure 4-6: The demonstration of "Swiss roll" data, (a) true underlying manifold, (b) sample data without noise, (c) sample data with Gaussian noise.

From the comparison results shown in Figure 4-7(a), it can be seen that under the same noise level, the proposed MKML-ISOMAP can significantly improve the learning performance when the

sample size decreases. In addition, Figure 4-7(b) demonstrates that under the same sample size, the proposed method also outperforms the ISOMAP in terms of RMSE at different noise levels.

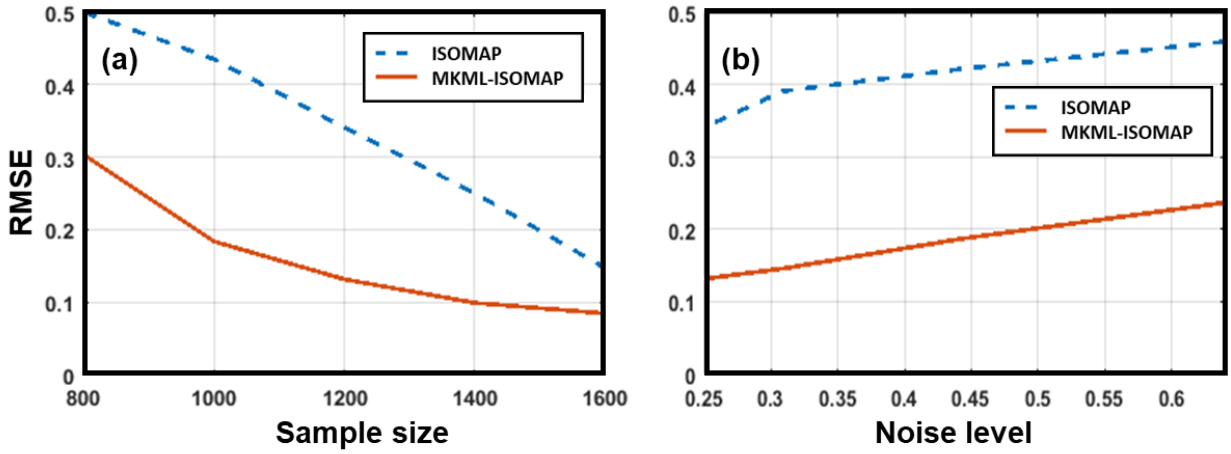

Figure 4-7: (a) RMSE under different sample size, (b) RMSE under different noise level.

4.4 Case studies

In this section, two real-world case studies regarding online defect diagnosis of the AM process are performed to validate the effectiveness of the proposed integrated manifold learning approach. A process state diagnosis study using heterogeneous real-time sensor data is demonstrated in Section 4.4.1, followed by an image-based surface defect diagnosis investigation in Section 4.4.2.

4.4.1 Process states classification based on heterogeneous sensors

In this case study, multiple temperature (thermocouples) and vibration (accelerometers) sensors are mounted at several different locations including extruder and hotbed on a MakerBot Replicator 2X experimental 3D printer (see Figure 4-8). The objective is to implement real-time process state diagnosis by analyzing the online sensing data, where the process states are labeled as three categories: normal state (stable extrusion with smooth surface), abnormal state (inconsistent or stringy extrusion), and failure state (nozzle clogged with scraped surface) [15].

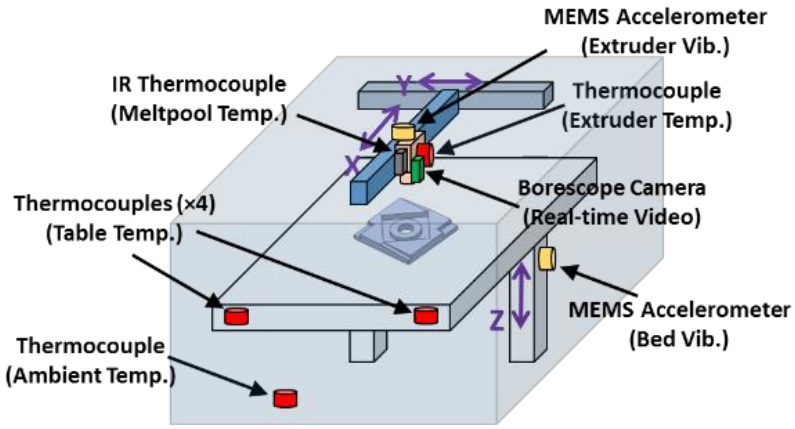

Figure 4-8: The schematic of the applied online sensing system for FFF machine [15].

To achieve this objective, the proposed MKML-ISOMAP method is applied to perform online feature extraction (i.e., dimension reduction). Subsequently, a commonly applied classification method, namely, k-nearest neighbor (k-NN) [112], is selected to identify the printing process states of the FFF machine. To demonstrate the performance of the proposed approach, the following two groups of methods are selected as benchmarks for comparison: (1) several popular classification algorithms in the literature including linear/quadratic discriminant analysis (LDA/QDA), k-NN, naïve Bayes (NB), and support vector machine (SVM) [112]; and (2) traditional nonlinear dimension reduction including NL-PCA [113] and ISOMAP with the proposed online process monitoring framework.

Based on the sensor data, the extracted quality evaluation index (i.e., the 1st dimension in $\mathcal{Y}$) obtained by the proposed approach illustrates that the process quality has a significant continuous decreasing trend (see Figure 4-9). For the performance of diagnosis, the classification algorithms are trained and then applied to predict the three labeled printing states. The prediction performance is evaluated by a commonly applied statistic, namely, F-score (the higher F-score indicates the more correct classification result) [114]. The results are shown in Table 4-1, from which we can

conclude that the proposed MKML-ISOMAP has the superior performance over the benchmark methods.

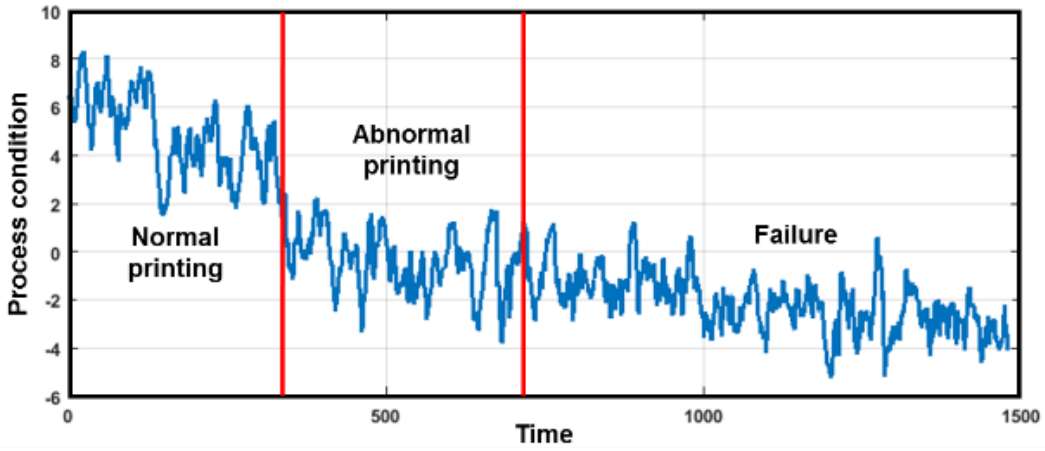

Figure 4-9: Process state identification using the feature extracted by MKML-ISOMAP.

Table 4-1: The comparison of classification performance between the proposed method and benchmark methods.

Groups	Algorithms	Average F-score	Computation time (ms)
1	QDA	0.774	0.72
1	k-NN	0.799	0.15
1	NBC	0.809	0.18
1	SVM	0.752	0.91
2	NL-PCA	0.842	2.2
2	ISOMAP	0.952	>1000
Proposed	**MKML-ISOMAP**	**0.984**	1.7

4.4.2 Surface defect diagnosis based on real-time image data

The objective of this case study is to implement online surface defect diagnosis for the printing parts in the FFF process using a developed machine vision system. The experimental platform for online image acquisition, as shown in Figure 4-10(a), consists of a Hyrel System 30M 3D printer and two digital microscopes with illumination, which are fixed on two sides of the extruder with an approximate 45^{o} inclination. The collected images have 640×480 resolution with about 15

times magnification. A detailed introduction for this image acquisition system is presented in Chapter 6.

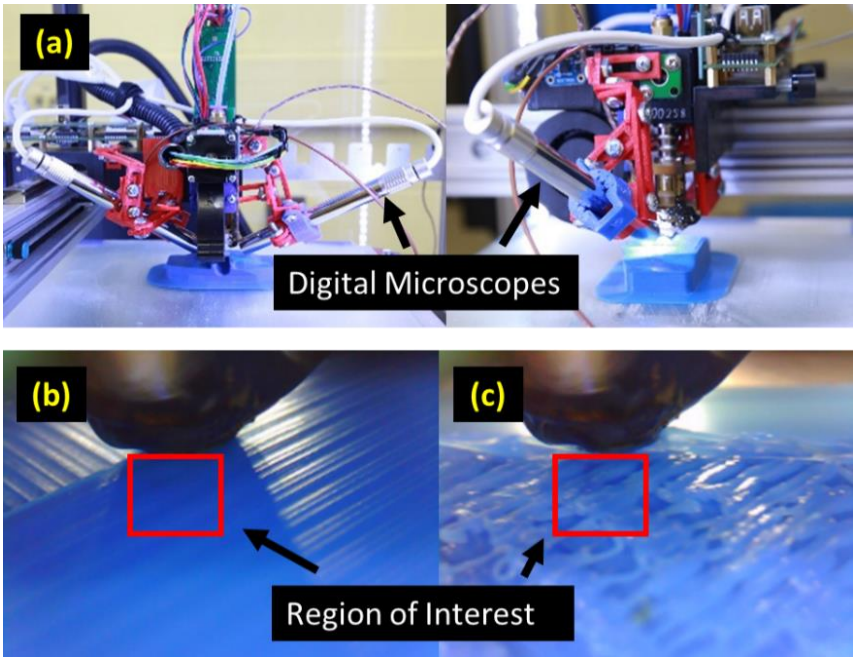

Figure 4-10: (a) Image acquisition system, (b) surface showing normal condition, (c) surface showing defect.

In this study, one frequently occurring defect caused by insufficient material feed, namely, under-fill, with multiple severity levels, is considered for diagnosis. The image data sets are collected using different material feed rates. For the collected images, in order to evaluate the real time quality status, only the region of interest (ROI) is used, which is cropped from the small region (80 by 80 pixels) below the nozzle (see Figure 4-10). Then the images can be represented by the input samples in a $d = 6{,}400$ dimensional vector space. Since the raw input data is very high dimensional, the proposed MKML-ISOMAP is applied to implement dimension reduction, i.e., feature extraction, with the application of k-NN classification for defect diagnosis. In addition, to illustrate the online diagnosis performance of MKML-ISOMAP, the same groups of methods introduced in Section 4.4.1 are used as benchmarks.

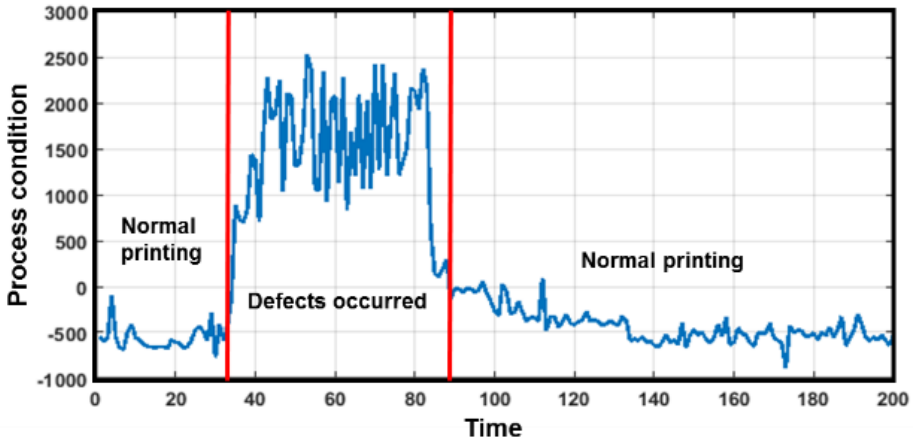

Figure 4-11: The defective printing status can be effectively detected by MKML-ISOMAP.

From a preliminary demonstration result in Figure 4-11, it can be seen that only the 1st dimension in $\mathcal{Y}$ extracted by the proposed approach is able to provide an excellent discrimination between the images from normal and defective printing (50% under-fill) with good interpretability. Furthermore, to diagnose the under-fill defects with different severity levels, after k-NN classification using the extracted features, the proposed method achieves the highest F-score compared with the benchmark methods, which implies this method provides the most effective surface defect diagnosis. Although ISOMAP-based diagnosis can also provide relatively good performance in terms of classification accuracy, the computational efficiency is not good enough for online applications (see Table 4-2).

Table 4-2: The comparison of surface defects diagnosis between the proposed method and benchmark methods.

Algorithms	Average F-score	Computation time (s)
LDA	0.914	0.0035
k-NN	0.936	0.0025
NBC	0.881	0.0038
SVM	0.948	0.0061
NL-PCA	0.947	0.0190
ISOMAP	0.967	>40
MKML-ISOMAP	**0.986**	0.0110

4.5 Conclusions

In this work, a novel manifold learning framework MKML-ISOMAP is proposed by integrating the strength of the non-parametric and parametric oriented data structure learning approaches. The proposed MKML-ISOMAP can successfully improve the learning accuracy for the noisy and low sampling rate data. At the same time, it also provides an efficient out of sample extrapolation framework due to the explicit distance metric expression. The case studies show that the proposed method is very promising in online process monitoring of AM processes.

The future work and investigation along these lines are mainly in two directions. First, the performance of the proposed MKML-ISOMAP still can be further improved. For example, how to further optimize the neighborhood size in graph construction. Second, since this method has excellent properties in noise resistance and feature extraction, it is also very promising to apply it to other advanced manufacturing processes.

5 A bilateral time series modeling approach for online quality/defect forecasting

The objective of this chapter is to investigate the layer-wise quality correlation in additive manufacturing (AM) processes, which can online forecast the AM quality more accurately. This objective is achieved by developing a data-driven modeling approach incorporated with a unique physical thermal phenomenon in AM termed reheating. The layer-by-layer manner of material deposition in AM results in unique thermal phenomena. For instance, in fused filament fabrication (FFF), layers of hot thermoplastic material are melted and deposited by a nozzle. The material of already deposited layers is subjected to repeated heating from the subsequent layers. This continual reheating of the layers has a consequential effect on the part quality. It is therefore important to model and forecast the quality characteristics of layers due to reheating, so that part defects can be forecasted accurately. Existing forecasting methods, such as autoregressive (AR) time series models, consider the effect of past evolutions of the process on the current states, i.e., forecast the outcome at the current time, given information from the past. These models, however, cannot incorporate the effect of forthcoming evolutions in the future on the current time step, in the context of the reheating phenomena in AM. To overcome this limitation, in this chapter a bilateral time series modeling approach is proposed, termed the extended autoregressive (EAR) model, to incorporate the thermal effects of both preceding and forthcoming layers in AM processes. The effectiveness of the approach is demonstrated in the context of a FFF-based 3D printing platform.

5.1 Introduction

The root cause of the poor quality in AM processes, where heat is used to join the layers, stems from the complex thermal interactions ranging across the microstructure-level to the part-level. One such thermal phenomenon is the repeated heating of a layer, as hot material is continually deposited on top. Thus, one layer of material will be reheated multiple times when new layers are deposited, which is termed as reheating effect in this dissertation (Figure 5-1(a)). The reheating effect slows down the material solidification process, or even re-melts the materials in the deposited layers, which may result in several defects, such as large geometric deviation (Figure 5-1(b)) or even significant porosity, etc. These defects will deteriorate mechanical properties of the printed parts [55]. Consequently, forecasting the reheating phenomena is a critical first step towards quality assurance in AM parts. The need for such a forecasting model in AM is further compelled due to the experimental difficulties in obtaining the quality measurement of the printed layers.

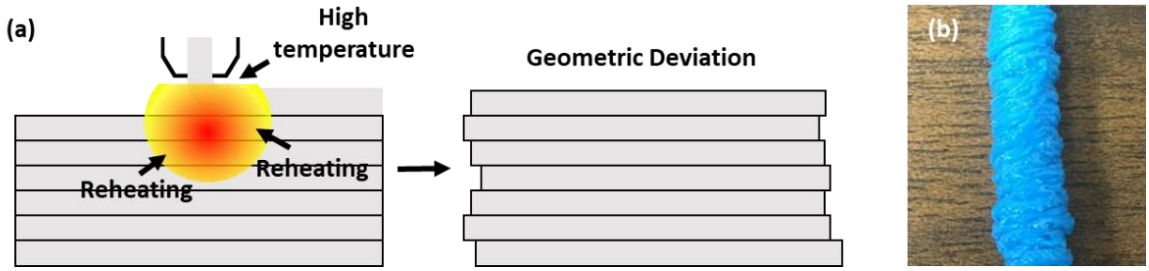

Figure 5-1: (a) The schematic of reheating effects in the layer-by-layer fabrication process; (b) the geometric deviation in an AM part impacted by reheating effects.

Accordingly, this chapter develops a new time series method for forecasting the reheating effect, so that the impact of reheating can be thoroughly understood and possibly controlled. Therefore, the objective of this chapter is to implement the reheating effect modeling and quality characteristics forecast based on an effective time series modeling approach.

The key challenge in modeling the reheating effect stems from the fact that the instantaneous heat in the current layer comes not only from past but also future layers. A large body of research work has been accomplished in time series modeling, such as autoregressive integrated moving average (ARIMA) model [115], generalized autoregressive conditional heteroscedasticity (GARCH) model, etc. [116]. However, these existing time series modeling approaches only take into consideration the impact of the past states on the current one, but do not include the future states, which cause reheating in the AM context. The proposed EAR model presented in this chapter is a substantial improvement over the existing techniques, because it provides a comprehensive framework for modeling the reheating phenomena.

The rest of this chapter is organized as follows. The proposed research methodology is presented in detail in Section 5.2; Section 5.3 and 5.4 provided numerical examples and actual case studies of AM, respectively, to demonstrate the effectiveness of the proposed method. Finally, the conclusion is discussed in Section 5.5.

5.2 Research methodology

This chapter proposes a bilateral time series model for online quality forecasting in AM processes. This model takes into consideration the impact of both past and future states on the current state. As shown in Figure 5-2, the overall framework of the proposed methodology consists of four parts: (1) the reheating phenomenon in AM in terms of the aspect of statistical modeling is discussed in Section 5.2.1; (2) a new bilateral time series-based forecasting model termed the extended autoregressive (EAR) model, to capture the reheating effects in AM, is proposed in Section 5.2.2; (3) an approach to estimate the parameters of the proposed model is developed in Section 5.2.3; and finally (4) the strategy and technical details for online layer-wise quality forecasting for AM parts, based on the proposed bilateral time series model, are discussed in Section 5.2.4.

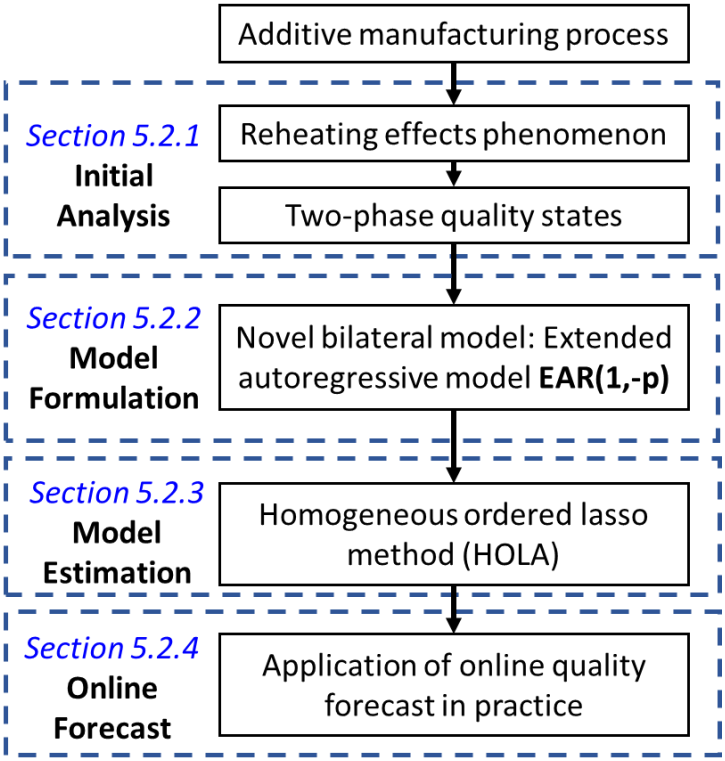

Figure 5-2: Overall methodology of the proposed bilateral time series modeling approach for online quality forecasting in AM processes.

5.2.1 Bilateral time series model for reheating phenomenon in AM

As introduced in Section 5.1, reheating effect is a unique thermal phenomenon in AM processes. For example, in FFF, the layer thickness is usually less than one millimeter (e.g., 0.3 mm in our case studies). Therefore, the deposition of one layer may significantly influence the quality of the previous layers. Since reheating may re-melt or partially re-melt the deposited materials, it will bring extra variation to the part being printed, so that defects such as larger geometric deviation may occur.

Due to the layer-to-layer interaction in AM processes, the dependence of the quality characteristics of a given layer t comes from two directions, namely, (1) past layers, and (2) future layers (i.e., reheating effects). Since all the impacts from previous layers will accumulate to the immediate

past layer t-1 when layer t is being printed, only layer t-1 needs to be considered. In the other direction, the reheating effects from the future layers will influence the layer t sequentially (see Figure 5-3). Although theoretically all the future layers will reheat the current layer t, the effect will be diminished gradually when future layers are eventually moved away from the current, due to the reduction of heat transfer [117]. Therefore, only the nearest p future layers have actual significant reheating effect to the current layer. The value of p needs to be determined in the model estimation stage (Section 5.2.3).

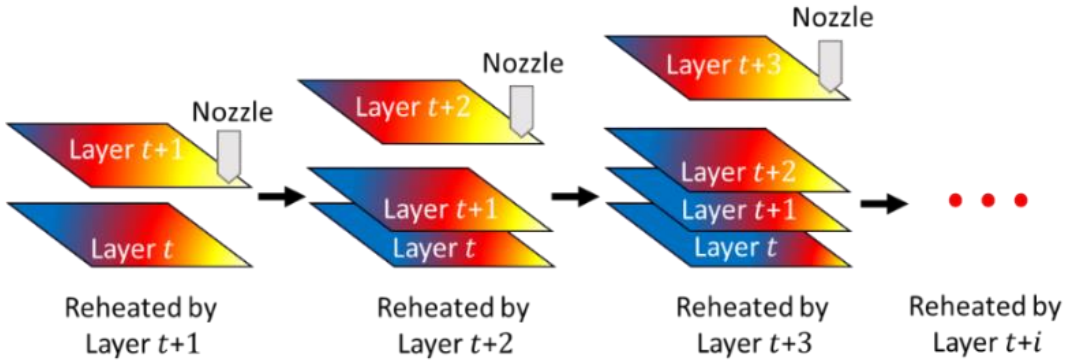

Figure 5-3: A demonstration of the reheating phenomenon in AM process.

In order to model this reheating phenomenon, let x_t be the layer-wise quality characteristic of layer t. Based on the above qualitative analysis, x_t actually depends on not only the past layer state x_{t-1} but also the future layer states $\{x_{t+i}\}$ $(i = 1,2, \dots, p)$. For a simple autoregressive model AR(1), the autocorrelation is at only one direction to the past, i.e., the current state of the random variable depends on its previous state x_{t-1}. If the impact from the future layer state x_{t+1} is also considered, then a corresponding bilateral autoregressive model can be formulated as follows [118],

$$x_t = \mu + ax_{t-1} + bx_{t+1} + \epsilon_t \tag{5-1}$$

where a and b are the coefficients for the past and future layer states, respectively, and ϵ_t is the noise term with constant variance σ^2. Based on the reheating effect (see Figure 5-3), it is also necessary to extend the Eq. (5-1) to a higher order model, which is formulated as follows,

$$x_t = \mu + ax_{t-1} + \sum_{i=1}^{p} b_i x_{t+i} + \epsilon_t \tag{5-2}$$

where p is the order of the extended model. The value of p indicates that layer t will be reheated p times by the future p layers. Although the bilateral time series model in Eqs. (5-1) and (5-2) has been proposed by Ref. [118], unfortunately, it does not fully capture the mechanism of reheating phenomenon in AM, which is justified as follows.

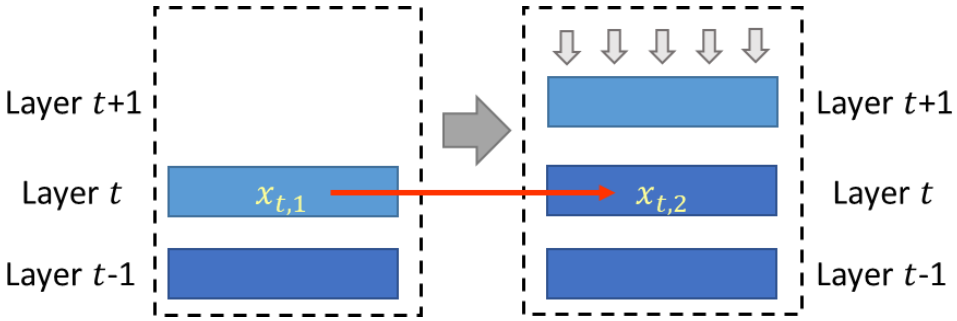

Figure 5-4: Illustration of reheating process in AM.

Based on the physical process of the reheating effect, it can be seen that x_t essentially consists of two phases: (1) phase 1 state $x_{t,1}$, which is the initial quality characteristics of layer t right after it is deposited, and (2) phase 2 state $x_{t,2}$, which is the characteristics of layer t after layer t+1 has been deposited (Figure 5-4). Transition from $x_{t,1}$ to $x_{t,2}$ is actually caused by the reheating effect (deposition of layer t+1). Clearly, the existing bilateral time series model in Eq. (5-2) proposed by Ref. [118] cannot capture the reheating effect in AM processes. Consequently, to address this limitation, a new two-phase bilateral time series model for reheating effect modeling is proposed in Section 5.2.2. The term of two-phase is named based on the aforementioned phases 1 and 2 sub-states.

5.2.2 Proposed extended autoregressive model EAR$(1, -p)$

Based on the definition of the two-phase sub-states introduced in Section 5.2.1, x_t is represented

as follows,

$$\mathbf{x_t} \stackrel{\text{def}}{=} (x_{t,1}, x_{t,2})^T \tag{5-3}$$

Using this definition, the new EAR model is proposed and illustrated in Figure 5-5. Since $x_{t,1}$ corresponds to the state of layer t without any effects from future layers, it is only impacted by the immediate past state, i.e., $x_{t-1,1}$, termed *historical impact* (Figure 5-5). Then for $x_{t,2}$, since it describes the state of layer t after the future layers (namely, layer $t+i, i = 1, \ldots, p$) deposition, it is influenced by the future layer states, i.e., $\{x_{t+i,1}\}$, termed *future impact* (Figure 5-5). Therefore, based on these relationships, two connected statistical models for $x_{t,1}$ and $x_{t,2}$, namely, phase 1 and phase 2 models, can be developed, respectively, as depicted in Figure 5-5.

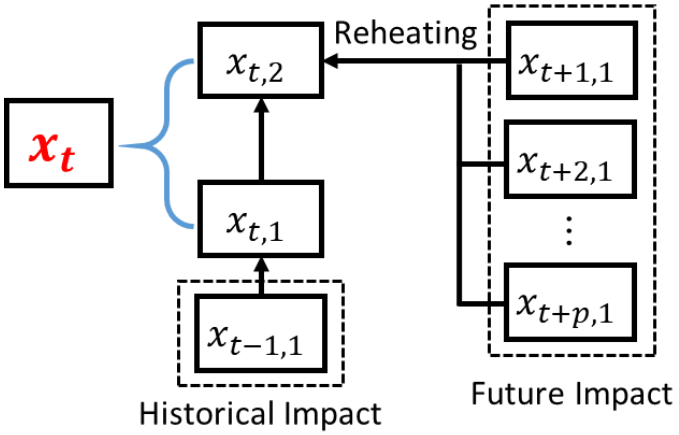

Figure 5-5: The basic framework of the proposed bilateral $EAR(1,-p)$ model

Phase 1 model is proposed to quantify phase 1 sub-state $x_{t,1}$, assuming the effect derived from the previous state is based on linear correlation, and then the historical phase can be described by an autoregressive model AR(1) with coefficient a, as shown in Eq. (5-4),

$$x_{t,1} = \mu + a x_{t-1,1} + \epsilon_{t,1} \tag{5-4}$$

where μ is a constant and $\epsilon_{t,1}$ is the noise term with zero mean and variance σ_1^2; the condition of $|a| \leq 1$ is required to guarantee model stationarity. Many methods can be applied to fit Eq. (5-4),

such as Yule-Walker, OLS, and MLE [119].

Phase 2 model is developed to capture the transition from $x_{t,1}$ to $x_{t,2}$. Assume the future p layers will significantly impact $x_{t,2}$ through reheating; then $x_{t,2}$ can be quantified by a constrained p-order linear regression as shown in Eq. (5-5),

$$\begin{gathered} x_{t,2} = b_0 x_{t,1} + \sum_{i=1}^{p} b_i x_{t+i,1} + \epsilon_{t,2} \\ |b_i| \geq |b_{i+1}| \\ b_i b_{i+1} \geq 0 \end{gathered} \tag{5-5}$$

where b_0, b_i $(i = 1, \dots, p)$ are the coefficients to be estimated, and $\epsilon_{t,2}$ is the noise term with zero mean and variance of σ_2^2. In general, parameter estimation and order determination for this model can be conducted using existing regression analysis methods, e.g., stepwise regression with statistical criterion, ridge regression and Lasso algorithm, etc. [120]. However, for the coefficients b_i in the model, two constraints, namely, $|b_i| \geq |b_{i+1}|$ and $b_i b_{i+1} \geq 0$ for $i = 1,2,\cdots,p-1$ should be added, which can be justified by the fact that closer layers will have higher impact on current layers and the impact should be homogeneous (either all positive or negative).

To address the difficulties of model fitting caused by the above constraints, this study proposes a Lasso-based method, which is discussed in detail in Section 5.2.3. Compared with the traditional time-lagged regression, the explanatory variables include not only past but also future states in this model. Thus, this model is termed *time raised regression* in this chapter. Combining Eqs. (5-4) and (5-5) together based on Eq. (5-3), the proposed two-phase bilateral model can be formulated as follows,

$$\mathbf{C}\mathbf{x}_t = \boldsymbol{\mu} + \mathbf{A}\mathbf{x}_{t-1} + \sum_{i=1}^{p} \mathbf{B}_{\boldsymbol{i}}\mathbf{x}_{t+i} + \boldsymbol{\epsilon}_{\boldsymbol{t}} \tag{5-6}$$

where $\boldsymbol{\epsilon}_{\boldsymbol{t}} = (\epsilon_{t,1},\ \epsilon_{t,2})^T$, and $\boldsymbol{\mu} = (\mu,\ 0)^T$. $\mathbf{A}$, $\mathbf{B}_{\boldsymbol{i}}$ and $\mathbf{C}$ are the coefficients matrix of states $\mathbf{x}_{t-1}$, $\mathbf{x}_{t+i}$ and $\mathbf{x}_t$, respectively, which are represented by,

$$\mathbf{A} = \begin{pmatrix} a & 0 \\ 0 & 0 \end{pmatrix}, \mathbf{B}_{\boldsymbol{i}} = \begin{pmatrix} 0 & 0 \\ 0 & b_i \end{pmatrix}, \mathbf{C} = \begin{pmatrix} 1 & 0 \\ -b_0 & 1 \end{pmatrix} \tag{5-7}$$

It also can be seen that Eq. (5-6) will be reduced as an AR(1) model for $x_{t,2}$ if $p = 0$,

$$x_{t,2} = ax_{t-1,2} + \epsilon_t \tag{5-8}$$

which is based on the same historical dependence of Eq. (5-4). Therefore, this proposed model is termed the extended autoregressive (EAR) model since it is essentially a bilateral extension of the AR model. In addition, the order of the EAR model is $(1, -p)$ since the dependence of the phase 2 model is from the future. To achieve online forecasting, the next step is to provide an effective model-fitting algorithm, which is presented in Section 5.2.3.

5.2.3 Homogeneous ordered lasso method (HOLA)

A novel bilateral time series model EAR$(1, -\mathrm{p})$ for online quality forecasting of AM processes is proposed in Section 5.2.2. This section develops an effective new method named homogeneous ordered lasso (HOLA), which can fit the EAR model accurately and efficiently.

For the phase 1 model (Eq. (5-4)), its model parameter estimation can be accomplished using the existing methods such as Yule-Walker, OLS and MLE [119]. Therefore, the major challenge is to fit the phase 2 model (Eq. (5-5)) due to the additional constraints in the regression model. To formulate the problem conveniently, let $x_{t,2}$ (i.e., dependent variable) and $x_{t+i,1}$ (i.e., explanatory variables) be denoted as y and x_i, respectively. The identification of the time-raised regression

model Eq. (5-5) can be reformulated as the following constrained Lasso problem,

$$\begin{gathered}\arg\min_{b_i} \ ||y - b_0 x_0 - \sum_{i=1}^{P} b_i x_i \,|| + \lambda \sum_{i=0}^{P} |b_i| \\ s.t. \ \ b_i b_{i+1} \geq 0, \ \ i = 1,2,\cdots,P-1 \\ |b_i| \geq |b_{i+1}|, \ \ i = 1,2,\cdots,P-1\end{gathered} \tag{5-9}$$

where λ is the tuning parameter and P is the maximum feasible order of the phase 2 model (i.e., a relatively big integer). The regularization term in the objective function encourages sparsity of the optimal solution, since only the p (an integer smaller than P) nearest future layers have a significant reheating effect on the current layer, as justified in Section 5.2.1. Then the estimated model order $\hat{p}$ is determined by the number of non-zero estimated coefficients $\hat{b}_i$ (exclude $\hat{b}_0$).

Due to the additional homogeneous ordered constraints, the optimization problem in Eq. (5-9) is nonconvex due to the following constraint with nonconvex set,

$$S = \{\mathbf{b} | b_i b_{i+1} \geq 0, |b_i| \geq |b_{i+1}|, i\} = 1, \cdots, P-1\} \tag{5-10}$$

To address this non-convex challenge, a two-level optimization algorithm termed homogeneous ordered lasso (HOLA) is developed in this study.

The main idea of the HOLA algorithm is to narrow down S as a convex subset without loss of optimal solution (level one) and then solve the problem as a lasso-type convex optimization (level two). First, S can be represented as a union of two convex subsets S_1 and S_2, as shown in Eqs. (5-11) and (5-12), respectively,

$$S_1 = \{\mathbf{b} | b_i \geq 0, b_i \geq b_{i+1}, i = 1,2,\cdots,P-1\} \tag{5-11}$$

$$S_2 = \{\mathbf{b} | b_i \leq 0, b_i \leq b_{i+1}, i = 1,2,\cdots,P-1\} \tag{5-12}$$

If S can be replaced by either S_1 or S_2, then the optimization problem Eq. (5-9) becomes convex.

Following this rationale, the aim in level one is to identify to which subset the optimal solution belongs. Actually this aim is equivalent to determining the sign of b_1. If the correlation between y and x_1 is positive, then $b_1 > 0$ and S_1 will be selected as the updated feasible set due to the homogeneity of the coefficients. On the contrary, S_2 will be selected if the correlation is negative. To determine $\text{sgn}(b_1)$, a natural idea is to use $\text{sgn}(x_1^T y)$ as an approximation, which is easy to solve. In the following, a mathematical proof (Proposition 5-1) is provided to delineate the correctness of this idea.

Proposition 5-1: The sign of $\hat{b}_1$ estimated by the optimization problem in (5-9) is consistent with $x_1^T y$, if $|x_1^T y| \geq \max|x_i^T y|$, where $i \geq 2$.

Proof: Expanding out the first term of the objective function in (5-9), and then it can be rewritten as

$$\arg\min_b (y^T y - 2y^T X b + b^T D b) + \lambda ||b||_1 \tag{5-13}$$

where $D = X^T X$. In Eq. (5-13), $y^T y$ can be discarded since it does not contain any of the variables of interests. Afterwards, (5-13) can be further represented as,

$$\arg\min_b \ -2y^T x_1 b_1 - 2\sum_{j=2}^{P} y^T x_j b_j + b^T D b + \lambda \sum_{i=1}^{P} |b_i| \tag{5-14}$$

Since we have $|x_1^T y| \geq \max|x_i^T y|$, then statistically the correlation between x_1 and y is higher than other (x_i, y), which implies b_1 is farther from zero than the other b_i. Subsequently, with the homogeneous ordered constraints, consider the optimal solution for b_1, namely, $\hat{b}_1$. If $\hat{b}_1$ such that $y^T x_1 b_1 < 0$, then there must exist a better solution $-\hat{b}_1$ to make the objective function (5-14) even smaller. Therefore, $y^T x_1 b_1 > 0$. Q.E.D.

Proposition 5-1 provides a theoretical support to determine $\text{sgn}(b_1)$ based on $x_1^T y$. In addition, if

there is no correlation between x_1 and y, then only x_0 needs to be fitted, which indicates that the reheating effect in the process is not significant. Therefore, before estimating $\mathrm{sgn}(b_1)$ in level one, a statistical hypothesis test for b_1 is necessary. If the correlation is significant, then choose the feasible subset S_1 or S_2. Otherwise fit $y = b_0 x_0$ and apply it to Eq. (5-5).

Afterwards, based on the selected convex feasible subset in level one, the updated optimization problem is convex. Considering the case $b_1 > 0$, then the problem can be rewritten as follows,

$$\begin{aligned} &\arg\min_{b_i} \ ||y - b_0 x_0 - \sum_{i=1}^{P} b_i x_i \,|| + \lambda \sum_{i=0}^{P} b_i \\ &s.t. \ b_{i+1} - b_i \geq 0, \ \ i = 1,2,\cdots,P-1 \end{aligned} \tag{5-15}$$

It can be seen that the problem has been converted to a standard quadratic programming problem. A similar result can be obtained as well if $b_1 < 0$. Therefore, the standard quadratic optimization algorithm [121] is utilized at level two to obtain the optimal solution for the constrained Lasso problem. The detailed procedures of the HOLA algorithm are summarized in Figure 5-6.

Algorithm 5-1: HOLA Method
Input: $\boldsymbol{X} = [\boldsymbol{x_0}, \boldsymbol{x_1}, \cdots, \boldsymbol{x_P}] \in \mathbb{R}^{N\times(P+1)}$, $\boldsymbol{y} \in \mathbb{R}^N$
Output: Estimated coefficients $\{b_i, i = 0,1,\cdots,P\}$ and estimated order $\hat{p}$
Step 1 Calculate $\mathrm{sgn}(x_1^T y)$ and test correlation between $\boldsymbol{y}$ and $\boldsymbol{x_1}$
Step 2 If no correlation, fit $y = b_0 x_0$ and output. Otherwise go step 3
Step 3 Use S_1 (positive) or S_2 (negative) to replace the current feasible set S
Step 4 Solve the updated problem by the standard quadratic optimization algorithm

Figure 5-6: The developed HOLA algorithm

Based on the proposed HOLA method, for a fixed λ, the global optimal solution can be obtained in an efficient manner. Then the model identification for the phase 2 model can be implemented by testing different values of λ using the HOLA algorithm, e.g., based on cross validation [122].

In addition, regarding the confidence interval of the estimated coefficient, typically it can be implemented by bootstrap [123]. After the parameter estimation, this EAR$(1, -\mathrm{p})$ model is able to forecast $\boldsymbol{x}_t$ with consideration of the reheating effect, which is presented in Section 5.2.4.

5.2.4 Online quality forecasting in AM processes

The HOLA method proposed in Section 5.2.3 provides an effective approach to quantify the reheating effects by fitting the phase 2 model in Eq. (5-5). Then with the estimated model and observed sensor data, the state of the current layer $\boldsymbol{x}_t$ can be forecasted by taking into consideration the impact from both past and future layers. Specifically, phase 1 sub-state $x_{t,1}$ can be measured directly in general [15, 124]. In addition, the phase 1 model of Eq. (5-4) proposed in Section 5.2.2 also enables a direct forecast for $x_{t,1}$ based on $x_{t-1,1}$ [119]. On the other hand, the forecast for phase 2 sub-state $x_{t,2}$ is challenging due to the twofold causes, (1) $x_{t,2}$ is the state after reheating, i.e., the final status of layer t; (2) the previous layer will be blocked by the new deposited layers, hence it may be technically difficult to measure $x_{t,2}$ directly in general. Therefore, this section focuses on how to implement online forecast of $x_{t,2}$.

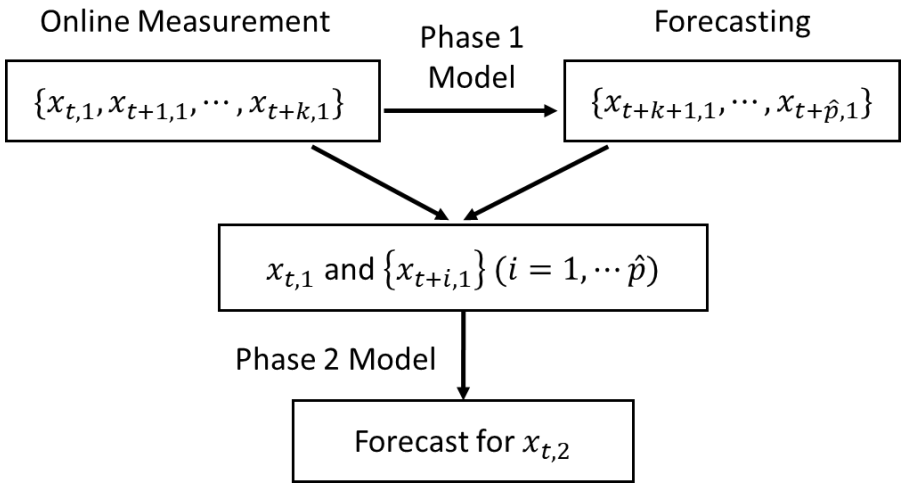

Figure 5-7: Procedure to online forecast $x_{t,2}$ based on $EAR(1, -p)$ model

In general, the overall framework to implement online quality forecasting is illustrated in Figure 5-7. Considering the real-world scenario of AM processes online monitoring, with effective sensing devices, assume both $x_{t,1}$ and all $\{x_{t+i,1}\}$ in Eq. (5-5) are known. Then the phase 2 model in Eq. (5-5) is used for forecast of $x_{t,2}$, which is based on the result of the phase 1 model. Under this circumstance, the online quality forecasting for the mean value of $x_{t,2}$ can be implemented as follows,

$$\hat{x}_{t,2} = \hat{b}_0 x_{t,1} + \sum_{i=1}^{\hat{p}} \hat{b}_i x_{t+i,1} \tag{5-16}$$

Then the next step is to estimate the confidence interval of $\hat{x}_{t,2}$. To achieve this, the key is to estimate the forecasting error. If all $\{x_{t+i,1}\}$ are known, then the only forecasting uncertainty comes from the error of model fitting by HOLA, which can be estimated by bootstrap, as mentioned in Section 5.2.4. Then the confidence interval of $\hat{x}_{t,2}$ can be represented as follows using bootstrap [125],

$$(\hat{x}_{t,2} - \hat{e}^{2.5}, \hat{x}_{t,2} + \hat{e}^{97.5}) \tag{5-17}$$

where $\hat{e}^{2.5}$ and $\hat{e}^{97.5}$ are the 2.5% and 97.5% percentiles of the bootstrap forecasting errors $\hat{e}$, respectively, for a 95% confidence interval.

Additionally, it is also possible that the information of phase 1 sub-state $\{x_{t+i,1}\}$ in Eq. (5-16) is only partially known, i.e., some influential future layers have not been deposited yet. However, $x_{t,2}$ is still of interest for forecasting. Without loss of generality, suppose layers $\{t, \cdots, t+k\}$ have been deposited but layers $\{t+k+1, \cdots, t+\hat{p}\}$ have not yet. Then in order to forecast $x_{t,2}$, since some of $\{x_{t+i,1}\}$ are unknown, they need to be forecasted first, which can be obtained by the fitted phase 1 model, i.e., Eq. (5-4). Afterwards, the mean value of $x_{t,2}$ can be estimated as below using

phase 2 model,

$$\hat{x}_{t,2} = \hat{b}_0 x_{t,1} + \sum_{i=1}^{k} \hat{b}_i x_{t+i,1} + \sum_{j=k+1}^{\hat{p}} \hat{b}_j \hat{x}_{t+j,1} \tag{5-18}$$

where $\{\hat{x}_{t+j,1}\}$ are the forecasted phase 1 sub-state value, which have not been deposited yet.

5.3 Numerical simulation studies

The objective of this numerical simulation study is to validate the performance of model estimation and online forecasting accuracy. In this case, the datasets with layer-wise reheating relationships are numerically generated from an $\mathrm{EAR}(1,-2)$ model. Specifically, the phase 1 model is an $\mathrm{AR}(1)$ model with $\mu = 5$ and $a = 0.2$, as shown in Eq. (5-19),

$$x_{t,1} = \mu + 0.2 x_{t-1,1} + \epsilon_{t,1} \tag{5-19}$$

And the phase 2 model is a second order time raised regression model, as shown in Eq. (5-20),

$$x_{t,2} = 0.8 x_{t,1} + 0.5 x_{t+1,1} + 0.3 x_{t+2,1} + \epsilon_{t,2} \tag{5-20}$$

where $\sigma_1 = 0.2, \sigma_2 = 0.3$. To validate the mode estimation performance of the proposed HOLA algorithm (with λ chosen by cross-validation), the step regression based on common criterions (AIC and BIC) and Lasso (with λ chosen by cross-validation as well) are selected as benchmark methods.

First, a single dataset with 100 simulated continuous layers is generated. Then the proposed and benchmark methods are performed using this dataset. As shown in Table 5-1, comparing the true value of the model parameters, the proposed method HOLA achieves a higher accuracy than the benchmark methods. In addition, the order of model is also successfully identified by HOLA, which outperforms the benchmark methods. Moreover, considering the capability of online application, the computational time for model fitting is about 0.15s on average (with Intel® Xeon®

Processor E3-1220 v3 at 3.10GHz). Compared with the typical printing time for each layer in practice, the computational time is fast enough.

Table 5-1: Model-fitting performance comparison between the proposed HOLA and benchmark methods

Fitting Methods	Model Parameters (true values)			
	b_0 (0.8)	b_1 (0.5)	b_2 (0.3)	p (2)
Stepwise (AIC)	0.89	0.47	0.37	3
Stepwise (BIC)	0.89	0.47	0.37	3
Lasso	0.76	0.57	0.26	3
HOLA (proposed)	**0.82**	**0.49**	**0.28**	**2**

To validate the forecasting accuracy of the proposed EAR model, a layer-wise online forecast with 95% confidence interval is performed to compare with the actual value (see Figure 5-8). In this case, using $x_{t,1}$, $x_{t+1,1}$ and $x_{t+2,1}$ to forecast $x_{t,2}$, the testing data is a new simulation set with 50 pairs of observations from the same model. The results show that the fitted model can provide an effective forecast, which is very close to the actual value. In addition, the forecasting performance between classical AR(1) (i.e., ignore reheating effect) and the fitted EAR$(1,-2)$ is also compared in terms of the averaged absolute relative error based on the forecast of $\{x_{t,2}, x_{t+1,2}, x_{t+2,2}\}$ without the information of $\{x_{t+3,1}, x_{t+4,1}\}$. The results (see Table 5-2) show that the forecasting error of the EAR model is significantly lower than the existing AR model.

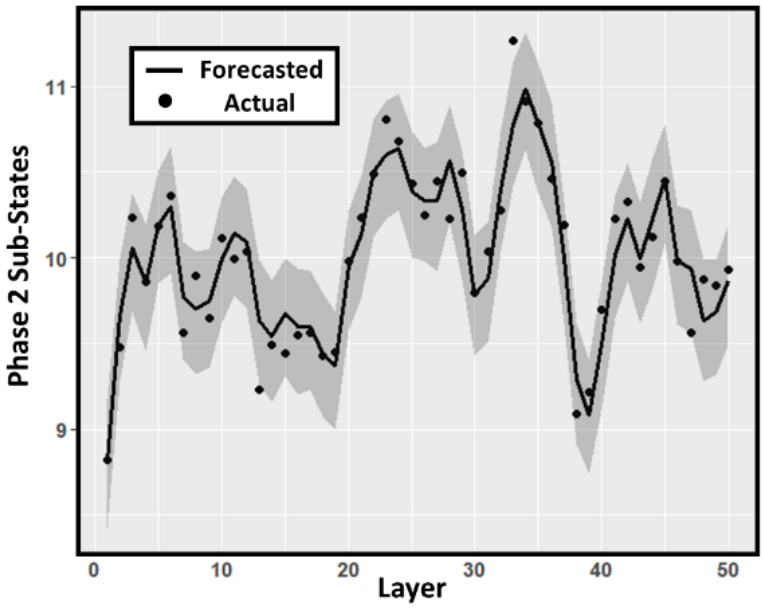

Figure 5-8: The results for the dynamic 1-step forecasting by using the fitted $EAR(1,-2)$ model. The solid line and gray area represent the forecasted mean value and 95% confidence interval, respectively.

Table 5-2: Accuracy for 3-layer forecasting by the classical $AR(1)$ and proposed $EAR(1,-p)$.

Layers to be forecasted	**Models to do forecasting**	
	AR(1)	**EAR$(1,-2)$**
1st Layer ($\|e\|$%)	5.9%	**0.4%**
2nd Layer ($\|e\|$%)	11.9%	**1.5%**
3rd Layer ($\|e\|$%)	14.4%	**2.1%**
Averaged (%)	10.7%	**1.3%**

5.4 Case studies

To validate its effectiveness in real-world AM applications, this section further validates the performance of the proposed method based on an actual 3D printing process. The objective of the case study is to achieve online layer-wise geometrical deviation forecasting in an FFF process [1]. In this study, the average geometrical deviation in the front edge of each layer is considered the

quality characteristics of interest (namely, the state of each layer) to measure and forecast, which is a very common type of variability caused by the reheating effect.

5.4.1 Experimental setup and tests

The experimental platform for the case studies consists of an FFF-based 3D printer and an online 3D structured light scanning system (Figure 5-9(a)). The digital 3D scanner (Figure 5-9(b)) is a fast and effective device to implement non-contact high accuracy measurement for layer-wise geometrical deviation. The basic principle of the 3D scanner is based on high-resolution image acquisition and efficient 3D reconstruction algorithms. The output of the scanning result is 3D point cloud data (Figure 5-9(c)) and it takes less than one second to scan each layer. Further detailed technical information of this type of 3D scan technology is available in Ref. [126, 127].

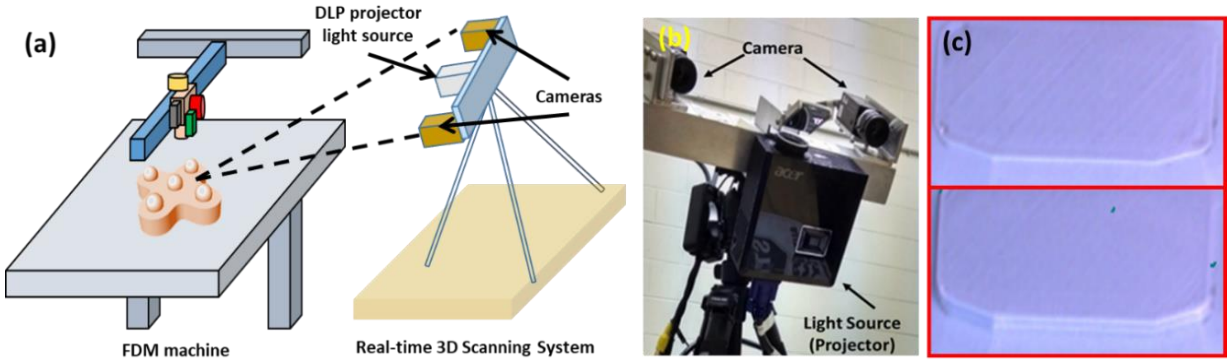

Figure 5-9: (a) The scheme of the 3D scan system; (b) the digital 3D scanner; (c) two sample scanned layers.

Based on the developed 3D printing and online 3D scan platform, the following case studies are conducted.

1) Case E1: A small cuboid with dimension 8mm×8mm×20mm (see Figure 5-10(a)). Since the area for the each layer is small (16 mm^2), the printing of one layer is very fast so that

each layer will be reheated after a short time. Hence, the reheating effect will significantly impact the solidification process.

2) Case E2: A relatively big model with dimension 70mm × 35mm × 20mm (see Figure 5-10(b)). Although each layer has enough time to solidify and cool down, the layer will still be reheated and the dimension deviation may occur in the edge regions.

During the printing experiments, the printing process was paused when the one layer was finished, and then the 3D scan was conducted subsequently. The process would be resumed immediately after the scan was complete. The time for each scan is 4-6 seconds (pause, scan, and resume) per layer, which is sufficient to perform online data acquisition and monitoring.

For both case studies, the side surfaces at the front edge of the parts were fully scanned and the point cloud data for each printed layer was collected. For each scanned layer, only the points within the ROI (the white region in Figure 5-10) are used for analysis. Subsequently, the actual layer-wise geometrical deviation in x direction (Figure 5-10) was obtained by comparing the 3D point cloud with the original CAD model.

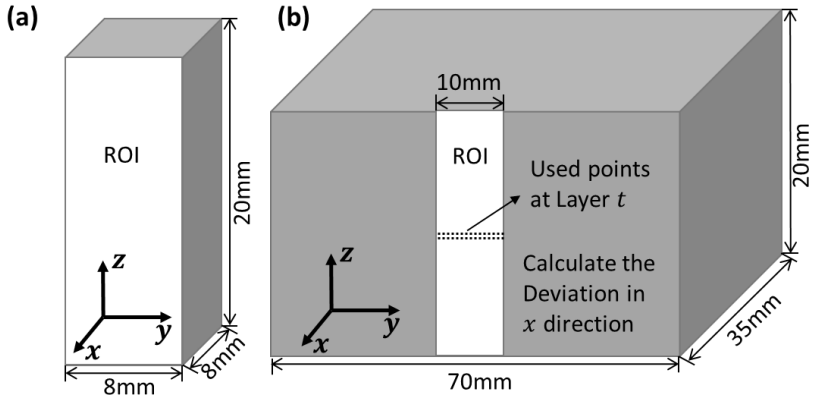

Figure 5-10: The designed samples for case studies, (a) a designed part for case E1; (b) a designed part for case E2. The white region is the ROI and only the points within the ROI are used for analysis.

In this case, the spatial resolution is about 16-25 points within 1 mm^2 (i.e., 4-5 points with 1 mm). Since the setting of layer thickness is 0.3mm, the geometric deviation for all of the printed layers can be obtained from the point cloud. In the case study, the average deviation of the scanned points with ROI in each layer (about 30-40 points and 40-50 points in each layer for case E1 and E2, respectively) is used as the quality characteristic for analysis.

5.4.2 Application and validation of the EAR model in FFF

As described in Section 5.4.1, the data collected from the front side of the parts (demonstrated in Figure 5-10(b)) are utilized as the ROI to perform the analysis. Specifically, the proposed EAR$(1,-\mathrm{p})$ model is fitted by using the data of 20 scanned layers for case E1 and case E2, respectively. Afterwards, the forecasting performance of the trained models is validated using additional scanned 20 layers.

The model estimation results are listed in Table 5-3. For both cases E1 and E2, with the fitted phase 1 model, the order of the estimated phase 2 model, i.e., the value of $\hat{p}$, is 1, which means only the nearest future layer has significant impact for the current layer. The main reason is that the layer thickness in FFF is usually relatively high (0.3mm in this study), and thus the future layers do not have enough heat to penetrate the immediate future layer to reheat the current layer.

Table 5-3: Model estimation results for case E1 and E2. $\hat{a}$ and $(\hat{b}_0, \hat{b}_1)$ are the estimated coefficient of phase 1 and phase 2 model, respectively.

Fitting results	**Case E1**	**Case E2**
Model order ($\hat{p}$)	1	1
$\hat{a}$ (p-value)	0.26 (<0.1)	0.24 (<0.1)
$\hat{b}_0$ (p-value)	0.18 (<0.05)	0.95 (<0.001)
$\hat{b}_1$ (p-value)	0.86 (<0.001)	0.06 (<0.01)

The estimation of model coefficients in case E1 demonstrates that the value of $\hat{b}_1$ is relatively large compared to $\hat{b}_0$, i.e., the reheating effect produces the major contribution to geometric deviation. In this case, the area of each layer is small, which means that the deposited materials in the previous layers do not have sufficient time to fully solidify, and the reheating effects will therefore result in significant geometric deviation. On the contrary, in case E2, due to the relatively large area of each layer, the deposited material has enough time to be solidified. Consequently, the impact from the future layers should be much lower than case E1, which causes a large $\hat{b}_0$ but small $\hat{b}_1$.

Then the online forecasting performance is validated by the estimated models. First, using $x_{t,1}$ and $x_{t+1,1}$ to forecast $x_{t,2}$, the results for cases E1 and E2 are presented in Figure 5-11 and Figure 5-12, respectively. The forecasted mean value and 95% confidence interval of both cases are close to the actual measurement.

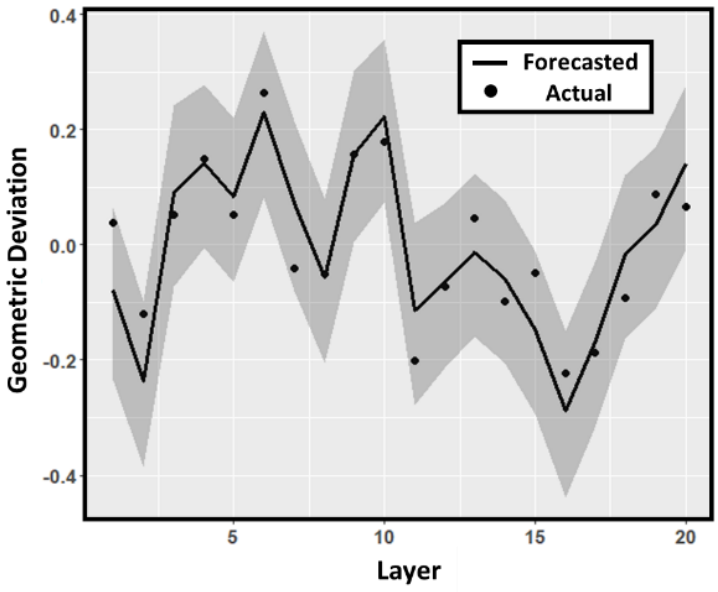

Figure 5-11: The forecasted vs. actual values of edge dimension deviation at each layer for case E1. The solid line and gray area represent the forecasted mean value and 95% confidence interval, respectively.

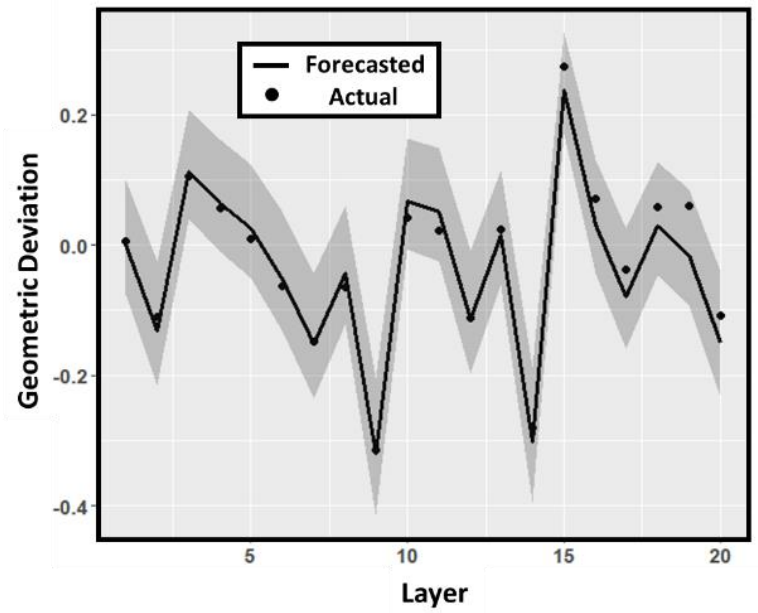

Figure 5-12: The forecasted vs. actual values of edge dimension deviation at each layer for case E2. The solid line and gray area represent the forecasted mean value and 95% confidence interval, respectively.

Subsequently, consider the forecast of $\{x_{t,2}, x_{t+1,2}\}$, in which $\{x_{t,1}, x_{t+1,1}\}$ are known but $x_{t+2,1}$ is unknown. To validate the effectiveness of the proposed EAR model, the ARIMA time series model is applied as a benchmark method to do comparison. The averaged forecasting errors are listed in Table 5-4. For the results of the benchmark method, the analysis starts from the ARIMA(p, d, q) model, and the automatic order determination algorithm finally shows that the optimal model is AR(1) for both E1 and E2. Then compared with the forecasting results from the fitted AR(1) model, the proposed model provides a significant performance improvement in terms of the forecasting error. Therefore, the proposed model is very effective to handle the layer-wise geometrical deviation caused by reheating effects.

Table 5-4: Model fitting results and forecasting performance compared with the benchmark AR(1).

Forecasting results ($\bar{e}$%)	**Case E1**		**Case E2**	
	AR(1)	EAR(1, −1)	AR(1)	EAR(1, −1)
1st layer	14.7%	**2.8%**	13.2%	**2.4%**
2nd layer	18.5%	**6.6%**	12.1%	**5.8%**
Average	17.1%	**4.7%**	12.7%	**4.1%**

5.5 Conclusions

This chapter developed a novel bilateral time series model termed EAR(1, −p) for online forecast of the layer-wise quality characteristics in AM processes. The novelty of the approach is that it considers the effect of not only previous but also subsequent layers on the current one. This bilateral aspect is the key to understanding the effect of reheating phenomena in AM, wherein a layer is repeatedly heated by subsequent layers. As a result, this work enables accurate modeling of quality characteristics affected by the reheating phenomenon, such as geometric deviation. Consequently, this chapter addresses one of the significant challenges regarding the quality issues in AM applications.

The effectiveness and efficiency of this approach are validated using numerical simulation study, finite element AM simulations, and real world study of layer-wise geometric deviation of AM parts. The proposed bilateral time series model effectively captures the impact of reheating phenomenon. With the developed model estimation method HOLA, the reheating effects can be quantified accurately. In contrast, the traditional time series model is not able to consider and quantify the effects from future layers. The relative forecasting error of the proposed model is typically under 5%, which is much more accurate than the performance of the benchmark methods (>10%). Therefore, the proposed method significantly outperforms the traditional time series

models such as AR(1).

6 An image-based closed-loop quality control approach for online defect mitigation

One of the major challenges in the AM industry is how to ensure product quality and consistency by detecting and then mitigating the defects, which otherwise can severely deteriorate the quality of AM products and even the sustainability of AM technology. Although optimizing machine parameter settings offline and post-processing of AM products can improve the quality, the effects may be still limited, particularly for the parts with complex geometries. The objective of this chapter is to develop an image-based closed-loop quality control system for a typical AM process, namely, fused filament fabrication (FFF). This system is implemented by a customized online image acquisition system with a proposed image diagnosis-based closed-loop quality control method. Based on this novel approach, the typical quality issues can be addressed by efficient and effective defect mitigation via online automatic machine parameter adjustment. The case studies based on an actual FFF platform demonstrate the effectiveness and applicability of the proposed approach.

6.1 Introduction

The frequently occurring defects of FFF include voids, over-fill, under-fill, etc. [43, 52] (a typical under-fill defect is shown in Figure 6-1(b)). Some of these defects can be avoided by optimizing the machine parameter settings before printing via design of experiments (DoE) or eliminated by post-processing after printing. However, due to the highly complex interactions in consecutive layers during printing, especially with varying cross-sectional geometries, large process variations may still occur, which ideally require changing machine parameters continuously during printing,

and thus cannot be resolved by offline optimal parameter settings, i.e., design of experiments (DoE). Post-processing, such as machining or polishing, is only effective for the external surface quality of AM parts. However, some typical defects, such as over-fill and under-fill (Figure 6-1(c)), occur in between layers that exist inside of the printed parts, and consequently cause severe deterioration in the quality of AM products in terms of strength, internal structure precision, and surface quality [43, 128].

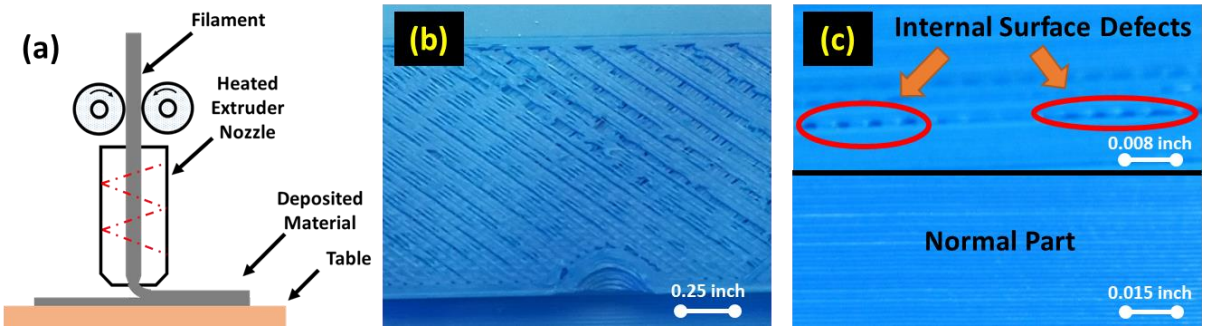

Figure 6-1: (a) Schematic of the FFF process; (b) typical under-fill defects occurring in the FFF parts (top view); (c) the internal surface defects (under-fill) occurring between layers (side view).

To further justify the significance of this research challenge, i.e., DoE is not sufficient to eliminate the defects even if the predefined machine parameters are already "optimal", a preliminary experiment for a part with simple geometry was conducted to verify the common existence of the in-process quality issues. A typical cuboid with side length of two inches was designed as a testing artifact. Then through DoE (the procedure is discussed in detail in Section 6.3.2), the optimal parameter settings can be obtained. Based on the optimal settings, most of the printed testing artifacts are of good quality, however defects still occur in a few samples. For the defective samples, the surface quality is defect-free at the beginning of the printing process. However, due to the accumulation of the process uncertainties from different sources, e.g., extrusion and machine vibration, some non-negligible under-fill defects were observed in the subsequent layers (Figure 6-2).

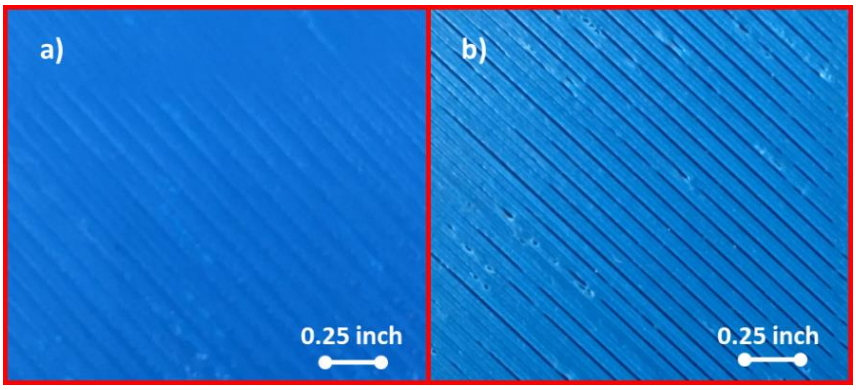

Figure 6-2: The under-fill defects occurred in the testing artifact during printing based on the predefined "optimal machine parameters", (a) normal printing at the beginning; (b) under-fill defects observed during printing.

Therefore, due to the occurrence of defects, the predefined "optimal machine parameters" are no longer considered optimal, which implies that the machine parameters need to be adjusted in order to maintain good quality of the parts. Even though the offline quality assurance techniques such as DoE can obtain excellent initial machine settings of the process, the experiment planning still cannot guarantee the perfect elimination of defects during printing even for the parts with simple geometry. The main explanation of this observation may be that some significant factors were not included in the machine parameters, such as the thermal variations between layers due to the physics of the FFF process, which belong to a nuisance factor that cannot be controlled by machine parameters. If the machine cannot perfectly control those factors, the defects may occur and accumulate during the printing process.

To ensure the quality of AM parts, an effective real-time *in situ* feedback quality control system for AM processes is needed to diagnose the defects and adjust the machine parameters automatically to mitigate defects [15, 28, 129]. To achieve this objective, this chapter proposes an image analysis-based feedback quality control approach for the FFF process. The applicability of the proposed approach is demonstrated by using the acquired image data from the experiments

collected on an actual FFF platform. Accordingly, in this work, our investigation was accomplished through the following three major tasks:

(1) An FFF-based real-time image acquisition system was developed, which can capture the high-resolution images for monitoring the surface quality of the material being extruded.
(2) The relationship between the severity of occurring defects in FFF and the related machine parameters was identified using experimental studies.
(3) An effective image-based classification method was implemented to diagnose specific defects and was integrated with a Proportional-Integral-Derivative (PID) based feedback quality control mechanism so that automatic parameter adjustment can be enabled when defects occur during the printing process.

The rest of this chapter is organized as follows. The experiment setup and the significance of the problem are presented in Section 6.2. The proposed research methodology is introduced in Section 6.3, followed by the case studies for testing and validation of the proposed approach in Section 6.4. Finally, the conclusions and future work are discussed in Section 6.5.

6.2 Experimental platform development

A desktop FFF 3D printer, a Hyrel System 30M 3D printer, was used to conduct the experiments (see Figure 6-3(a)). The machine has an extruder with 0.5mm nozzle diameter and uses acrylonitrile butadiene styrene (ABS) with a diameter of 1.75mm as filament for printing. The printer comes with an enclosed chamber, which is an important feature to ensure the printing quality since it can reduce the influence of ambient temperature variations. Another excellent feature of this printer is that it deploys an open communication-based software controller, with

which an external computer/program can directly communicate to adjust the machine parameters (in the form of G-code) online during the printing process (Figure 6-3(b)).

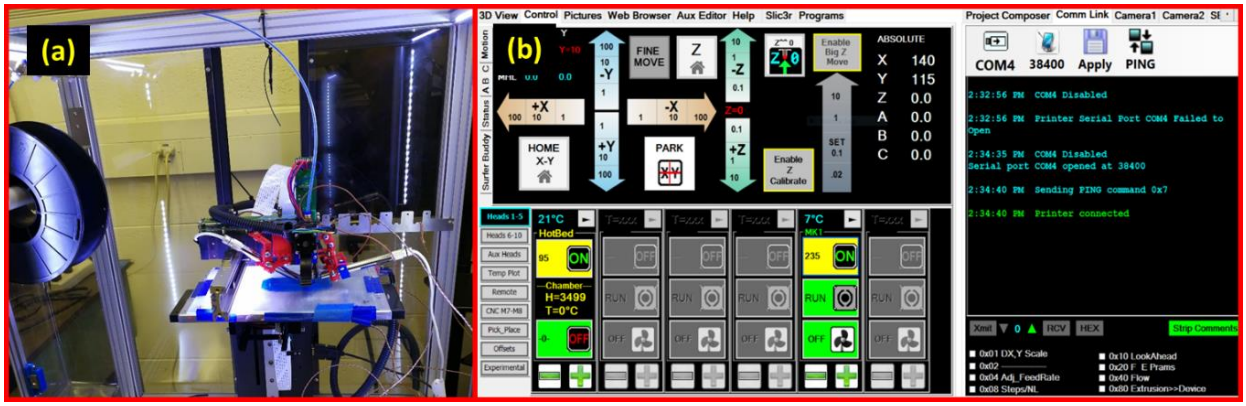

Figure 6-3: The selected experimental platform, Hyrel System 30M 3D printer. (a) Overall setup; (b) the control panel with an external interface.

The developed image acquisition system consists of two digital microscopes with an adjustable sampling frequency (Figure 6-4), which were mounted near to the extruder of the 3D printer to collect high-quality images of the surface of the printed part surface. In order to avoid blind spots during data collection, the microscopes were installed on opposite sides of the extruder (Figure 6-4(b)). The image resolution for online acquisition is 640×480 pixels at a typical sampling frequency of 1 Hz. For other types of AM processes, similar image acquisition system can be implemented as well according to the recent related work [26, 130, 131].

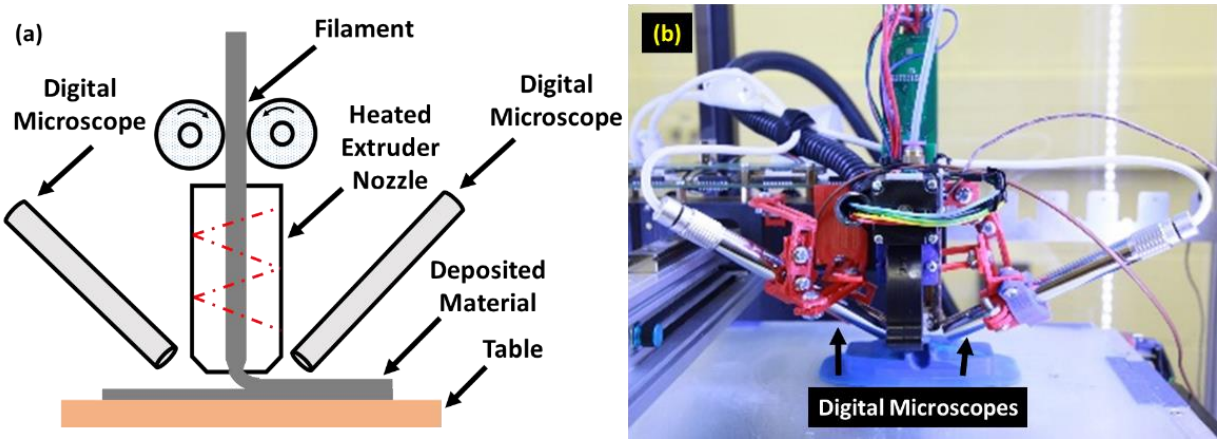

Figure 6-4: (a) The designed image acquisition system; (b) the actual setup in the test platform.

The overall architecture of the experimental closed-loop quality control system is illustrated in Figure 6-5. The communication between the 3D printer and the external program for defect detection and mitigation was implemented through virtual serial ports (RS-232). The basic procedure is to convert the commands for machine parameter adjustment to corresponding G-codes and then send them to the printer through the virtual serial ports. Certain delays were observed for the G-codes to be executed from the time they were received. Based on our experiments, the delays for adjustment of cooling fan and flow rate were quantified in Table 6-1.

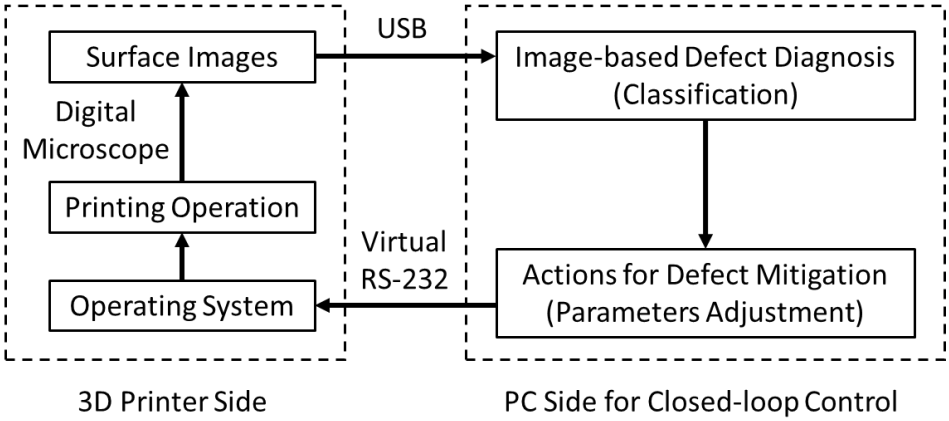

Figure 6-5: The overall architecture of the designed closed-loop quality control system with machine-computer interaction.

Table 6-1: Delay of machine response to parameter adjustment.

Action	Trial 1	Trial 2	Trial 3	Trial 4	Trial 5	Average (Stdev)
Turn on cooling fan	1.84s	1.85s	1.46s	1.75s	1.47s	1.67s(0.19s)
Turn off cooling fan	1.16s	1.86s	1.51s	1.05s	1.39s	1.39s(0.32s)
Change flow rate	2.86s	2.44s	3.73s	4.92s	3.16s	3.42s(0.96s)

6.3 Research methodology

Based on the developed online data acquisition system, this section aims to implement online defect mitigation by automatic machine parameter adjustment.

6.3.1 Methodology overview

The overall proposed research methodology in this study is summarized in Figure 6-6, which consists of the following three major steps:

(1) Experimental design study: The relationship between the selected typical defects and machine parameters is investigated using an experimental design, which is presented in Section 6.3.2. Meanwhile, the image data collection and labeling procedure is introduced as well.

(2) Defect diagnosis algorithm: A textural analysis-based image classification algorithm for surface defect recognition is developed in Section 6.3.3.

(3) Defect mitigation strategy: A PID equation-based feedback quality control system for automatic machine parameter adjustment was implemented to mitigate the defects in Section 6.3.4.

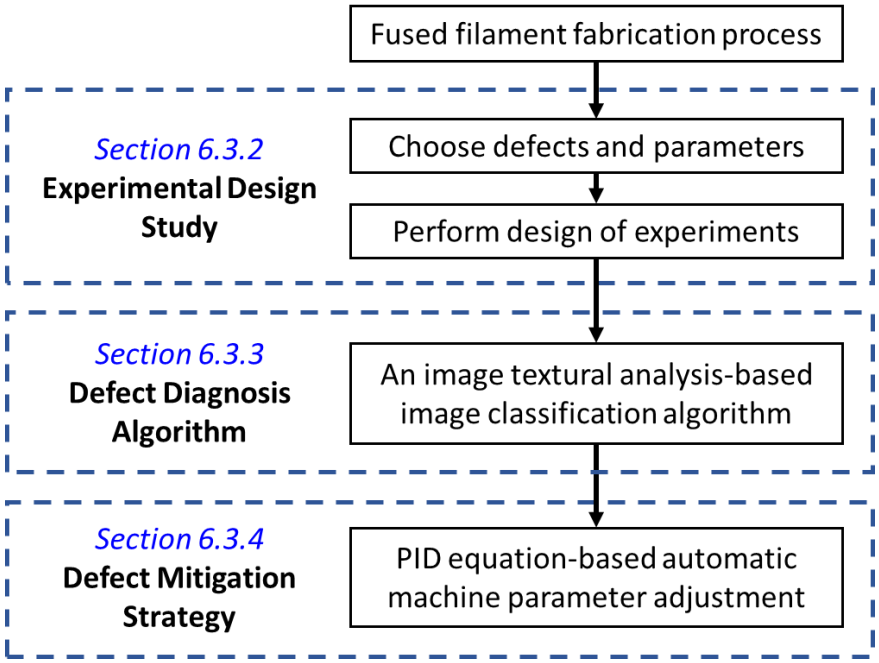

Figure 6-6: Framework of the proposed research approach integrating experimental study, diagnosis algorithm development, and control system design for online closed-loop quality control.

6.3.2 Experimental design study

The objective of the experimental design study is to understand the relationship between online adjustable machine parameters and printing defects. Based on this relationship, the feedback quality control system can identify which parameter should be adjusted when defects occur during printing.

To identify this relationship, the appropriate defects and adjustable machine parameters must be determined. For the adjustable machine parameters, based on the control capability of the 3D printing platform and the existing literature [11, 44, 132], three parameters including material flow rate (R), extruder temperature (T), and layer height (H) were selected. Specifically, R refers to the rate at which material is being extruded through the nozzle; T controls the extruder temperature and governs the viscosity of the extrusion; and H represents the nominal distance between the nozzle tip and the part surface. All three parameters may possibly have impacts on the occurrence of defects during printing. The nozzle feed rate (travel speed in the horizontal plane) was not selected as a factor since it cannot be adjusted online during printing in the 3D printer used in this study. For the defects of interest, two commonly occurring surface defects in FFF, namely, under-fill and over-fill are chosen for the investigation [43]. The test artifact is a cuboid of dimensions 2 inches × 2 inches × 2 inches as introduced in Section 6.1.

To identify the relationship model between the selected parameters and defects in this study, a full factorial experimental design [133] is applied, and the severity of defects is chosen as the output. The results of these experiments can provide a strategy to mitigate the defects effectively. The experimental runs were designed at two levels of the three selected machine parameters, namely, a 2^3 full factorial experimental design is utilized (Table 6-2). With two replicates a total of 16 runs

were performed and the experimental results are presented in Table 6-3. The results listed in Table 6-3 present the printing quality of each experiment. The experimental conditions that result in a normal printing process (i.e., no defect occurs) are defined as optimal machine parameters. Then different types of printing defects are also marked based on the collected images.

Table 6-2: The treatment conditions for defects investigation in experimental studies.

Machine Parameters	**Level of Treatment**	
	For Under-fill	**For Over-fill**
Extruder temperature (T)	200/230°C (low/standard)	230/250°C (standard/high)
Material flow rate (R)	50/100% (low/standard)	100/150% (standard/high)
Nozzle height for flow (H)	0.3/0.4mm (standard/high)	0.2/0.3mm (low/standard)

Table 6-3: The full factorial design table and experiments results.

Treatment Conditions	**T**	**R**	**H**	**Results**
TC1	230°C	100%	0.3mm	Normal printing
TC2	230°C	100%	0.4mm	Normal printing
TC3	230°C	50%	0.3mm	Under-fill with regular pattern
TC4	230°C	50%	0.4mm	Under-fill with regular pattern
TC5	200°C	100%	0.3mm	Under-fill with irregular pattern
TC6	200°C	100%	0.4mm	Under-fill with irregular pattern
TC7	200°C	50%	0.3mm	Severe under-fill (low extrusion)
TC8	200°C	50%	0.4mm	Severe under-fill (low extrusion)
TC9	230°C	100%	0.3mm	Normal Printing
TC10	230°C	100%	0.2mm	Normal Printing
TC11	230°C	150%	0.3mm	Over-fill
TC12	230°C	150%	0.2mm	Over-fill
TC13	250°C	100%	0.3mm	Normal printing
TC14	250°C	100%	0.2mm	Normal printing
TC15	250°C	150%	0.3mm	Over-fill (wider spread extruding)
TC16	250°C	150%	0.2mm	Over-fill (wider spread extruding)

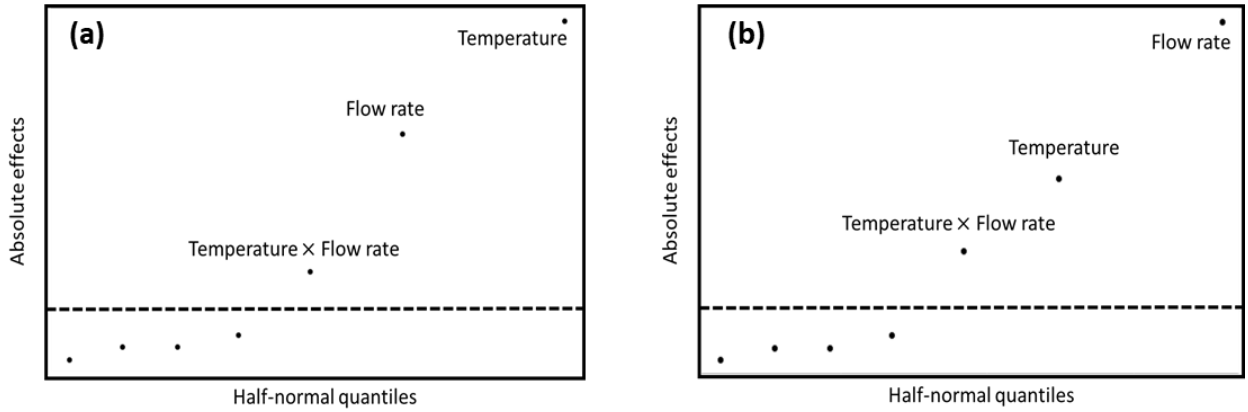

Figure 6-7: The half-normal to show the statistical significance of each effect for (a) under-fill and (b) over-fill experiments.

The experimental results show that material flow rate R and extruder temperature T, as well as their interaction, significantly affected the printed surface quality, as evidenced by the half-normal plot in Figure 6-7. More specifically, it can be observed that an inappropriate setting for material flow rate R caused under-fill defects with regular pattern (50% flow rate, Figure 6-8(a)) and over-fill defects (150% flow rate, Figure 6-8(b)). For the effect of extruder temperature T, the experimental results indicated that low temperature led to the under-fill defect with irregular pattern (Figure 6-8(c)). This is because low temperature will reduce the material flowability, which may cause the voids between printing tracks. In addition, if flow rate R is suboptimal, an inappropriate extruder temperature T will cause even more serious defects (i.e., interaction effect). The result also showed that the machine parameter H did not significantly affect the surface quality (Figure 6-8(d), when H is higher than the standard setting). The range of H is between 0.2mm and 0.4mm on the Hyrel 30M 3D printer, and it is set as 0.3mm in this study.

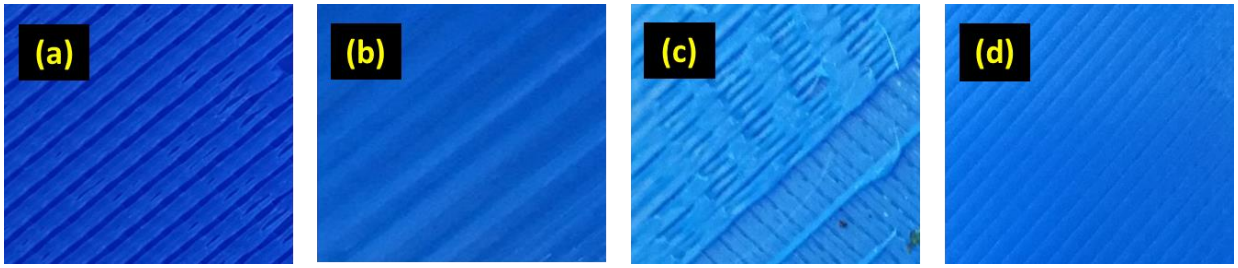

Figure 6-8:: (a) Under-fill defects with regular pattern caused by low flow rate R; (b) Over-fill defects caused by high flow rate R; (c) Under-fill defects with irregular pattern caused by low temperature T; (d) no significant defects occur when nozzle height H is higher than the standard.

In this study, to detect defects online during printing, the supervised classification method using image data (based on the data collection system shown in Figure 6-4) is utilized. Therefore, apart from utilizing DoE to identify the defect-parameter relationship, extensive experiments are also performed to collect training and validation data for image classification. Since the classification output will be used as input of the closed-loop quality control system, it is necessary to quantify the definition of the labels in mathematical formulas. To label the images, two key aspects should be considered, namely, types and severity. The type of defects shown in Table 6-3 can be represented by combination of two indicator variables $I_1(t)$ and $I_2(t)$, which are defined as follows,

$$I_1(t) = \begin{cases} 1 & \text{under} - \text{fill} \\ 0 & \text{normal} \\ -1 & \text{over} - \text{fill} \end{cases} \tag{6-1}$$

$$I_2(t) = \begin{cases} 1 & \text{caused by temperature} \\ 0 & \text{caused by flow rate} \end{cases} \tag{6-2}$$

These definitions are based on the defects categorized and listed in Table 6-3. Then for the severities, in this study, the defects with different severities are purposely generated by changing the specific machine parameters, e.g., setting flow rate R as 75% to generate 25% under-fill defects. For labeling purposes, the severity of defects is denoted as $s(t)$ by considering the root cause. Specifically, if $I_2(t) = 0$, then $s(t)$ is determined by the difference between the current and

optimal value of R. For example, for under-fill defects $I_1(t) = 1$, $s(t) = 0.25$ represents that only 75% materials are deposited compared with normal printing (i.e., the difference from the optimal setting is 25%). Otherwise if $I_2(t) = 1$, then define $s(t) = 1$ to represent the irregular under-fill defects caused by low temperature. Overall, the labels for image classification in this study are defined in Table 6-4.

Table 6-4: The defined labels for image classification.

Image label	Printing quality	Quantified classification output
0	Normal printing	$I_1(t) = 0, s(t) = 0$
1	25% Under-fill with regular pattern	$I_1(t) = 1, I_2(t) = 0, s(t) = 0.25$
2	50% Under-fill with regular pattern	$I_1(t) = 1, I_2(t) = 0, s(t) = 0.5$
3	125% Over-fill	$I_1(t) = -1, I_2(t) = 0, s(t) = 0.25$
4	Under-fill with irregular pattern	$I_1(t) = 1, I_2(t) = 1, s(t) = 1$

In the experiments, a significant decrease (from 230ºC to 200ºC) in the extruder temperature during printing was observed, which was caused by the cooling fan attached to the extruder. Conversely, turning off the cooling fan increased the extruder temperature quickly. Therefore, turning on/off the cooling fan is an effective action to adjust the extruder temperature. Although the 3D printer used in the experiments has a machine parameter that directly adjusts the extruder temperature, its actual response was observed to be slower than turning on/off the cooling fan. Therefore, turning on/off the cooling fan is used to adjust extruder temperature in this study for the closed-loop control purpose. As a summary, a qualitative relationship between defects and the related mitigation actions in this study is illustrated in Figure 6-9.

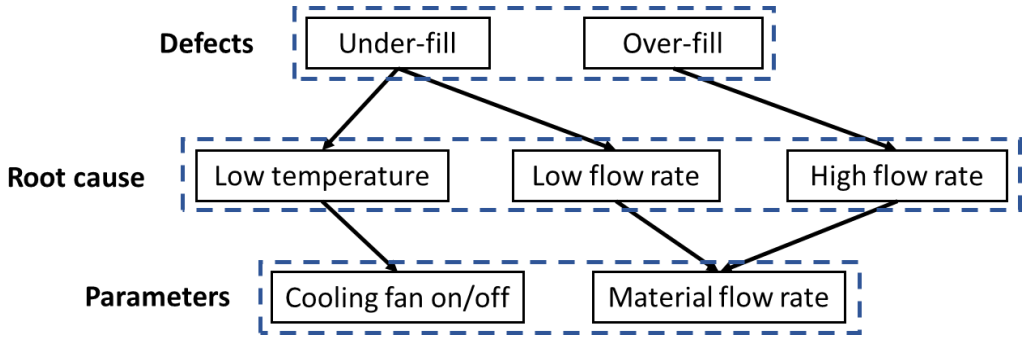

Figure 6-9: The causal relationship between defects and the related mitigation actions.

A timely adjustment of the machine parameters is critical, otherwise the deterioration of the surface quality of printed layers and failure of printing may occur. As shown in Table 6-5, the nozzle will be clogged within a short time (25s-30s) if the temperature of the extruder cannot be adjusted in time. The reason is that the filament is very difficult to be melted and extruded under low temperature. A similar problem for the over-fill defect may occur and can cause the printing process to stop since the excessive amount of filament cannot be deposited in time, thus blocking the nozzle. Although the under-fill defect will not cause clogging, the resulting low infill density will weaken the mechanical property of the printed part substantially [134, 135].

Table 6-5: The risk for process if no adjustment when defects occur.

Defects	Cause	Risk for process	Remarks
Under-fill	Temperature/Cooling fan	Clog in 25-30s	Under-fill rate will increase very fast
Under-fill	Material flow rate	Poor printing quality	Infill density will be very low
Over-fill	Material flow rate	Clog in 1-1.5min	Lots of filament unable to be deposited

6.3.3 Textural analysis-based image diagnosis (TA-ID) algorithm for defect detection

This section describes implementation of an online defect detection based on a textural analysis-based image diagnosis (TA-ID) algorithm. The image acquisition system introduced in Section 6.2 can collect image data in an online manner to monitor the surface quality of the part being printed.

In order to implement an effective automatic online adjustment of machine parameters, it is necessary to identify both types and severity of the occurring defects. Figure 6-1, Figure 6-2, and Figure 6-8 clearly show that the images of the printed surface have evident textural features under different printing quality conditions. Thus, the proposed TA-ID algorithm integrates the advantages of image textural analysis [136] and a supervised classification algorithm, so that the occurring defects can be identified accurately and quickly.

In this study, for each image a region of interest (ROI) was utilized, which was cropped from the original image (640 by 480 pixels) to a smaller region (80 by 80 pixels) right below the nozzle (Figure 6-10). Then, the raw RGB images were converted to grayscale to improve the efficiency of image analysis. Although the grayscale transformation may result in some information loss, most of the textural information representing the defects' characteristics is still preserved.

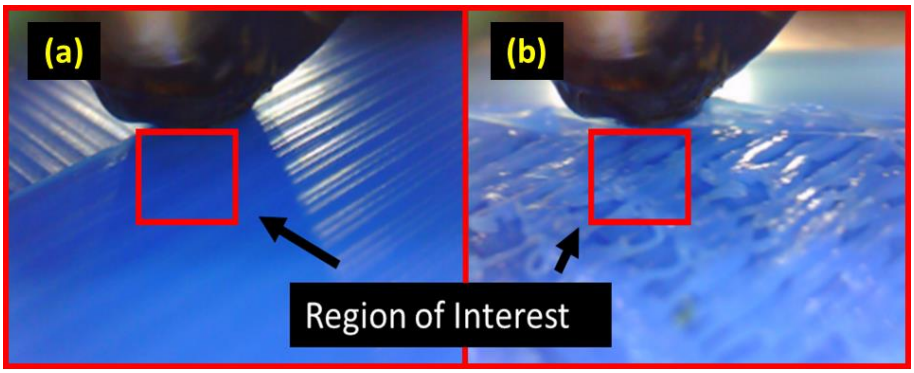

Figure 6-10: The real-time collected image samples and the region of interest. (a) Normal printing; (b) defects occurred.

It is observed that the defects with different type and severity have different textural characteristics. Thus, the proposed TA-ID algorithm utilizes an image textural feature extraction approach to improve the performance of image classification. The procedure of the feature extraction approach consists of two steps. The first step is to capture image textural information using the gray level co-occurrence matrix (GLCM) [137]. The second step is to extract the effective yet compact

features from the resulting GLCM. In order to achieve this, four typical statistics of GLCM, which is very effective to capture the spatial variation features, were utilized in this study. Through the experimental studies conducted in Section 6.3.2, the labels of the training images are identified based on the definition introduced in Section 6.3.2. Afterward, supervised classification algorithm (such as k-NN, SVM, LDA, etc.) is applied to detect the type of defects. Therefore, the overall framework of the proposed TA-ID algorithm can be summarized in Figure 6-11.

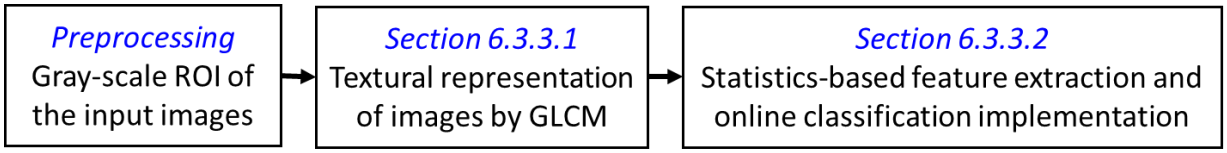

Figure 6-11: The framework of the proposed textural analysis-based image diagnosis (TA-ID) algorithm.

6.3.3.1 Textural representation via gray level co-occurrence matrix

Hypothetically, for the investigated FFF case, different types of surface defects can be identified by surface image textures. Since the collected image data contain various surface textural information, image texture analysis-based approaches have the potential to provide effective features for classification. One of the most effective image textural representations is called the co-occurrence matrix [138], which was chosen in this study because it can effectively describe the spatial correlation of the pattern in the images generated by tracks of printing [139] and therefore is the key feature to differentiate different levels of surface quality (normal, defective, etc.).

The co-occurrence matrix, also referred to as the co-occurrence distribution, represents the distance and angular spatial relationship over an image sub-region of a specific size [138]. In order to reduce the computational complexity of real world applications, the gray level co-occurrence matrix (GLCM) [140], which is transformed from a grayscale image, is commonly applied. More

specifically, for a grayscale image I with dimension $M \times N$, the GLCM of I, termed by G, is a matrix where the numbers of rows and columns are equal to the number of the gray levels in I. The element of G, $G(i,j|\Delta r,\Delta c)$ is defined by the occurring frequency of a two-pixel combination with intensity i and j respectively, and the spatial distance of these two pixel is defined by $(\Delta r,\Delta c)$. Suppose the number of gray levels in I is K, then the dimension of the corresponding GLCM will be $(K \times K)$, and the elements in GLCM can be obtained by,

$$G(i,j|\Delta r,\Delta c) = \frac{1}{(M-\Delta c)(N-\Delta r)} \sum_{m=1}^{M-\Delta c} \sum_{n=1}^{N-\Delta r} g \tag{6-3}$$

where

$$g = \begin{cases} 1 & if\ I(m,n) = i\ \ and\ \ I(m+\Delta r, n+\Delta c) = j \\ 0 & otherwise \end{cases} \tag{6-4}$$

Therefore, the element located in row r and column c of the GLCM refers to the number of the pairs (r,c) appearing in the intensity matrix.

A single image I has multiple GLCMs by different ways of selecting the spatial distance $(\Delta r,\Delta c)$. Equivalently, $(\Delta r,\Delta c)$ also can be represented as (θ,d), where θ is the angle of direction and d is the distance. For example, $(\Delta r,\Delta c) = (1,0)$ is equal to $(\theta,d) = (\frac{\pi}{2},1)$. In order to achieve rotationally invariant feature extraction, $\theta = (0,\frac{\pi}{4},\frac{\pi}{2},\frac{3\pi}{4})$ with a constant d will be calculated as a group in this work due to the relationship $G(i,j|\theta,d) = G^T(i,j|\theta+\pi,d)$, where G^T is the transpose of G. Figure 6-12 shows an example of how a GLCM was created. For a given 8-level grayscale image with dimension 5 by 5, set $(\Delta r,\Delta c) = (0,1)$ and then the corresponding GLCM

is an 8 by 8 matrix. Just for convenience, let us denote these obtained four GLCMs as $G(d) = \{G_1, G_2, G_3, G_4\}$, where d is the selected constant to calculate GLCM.

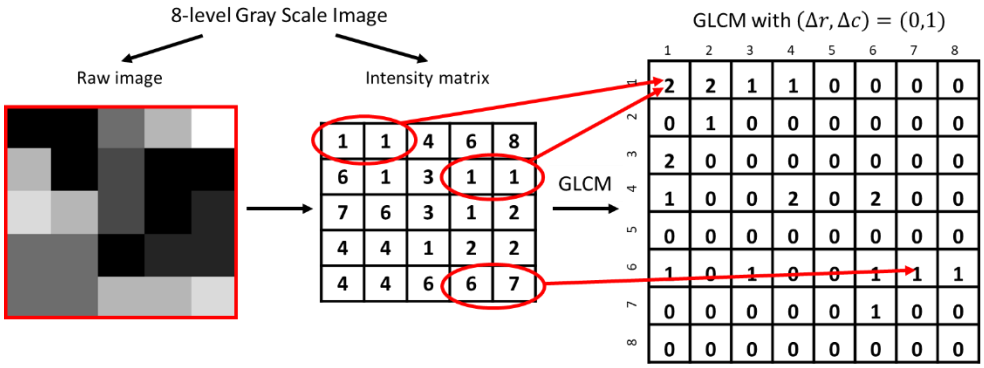

Figure 6-12: Procedure of the GLCM transformation.

6.3.3.2 Feature extraction and online classification implementation

As mentioned in Section 6.3.3.1, the GLCMs of an image $G(d)$, i.e., the textural representation, is still high dimensional. Therefore, it is necessary to extract the most effective features from $G(d)$, i.e., the features that maximize the variation between different defects. To achieve that, some effective statistical features are generated based on the GLCM and utilized to perform classification analysis. From a specific GLCM, a variety of statistics with textural interpretation can be obtained [140, 141], and the following features are used in this work.

- Contrast: Quantify the intensity contrast between the pixel and the neighbor. Obviously, contrast is zero for a constant image.

$$Contrast = \sum_{i,j} (i-j) G(i,j) \tag{6-5}$$

- Correlation: Measurement of the correlation between a pixel and its neighbor. The range of correlation is $[-1,1]$, and the boundary can be achieved only when the image is perfectly correlated. In particular, the correlation measurement is meaningless for a constant image.

$$Correlation = \sum_{i,j} \frac{(i-\mu_i)(j-\mu_j)G(i,j)}{\sigma_i \sigma_j} \tag{6-6}$$

- Energy: Energy is calculated by the sum of squares from the GLCM, which is also known as the angular second moment (ASM). The range of energy is $[0,1]$, and the value is equal to 1 for a constant image.

$$Energy = \sum_{i,j} G(i,j)^2 \tag{6-7}$$

- Homogeneity: The measurement for the closeness of the distribution of elements to the diagonal of GLCM, and its range is also $[0,1]$. When the GLCM is diagonal, the value of homogeneity can achieve 1.

$$Homogeneity = \sum_{i,j} \frac{G(i,j)}{1+|i-j|} \tag{6-8}$$

Based on the above four features, classification algorithms can then be applied to detect the defects by using the labeled training image data (see Section 6.3.2 for details). Through classification performance comparison via cross-validation, the best classification algorithm can be selected (k-NN is used for this study based on the preliminary comparison, see Section 6.4.1). The classifier is trained offline and then applied to the image data collected online. The detailed procedure to perform the proposed TA-ID algorithm are presented in Figure 6-13.

Algorithm 6-1: TA-ID Algorithm

Input data: Image training set with a label (i.e., defective status), online collected images

Input parameters: Constant d for GLCM, a region of ROI

Output: The predicted defective status of the online collected images

Step 0 Image cropping (for ROI) and grayscale transformation (preprocessing)

Step 1 Calculate the GLCMs $G(d)$ for the images in the training set

Step 2 Obtain the textural features based on Eqs. (6-5) to (6-8).

Step 3 Train the standard classifier by using the extracted features

Step 4 Select the best classification algorithm for online application via cross-validation

Step 5 Perform the same feature extraction process for the online collected images

Step 6 Predict the defective status via the trained classifier

Figure 6-13: The detailed procedure to implement the proposed TA-ID algorithm.

6.3.4 Automatic action determination for defect mitigation

As presented in Section 6.3.3, the proposed TA-ID algorithm can identify the types and severity of the defects which occur, and the results can be represented by the indicator variables, $I_1(t)$ and $I_2(t)$, and severity function, $s(t)$, respectively, as introduced in Section 6.3.2. Based on this outcome, this section implements a method for defect mitigation through online parameter adjustment.

The proposed method is based on the proportional-integral-derivative (PID) control technique, which provides simple but effective solutions to many industrial control systems [142, 143]. The basic principle of the PID control is to continuously update the control variable, $u(t)$, i.e., the adjustable machine parameters, based on the proportional, integral and derivative of the error term $e(t)$ estimated from the online measurement. The error term $e(t)$, is defined as the difference between the desired and the actual measurements. In this study, at time t, $e(t)$ is updated by the

defect severity estimation function $s(t)$ based on classification. Mathematically, the framework of PID control can be represented in the time domain as follows [142],

$$u(t) = K_p e(t) + K_i \int_0^t e(\tau)d\tau + K_d \frac{de(t)}{dt} \tag{6-9}$$

where K_p, K_i and K_d are the tuning parameters corresponding to the proportional, integral gain, and derivative terms. For a discrete-time system, e.g., the control problem in this work, the integral and derivative terms will be replaced by summation and difference, respectively.

Although PID control is a well-investigated technique, it is challenging to apply it to this study directly. There are three main reasons: (1) PID control assumes the desired setting (e.g., targeted value for a physical variable) is given, but the optimal parameters in this study are unknown since they will change during the process (see Sec.1); (2) in this research, the measured signals (i.e., image diagnosis results) and adjusted parameters are different variables, which cannot be handled by PID control directly; and (3) the existing PID equation is only valid when $u(t)$ is a continuous variable without any constraints, however, the adjustment of machine parameters in additive manufacturing is usually discrete, that is, they cannot be adjusted continuously.

In the proposed method, the error term $e(t)$ is represented by the defect severity $s(t)$ that is estimated by classification analysis, i.e., $e(t) = s(t)$. Therefore, the first challenge has been addressed. Subsequently, the physical units of image classification and adjustable parameters are connected by the defect type and root cause diagnosis, i.e., indicator variables $I_1(t)$ and $I_2(t)$. Based on the combination of indicator variables, the parameter that needs to be adjusted can be identified. For example, $I_1(t)I_2(t)$ can be used as the indicator function for the adjustment of the cooling system. Then, for the constraints of the adjustable machine parameters, the adjustment

cannot be purely continuous. Based on the description in Section 6.3.2, the proposed control system consists of two adjustable machine parameters, namely, on/off control of the cooling fan (C) (to adjust extruder temperature) and the adjustment of material flow rate (R). C is a binary variable which indicates the action to turn on or off the cooling fan, whereas R is a discrete variable to represent the adjustment value of flow rate and the minimal unit to adjust is 5%. Therefore, based on Eq. (6-9), the output of the PID control equation usually cannot satisfy these discrete constraints. To address this challenge, the proposed strategy introduces the link functions to build the relationship between the PID output (i.e., $u(t)$) and the control variables (i.e., the adjustable machine parameters). First, in terms of the cooling fan on/off control, due to its binary property, the logistic link function, $L(x) = \frac{1}{1+e^{-x}}$ is integrated to the control equation. Then, the equation for cooling fan adjustment can be written as,

$$C(t) = \frac{I_1(t)I_2(t)}{1 + \exp\{-\left[K_p e(t) + K_i \int_0^t e(\tau)d\tau + K_d \frac{de(t)}{dt}\right]\}} \tag{6-10}$$

Similarly, due to the discrete property of material flow rate R, an exponential link function is introduced, which is inspired by the Poisson regression model [144]. With an indicator function $\big(1 - I_2(t)\big)I_1(t)$, the equation for flow rate adjustment can be expressed by,

$$R(t) = (1 - I_2(t))I_1(t) \cdot \exp\{K_p e(t) + K_i \int_0^t e(\tau)d\tau + K_d \frac{de(t)}{dt}\} \tag{6-11}$$

Therefore, consider R and C together, and then the overall framework of the improved closed-loop control system can be illustrated as Figure 6-14.

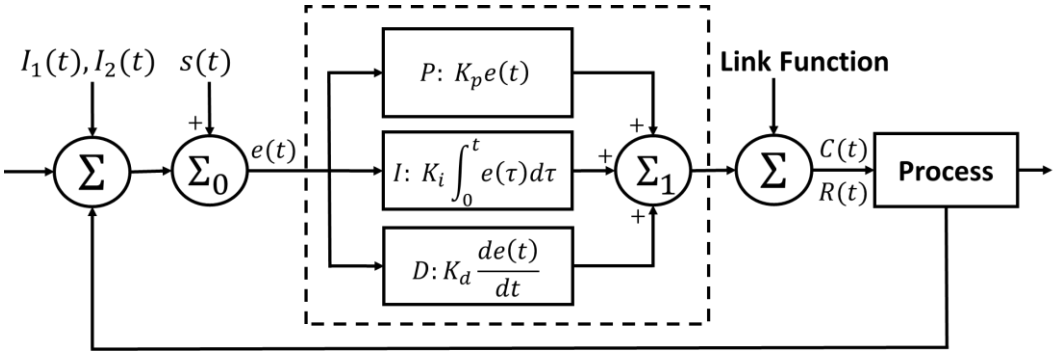

Figure 6-14: The improved closed-control system.

Moreover, for the PID part in the designed controller, usually not all of the three components will be utilized. As concluded in the experimental studies, first, a small steady-state error is allowed. For instance, the surface quality is also good enough in the case of a slightly low material flow rate. In addition, since there is a delay between the changes of some parameters and machine response, the controller should have a fast rise time but a small overshoot. Therefore, the proportional and derivative components are selected for the controller without including the integral part. In practice, tuning parameter estimation is another significant and challenging problem. From the literature, there are some well-developed tuning methods which are effective for some specific cases, such as the Ziegler-Nichols method, Tyreus-Luyben method, and Cohen-Coon method, etc. [145]. Since this work does not have to consider complex control loops in the system, and the investigated defects can be simulated by different parameter settings, the tuning parameters can be trained by offline experiments prior to online application.

In summary, since the online adjustment is not continuous in practice and only PD terms are selected in this study, Eq. (6-9) needs to be discretized as,

$$\tilde{u}(t_k) = \tilde{u}(t_{k-1}) + K_p[\tilde{e}(t_k) - \tilde{e}(t_{k-1})] + K_d\,[\tilde{e}(t_k) - 2\tilde{e}(t_{k-1}) + \tilde{e}(t_{k-2})]/(t_k - t_{k-1}) \tag{6-12}$$

and the discretized version of the developed control mechanism can be reformatted as,

$$C(t_k) = \frac{I_1(t_k)I_2(t_k)}{1 + \exp\{-\tilde{u}(t_k)\}} \tag{6-13}$$

$$R(t_k) = (1 - I_2(t_k))I_1(t_k) \cdot \exp\{\tilde{u}(t_k)\} \tag{6-14}$$

where the discretized error term $\tilde{e}(t_k)$ is defined by the estimated severity of the defects, i.e., the over-fill/under-fill rate diagnosed by online classification. Therefore, the error term $e(t)$ is able to be updated in an online manner.

6.4 Case Studies

Based on the implemented image-based closed-loop quality control system, multiple case studies are performed in this section. The effectiveness of defect detection (Section 6.4.1) and automatic machine parameter adjustment (Section 6.4.2) are validated.

6.4.1 Image-based classification for defect recognition

This case study validates the performance of the developed defect recognition method named the TA-ID algorithm based on the image data captured by the image acquisition system introduced in Section 6.2. A total of 656 sample images with different surface printing quality (i.e., normal or with various defects) were collected. 75% (i.e., 492 images) of them were selected as the training set and the others as the testing set. The defects with different severities were purposely generated by changing the machine parameter settings based on the results of experimental studies (Section 6.3.2).

To implement the developed classification framework proposed in Section 6.3.3, the ROI of the collected images are first converted to grayscale images. Based on the experiments, the 10-level grayscale is the most effective option to represent the textural information of defects, i.e., the range of the pixel intensity is (1-10), and subsequently, the dimension of the GLCM is 10 by 10. To

further extract the most important textural information, the four statistics (see Section 6.3.3.2) of GLCM were obtained as the features for classification analysis to identify the defects. In classification, k-Nearest Neighbor (k-NN) [112] is selected to perform classification analysis based on preliminary performance comparison with other popular classification algorithms, and thus detect the defects of under-fill and over-fill.

For comparison of the performance, four widely used classification algorithms (directly applied to the image set after preprocessing without textural feature extraction) were selected as benchmarks. The criterion to evaluate overall classification performance in this chapter is the F-score, which is a combination of precision and recall [114]. Precision and recall are directly related to Type I and Type II errors, respectively. Eq. (6-15) indicates the calculation method of the F-score. In this work, for one specific type of defect, precision represents the percentage of real defects among all the predicted defects, and recall indicates the percentage of correctly predicted defects among all the real defects. Since multiple defects are investigated, the averaged F-score is used to evaluate one classification method.

$$\mathrm{F-score} = 2 \times \frac{\mathrm{Precision} \times \mathrm{Sensitivity}}{\mathrm{Precision} + \mathrm{Sensitivity}} \tag{6-15}$$

The average F-scores along with the average results of accuracy, precision and recall for the proposed approach and the selected benchmark methods using the testing image set are summarized in Table 6-6, from which it is evident that the proposed method has the best performance in classification, i.e., diagnosing the defects. The CPU of the computer used in the experiments is an Intel® Xeon® Processor E3-1220 v3 (Quad Core, 3.10GHz Turbo, 8MB). The average computational time for classification of a single observation is 0.0029 seconds (equivalent to 345 Hz) for the proposed TA-ID algorithm. It can be seen from Table 6-6 that although it is not

as fast as other benchmark methods, it is sufficient for online defect diagnosis of FFF processes since the computational speed (about 345 Hz) is much faster than the sampling rate for the images (1 Hz) during the printing process.

Table 6-6: Performance comparison between the proposed method and benchmark algorithms (for detection for the defects of under-fill caused by flow rate and cooling system, and over-fill)

Method	Accuracy	Precision	Recall	F-score	Computation time (s)
k-NN	0.61	0.98	0.35	0.52	0.0024
NBC	0.83	0.81	0.83	0.82	0.0036
LDA	0.77	0.66	0.81	0.73	0.0032
SVM	0.82	0.69	0.87	0.77	0.0058
TA-ID (proposed)	**0.85**	**0.81**	**0.89**	**0.85**	**0.0029**

Although the classification analysis was conducted for each individual data point (an image), the decision to trigger machine parameter adjustment was based on a window-based approach (with no overlap). In this case study, a window size of five is used, namely, the classification analysis were accomplished for five consecutive images, and the classification result with the most votes is used for defect identification and the subsequent closed-loop quality control analysis. Since the image sampling frequency of the system is 1 Hz, the action of the adjustable machine parameters will be updated once per five seconds through the closed-loop control system.

6.4.2 Validation of the closed-loop control for defect mitigation

To verify the performance of the closed-loop control system for automatic machine parameter adjustment, two case studies for mitigation of flow rate caused defects and cooling system caused defects are performed.

6.4.2.1 Mitigation of flow-rate-caused defects through closed-loop quality control

The flow rate caused defects commonly occurred in the FFF process. In practice, due to the complexity of geometric design and limitation of slicing algorithms, the desired flow rate and actual setting may not be consistent during printing, which may result in under-fill or over-fill. The optimal setting for flow rate is set at 100% based on the experiments. A defect (i.e., 50% under-fill) is generated with a flow rate of 50%. For the application of the developed control system, the severity estimation is the error term $e(t_k)$ and the adjustment value of the material flow rate refers to $R(t_k)$ in Eq. (6-14). In addition, the values of I_1 and I_2 determine the type of defects.

The detailed testing procedure includes three steps. In the first step three normal layers were printed; in the second step the corresponding machine parameters were changed to generate defects, i.e., set the flow rate as 50% to generate the under-fill defect; and then in the third step the developed closed-loop quality control system is activated to detect and then mitigate the defects by implementing image-based classification and automatic machine parameter adjustment.

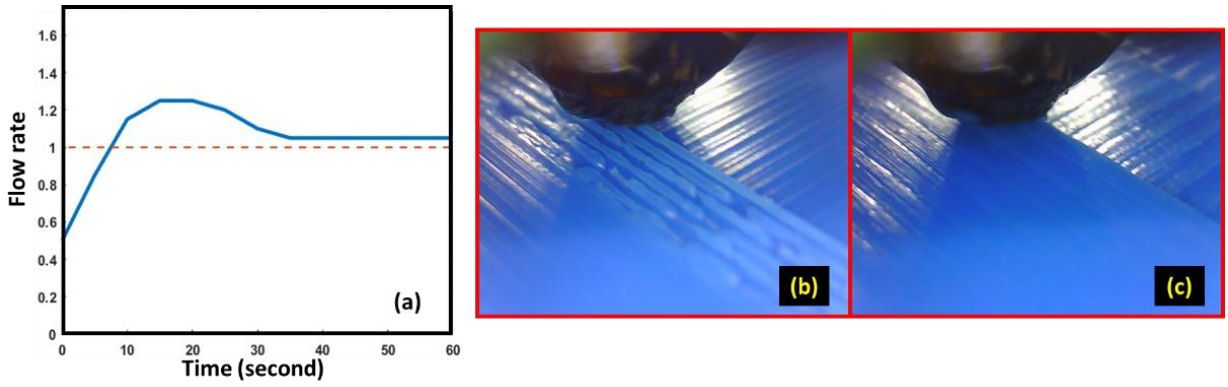

Figure 6-15: The performance of the designed control system when defects occur due to low flow rate. (a) Controller performance; (b) initial surface (under-fill defects appear) (c) surface after closed-loop control adjustment (back to normal printing).

The results show that the control system identifies the defects successfully ($I_2 = 0$) and the surface quality appears to return to normal after an additional 30-40 seconds of printing based on the

adjustment of flow rate (see Figure 6-15). Considering the delay of machine reaction (Table 6-1), the control system only takes about half a minute to correct the printing quality. The performance of the controller is acceptable and promising. In addition, although steady-state error exists due to resolution (5%) of flow rate adjustment, the layer surface after adjustment is the same as the normal condition.

6.4.2.2 Mitigation of flow-rate-caused defects through closed-loop quality control

The verification for mitigation of the cooling system-caused defects is performed in this section. The occurrence of the cooling system-caused defects is due to the low temperature causing the filament to not be fully melted and extruded. Therefore, turning the cooling fan on/off is a very important way to mitigate defects. It can also be seen from the experimental study that choosing an inappropriate setting for the cooling fan will cause major defects. In this study, the optimal temperature target is 230°C, and the real-time temperature of the nozzle is measured by the built-in thermal sensor as verification.

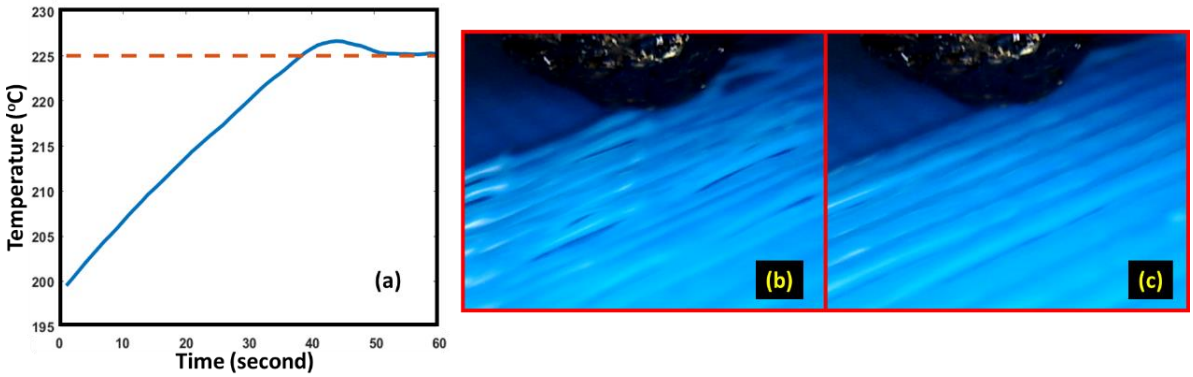

Figure 6-16: The performance of the designed control system when defects occur due to cooling system. (a) The change of temperature when the control system starts running; (b) initial surface (under-fill defects appear); (c) surface after closed-loop control adjustment (back to normal printing).

The testing procedure is similar to the flow rate case (Section 6.4.2.1). After three layers of normal printing in the first step, the second step is to turn on the cooling fan to reduce the nozzle temperature T (lower than 205^{o}C), followed by running the developed closed-loop control system in the third step. The results indicated that the system correctly identified the type of defects ($I_2 = 1$) and the temperature comes back to the optimal target (230^{o}C) with an improved printing quality in a short time after turning off the cooling fan (see Figure 6-16). To quantify the process variability, a total of five trials were performed and the results were almost the same. The control system can always turn off the cooling fan within 15 seconds once defects appear and the surface quality will come back to normal status within 45 seconds of turning off the fan. The timely adjustment also saves the process since the cooling system-caused defects can result in clogging if the defects are not mitigated in time.

6.5 Conclusions

This chapter developed image-based online defect recognition with a closed-loop feedback quality control system for defect mitigation in AM with FFF. For defect recognition, an effective feature extraction method using image textural analysis was proposed to extract the appropriate textural features of defects from the input images. The extracted features were very effective for classification analysis-based defect detection. In the case studies, the resulting F-scores showed that the proposed method has the best performance for image classification compared with the benchmark methods. To implement online defect mitigation, a PID-based feedback closed-loop quality control system was developed. The case studies showed that the proposed control framework is very effective for combating the defects in the FFF process by adjusting the related machine parameters automatically. This chapter is a preliminary work for online closed-loop

quality control system development in the AM process, and the results demonstrate that this research direction is quite promising for significant improvement of the quality of AM parts.

The future work is mainly in three directions. First, since the current online monitoring device only has two microscopes, the coverage may be improved, as blind spots could still exist which may affect the diagnosis results. Embedding new image-based sensing devices, such as a thermographic camera, may also improve the system performance. Second, more types of defects can be investigated. As additional types of defects are considered, further experimental studies are required as a more comprehensive relationship model between defects and machine parameters is created. Third, for the currently designed closed-loop quality control system, the PID framework-based controller still has some limitations. For example, the optimal tuning parameter settings may vary at different layers if the part is complex, or the relationship between defects and machine parameters may not be very clear when considering more types of defects. Also, the response time may still be reduced. Therefore, a further goal of the future work is to introduce some strategies from fuzzy control theory [146], reinforcement learning [147], and transfer learning [148] to overcome the limitations of the current control system.

7 Conclusions and future work

This dissertation aims to build a basis for smart additive manufacturing in terms of the capability for online intelligent quality assurance. Several new methodologies are developed to achieve this goal. This chapter summarizes the contributions and conclusions of this dissertation research, as well as provides a brief discussion of the future work directions.

7.1 Research contributions and conclusions

The major contribution of this research is to create several data-driven methodologies for online quality monitoring and control of AM processes. The proposed methods successfully overcome some typical challenges in online quality assurance of AM processes. Specific contributions and conclusions are summarized as three categories (Figure 7-1):

(1) **Feature extraction:** Two effective feature extraction approaches are proposed based on spectral graph theory (Chapter 3) and nonlinear dimension reduction (Chapter 4). These two methods are successfully tested using both simulation and actual data sets. The dimension reduction-based method is able to extract the critical quality information from high dimensional sensor signals. The spectral graph theory-based approach demonstrates the great potential for cyber-physical attack detection in AM.

(2) **Process modeling:** A unique physical phenomenon called reheating in AM is investigated, with the development of a new bilateral time series modeling approach. This developed model is capable of incorporating the impact from reheating effects. Therefore, this method is able to provide high accuracy forecasting for the layer-wise quality characteristics.

(3) **Defect detection and mitigation:** An image analysis and PID control theory-based online defect detection and mitigation approach is implemented. With this approach, the AM platform has initial capability to automatically adjust machine parameters without human operation, which makes the AM process more intelligent to treat the quality issues.

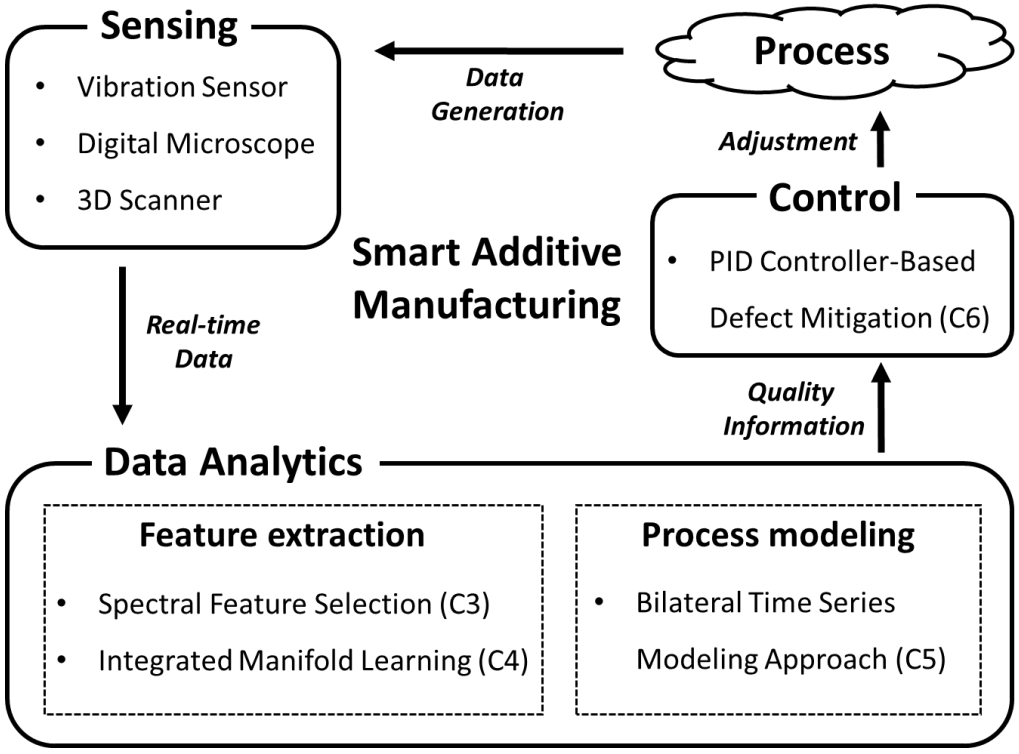

Figure 7-1: The proposed methods to build a basis for smart additive manufacturing.

7.2 Directions of future work

Based on the promising demonstration from case studies, future work and investigation along these lines is highly valuable to pursue. Overall, based on the major components of smart manufacturing, the direction of future work has three main aspects:

(1) **Sensing:** More types of sensors should be explored for data acquisition purposes, which are helpful to reduce the information loss. Meanwhile, with new sensors, how to design appropriate sensing systems is essential as well.

(2) **Analytics:** To handle the massive amount of real-time sensor data, more big data analytics methodologies are valuable to be investigated, such as efficient deep learning and robust representation learning algorithms, etc.

(3) **Control:** Further increase the intelligence of the closed-loop quality control framework. More artificial intelligence (AI) related methods could be integrated with the current system. For example, using a reinforcement learning-based approach to improve the quality control capability when new defects or other quality issues occur.

In addition, all the developed methods in this dissertation are also very promising to be extended to other manufacturing systems, or even other application areas such as healthcare systems, so long as the process has a similar mechanism or the collected sensor data have similar formats. This research aims to resolve the problems regarding the quality monitoring, forecasting, and control, which are also very critical for many other real-world cases.

References

[1] *Standard terminology for additive manufacturing technologies*, 2012.

[2] C. Beyer, "Strategic implications of current trends in additive manufacturing," *Journal of Manufacturing Science and Engineering,* vol. 136, no. 6, p. 064701, 2014.

[3] N. Guo and M. C. Leu, "Additive manufacturing: technology, applications and research needs," *Frontiers of Mechanical Engineering,* vol. 8, no. 3, pp. 215-243, 2013.

[4] F. P. Melchels, M. A. Domingos, T. J. Klein, J. Malda, P. J. Bartolo, and D. W. Hutmacher, "Additive manufacturing of tissues and organs," *Progress in Polymer Science,* vol. 37, no. 8, pp. 1079-1104, 2012.

[5] T. J. Horn and O. L. Harrysson, "Overview of current additive manufacturing technologies and selected applications," *Science progress,* vol. 95, no. 3, pp. 255-282, 2012.

[6] I. Gibson, D. W. Rosen, and B. Stucker, *Additive manufacturing technologies*. Springer, 2014.

[7] W. Gao, Y. Zhang, D. Ramanujan, K. Ramani, Y. Chen, C. B. Williams, C. C. Wang, Y. C. Shin, S. Zhang, and P. D. Zavattieri, "The status, challenges, and future of additive manufacturing in engineering," *Computer-Aided Design,* vol. 69, pp. 65-89, 2015.

[8] O. Ivanova, C. Williams, and T. Campbell, "Additive manufacturing (AM) and nanotechnology: promises and challenges," *Rapid Prototyping Journal,* vol. 19, no. 5, pp. 353-364, 2013.

[9] E. Savio, L. De Chiffre, and R. Schmitt, "Metrology of freeform shaped parts," *CIRP annals,* vol. 56, no. 2, pp. 810-835, 2007.

[10] G. Henzold, *Geometrical dimensioning and tolerancing for design, manufacturing and inspection: a handbook for geometrical product specification using ISO and ASME standards*. Elsevier, 2006.

[11] A. H. Peng and Z. M. Wang, "Researches into influence of process parameters on FDM parts precision," in *Applied Mechanics and Materials*, 2010, vol. 34, pp. 338-343: Trans Tech Publ.

[12] G. Tapia and A. Elwany, "A review on process monitoring and control in metal-based additive manufacturing," *Journal of Manufacturing Science and Engineering,* vol. 136, no. 6, p. 060801, 2014.

[13] H. Wu, Y. Wang, and Z. Yu, "In situ monitoring of FDM machine condition via acoustic emission," *The International Journal of Advanced Manufacturing Technology,* vol. 84, no. 5-8, pp. 1483-1495, 2016.

[14] C. Kousiatza and D. Karalekas, "In-situ monitoring of strain and temperature distributions during fused deposition modeling process," *Materials & Design,* vol. 97, pp. 400-406, 2016.

[15] P. K. Rao, J. P. Liu, D. Roberson, Z. J. Kong, and C. Williams, "Online real-time quality monitoring in additive manufacturing processes using heterogeneous sensors," *Journal of Manufacturing Science and Engineering*, vol. 137, no. 6, p. 061007, 2015.

[16] A. Dunbar, E. Denlinger, J. Heigel, P. Michaleris, P. Guerrier, R. Martukanitz, and T. W. Simpson, "Development of experimental method for in situ distortion and temperature measurements during the laser powder bed fusion additive manufacturing process," *Additive Manufacturing*, vol. 12, pp. 25-30, 2016.

[17] M. Khanzadeh, S. Chowdhury, M. A. Tschopp, H. R. Doude, M. Marufuzzaman, and L. Bian, "In-situ monitoring of melt pool images for porosity prediction in directed energy deposition processes," *IISE Transactions*, vol. 51, no. 5, pp. 437-455, 2019.

[18] M. Mahmoudi, A. A. Ezzat, and A. Elwany, "Layerwise Anomaly Detection in Laser Powder-Bed Fusion Metal Additive Manufacturing," *Journal of Manufacturing Science and Engineering*, vol. 141, no. 3, p. 031002, 2019.

[19] J. Schwerdtfeger, R. F. Singer, and C. Körner, "In situ flaw detection by IR-imaging during electron beam melting," *Rapid Prototyping Journal*, vol. 18, no. 4, pp. 259-263, 2012.

[20] M. Grasso, A. Demir, B. Previtali, and B. Colosimo, "In situ monitoring of selective laser melting of zinc powder via infrared imaging of the process plume," *Robotics and Computer-Integrated Manufacturing*, vol. 49, pp. 229-239, 2018.

[21] T. Fang, I. Bakhadyrov, M. A. Jafari, and G. Alpan, "Online detection of defects in layered manufacturing," in *Proceedings. 1998 IEEE International Conference on Robotics and Automation (Cat. No. 98CH36146)*, 1998, vol. 1, pp. 254-259: IEEE.

[22] T. Fang, M. A. Jafari, S. C. Danforth, and A. Safari, "Signature analysis and defect detection in layered manufacturing of ceramic sensors and actuators," *Machine Vision and Applications*, vol. 15, no. 2, pp. 63-75, 2003.

[23] Y. Cheng and M. A. Jafari, "Vision-based online process control in manufacturing applications," *IEEE Transactions on Automation Science and Engineering*, vol. 5, no. 1, pp. 140-153, 2008.

[24] T. Craeghs, S. Clijsters, J.-P. Kruth, F. Bechmann, and M.-C. Ebert, "Detection of process failures in layerwise laser melting with optical process monitoring," *Physics Procedia*, vol. 39, pp. 753-759, 2012.

[25] J. A. Kanko, A. P. Sibley, and J. M. Fraser, "In situ morphology-based defect detection of selective laser melting through inline coherent imaging," *Journal of Materials Processing Technology*, vol. 231, pp. 488-500, 2016.

[26] M. Grasso, V. Laguzza, Q. Semeraro, and B. M. Colosimo, "In-process monitoring of selective laser melting: spatial detection of defects via image data analysis," *Journal of Manufacturing Science and Engineering*, vol. 139, no. 5, p. 051001, 2017.

[27] B. Zhang, J. Ziegert, F. Farahi, and A. Davies, "In situ surface topography of laser powder bed fusion using fringe projection," *Additive Manufacturing*, vol. 12, pp. 100-107, 2016.

[28] K. Bastani, P. K. Rao, and Z. J. Kong, "An online sparse estimation-based classification approach for real-time monitoring in advanced manufacturing processes from heterogeneous sensor data," *IIE Transactions*, vol. 48, no. 7, pp. 579-598, 2016.

[29] M. Khanzadeh, W. Tian, A. Yadollahi, H. R. Doude, M. A. Tschopp, and L. Bian, "Dual process monitoring of metal-based additive manufacturing using tensor decomposition of thermal image streams," *Additive Manufacturing,* vol. 23, pp. 443-456, 2018.

[30] B. Yao, F. Imani, A. S. Sakpal, E. W. Reutzel, and H. Yang, "Multifractal analysis of image profiles for the characterization and detection of defects in additive manufacturing," *Journal of Manufacturing Science and Engineering,* vol. 140, no. 3, p. 031014, 2018.

[31] A. C. C. Law, N. Southon, N. Senin, P. Stavroulakis, R. Leach, R. Goodridge, Z. J. Kong, and M. M. Team, "Curvature-based Segmentation of Powder Bed Point Clouds for in-Process Monitoring," 2018: Proceedings of the 29th Annual International Solid Freeform Fabrication Symposium.

[32] H. Sun, P. K. Rao, Z. J. Kong, X. Deng, and R. Jin, "Functional quantitative and qualitative models for quality modeling in a fused deposition modeling process," *IEEE Transactions on Automation Science and Engineering,* vol. 15, no. 1, pp. 393-403, 2017.

[33] J. Liu, C. Liu, Y. Bai, P. Rao, C. B. Williams, and Z. J. Kong, "Layer-wise spatial modeling of porosity in additive manufacturing," *IISE Transactions,* vol. 51, no. 2, pp. 109-123, 2019.

[34] C. Cheng, A. Sa-Ngasoongsong, O. Beyca, T. Le, H. Yang, Z. J. Kong, and S. T. Bukkapatnam, "Time series forecasting for nonlinear and non-stationary processes: a review and comparative study," *IIE Transactions,* vol. 47, no. 10, pp. 1053-1071, 2015.

[35] R. Yao and S. N. Pakzad, "Autoregressive statistical pattern recognition algorithms for damage detection in civil structures," *Mechanical Systems and Signal Processing,* vol. 31, pp. 355-368, 2012.

[36] Y. Lu and F. Gao, "A novel time-domain auto-regressive model for structural damage diagnosis," *Journal of Sound and Vibration,* vol. 283, no. 3-5, pp. 1031-1049, 2005.

[37] W. Jiang, K.-L. Tsui, and W. H. Woodall, "A new SPC monitoring method: The ARMA chart," *Technometrics,* vol. 42, no. 4, pp. 399-410, 2000.

[38] S. Vander Wiel, "Monitoring processes that wander using integrated moving average models," *Technometrics,* vol. 38, no. 2, pp. 139-151, 1996.

[39] J. E. Jarrett and X. Pan, "The quality control chart for monitoring multivariate autocorrelated processes," *Computational Statistics & Data Analysis,* vol. 51, no. 8, pp. 3862-3870, 2007.

[40] J. K. Ord, A. B. Koehler, R. D. Snyder, and R. J. Hyndman, "Monitoring processes with changing variances," *International Journal of Forecasting,* vol. 25, no. 3, pp. 518-525, 2009.

[41] T.-M. Wang, J.-T. Xi, and Y. Jin, "A model research for prototype warp deformation in the FDM process," *The International Journal of Advanced Manufacturing Technology,* vol. 33, no. 11-12, pp. 1087-1096, 2007.

[42] R. Anitha, S. Arunachalam, and P. Radhakrishnan, "Critical parameters influencing the quality of prototypes in fused deposition modelling," *Journal of Materials Processing Technology,* vol. 118, no. 1-3, pp. 385-388, 2001.

[43] M. K. Agarwala, V. R. Jamalabad, N. A. Langrana, A. Safari, P. J. Whalen, and S. C. Danforth, "Structural quality of parts processed by fused deposition," *Rapid prototyping journal,* vol. 2, no. 4, pp. 4-19, 1996.

[44] A. Armillotta, "Assessment of surface quality on textured FDM prototypes," *Rapid Prototyping Journal,* vol. 12, no. 1, pp. 35-41, 2006.

[45] E. Pei, R. Ian Campbell, and D. de Beer, "Entry-level RP machines: how well can they cope with geometric complexity?," *Assembly Automation,* vol. 31, no. 2, pp. 153-160, 2011.

[46] D. Qiu and N. A. Langrana, "Void eliminating toolpath for extrusion-based multi-material layered manufacturing," *Rapid prototyping journal,* vol. 8, no. 1, pp. 38-45, 2002.

[47] K. Tong, S. Joshi, and E. Amine Lehtihet, "Error compensation for fused deposition modeling (FDM) machine by correcting slice files," *Rapid Prototyping Journal,* vol. 14, no. 1, pp. 4-14, 2008.

[48] F. Lin, W. Sun, and Y. Yan, "Optimization with minimum process error for layered manufacturing fabrication," *Rapid Prototyping Journal,* vol. 7, no. 2, pp. 73-82, 2001.

[49] F. Xu, H. Loh, and Y. Wong, "Considerations and selection of optimal orientation for different rapid prototyping systems," *Rapid Prototyping Journal,* vol. 5, no. 2, pp. 54-60, 1999.

[50] E. Sabourin, S. A. Houser, and J. Helge Bøhn, "Accurate exterior, fast interior layered manufacturing," *Rapid Prototyping Journal,* vol. 3, no. 2, pp. 44-52, 1997.

[51] C. Ziemian and P. Crawn III, "Computer aided decision support for fused deposition modeling," *Rapid Prototyping Journal,* vol. 7, no. 3, pp. 138-147, 2001.

[52] A. Peng and X. Xiao, "Investigation on reasons inducing error and measures improving accuracy in fused deposition modeling," *Advances in Information Sciences and Service Sciences,* vol. 4, no. 5, 2012.

[53] L. K. Gillespie, *Design for Advanced Manufacturing: Technologies, and Processes*. McGraw Hill Professional, 2017.

[54] S. F. Krar and A. Gill, *Exploring advanced manufacturing technologies*. Industrial Press Inc., 2003.

[55] T. D. Ngo, A. Kashani, G. Imbalzano, K. T. Nguyen, and D. Hui, "Additive manufacturing (3D printing): A review of materials, methods, applications and challenges," *Composites Part B: Engineering,* vol. 143, pp. 172-196, 2018.

[56] W. H. Woodall, "Controversies and contradictions in statistical process control," *Journal of Quality Technology,* vol. 32, no. 4, pp. 341-350, 2000.

[57] J. P. Liu, O. F. Beyca, P. K. Rao, Z. J. Kong, and S. T. Bukkapatnam, "Dirichlet process Gaussian mixture models for real-time monitoring and their application to chemical mechanical planarization," *IEEE Transactions on Automation Science and Engineering,* vol. 14, no. 1, pp. 208-221, 2016.

[58] W. Huang, J. Liu, V. Chalivendra, D. Ceglarek, Z. J. Kong, and Y. Zhou, "Statistical modal analysis for variation characterization and application in manufacturing quality control," *IIE Transactions*, vol. 46, no. 5, pp. 497-511, 2014.

[59] M. Colledani and T. Tolio, "Impact of quality control on production system performance," *CIRP annals*, vol. 55, no. 1, pp. 453-456, 2006.

[60] W. H. Woodall, "The use of control charts in health-care and public-health surveillance," *Journal of Quality Technology*, vol. 38, no. 2, pp. 89-104, 2006.

[61] M. J. Anderson and A. A. Thompson, "Multivariate control charts for ecological and environmental monitoring," *Ecological Applications*, vol. 14, no. 6, pp. 1921-1935, 2004.

[62] D. C. Montgomery, *Introduction to statistical quality control*. John Wiley & Sons, 2007.

[63] P. Qiu, *Introduction to statistical process control*. Chapman and Hall/CRC, 2013.

[64] J. G. Proakis, *Digital signal processing: principles algorithms and applications*. Pearson Education India, 2001.

[65] S. Chen, B. Ma, and K. Zhang, "On the similarity metric and the distance metric," *Theoretical Computer Science*, vol. 410, no. 24-25, pp. 2365-2376, 2009.

[66] P. K. Rao, O. F. Beyca, Z. J. Kong, S. T. Bukkapatnam, K. E. Case, and R. Komanduri, "A graph-theoretic approach for quantification of surface morphology variation and its application to chemical mechanical planarization process," *IIE Transactions*, vol. 47, no. 10, pp. 1088-1111, 2015.

[67] C. Liu, A. Kapoor, J. VanOsdol, K. Ektate, Z. J. Kong, and A. Ranjan, "A Spectral Fiedler Field-based Contrast Platform for Imaging of Nanoparticles in Colon Tumor," *Scientific reports*, vol. 8, no. 1, p. 11390, 2018.

[68] M. Arjovsky, S. Chintala, and L. Bottou, "Wasserstein generative adversarial networks," in *International Conference on Machine Learning*, 2017, pp. 214-223.

[69] L. Baringhaus and N. Henze, "Cramér–von Mises distance: probabilistic interpretation, confidence intervals, and neighbourhood-of-model validation," *Journal of Nonparametric Statistics*, vol. 29, no. 2, pp. 167-188, 2017.

[70] M. S. Tootooni, C. Liu, D. Roberson, R. Donovan, P. K. Rao, Z. J. Kong, and S. T. Bukkapatnam, "Online non-contact surface finish measurement in machining using graph theory-based image analysis," *Journal of Manufacturing Systems*, vol. 41, pp. 266-276, 2016.

[71] P. K. Rao, Z. J. Kong, C. E. Duty, R. J. Smith, V. Kunc, and L. J. Love, "Assessment of dimensional integrity and spatial defect localization in additive manufacturing using spectral graph theory," *Journal of Manufacturing Science and Engineering*, vol. 138, no. 5, p. 051007, 2016.

[72] F. R. Chung and F. C. Graham, *Spectral graph theory* (no. 92). American Mathematical Soc., 1997.

[73] A. Y. Ng, M. I. Jordan, and Y. Weiss, "On spectral clustering: Analysis and an algorithm," in *Advances in neural information processing systems*, 2002, pp. 849-856.

[74] M. Belkin and P. Niyogi, "Laplacian eigenmaps and spectral techniques for embedding and clustering," in *Advances in neural information processing systems*, 2002, pp. 585-591.

[75] M. Fiedler, "Algebraic connectivity of graphs," *Czechoslovak mathematical journal,* vol. 23, no. 2, pp. 298-305, 1973.

[76] M. S. Tootooni, P. K. Rao, C.-A. Chou, and Z. J. Kong, "A spectral graph theoretic approach for monitoring multivariate time series data from complex dynamical processes," *IEEE Transactions on Automation Science and Engineering,* vol. 15, no. 1, pp. 127-144, 2016.

[77] H. Guo, K. Paynabar, and J. Jin, "Multiscale monitoring of autocorrelated processes using wavelets analysis," *IIE Transactions,* vol. 44, no. 4, pp. 312-326, 2012.

[78] S. Huang, Z. J. Kong, and W. Huang, "High-dimensional process monitoring and change point detection using embedding distributions in reproducing kernel Hilbert space," *IIE Transactions,* vol. 46, no. 10, pp. 999-1016, 2014.

[79] E. Parzen, "Quantile probability and statistical data modeling," *Statistical Science,* vol. 19, no. 4, pp. 652-662, 2004.

[80] D. Ruppert, *Statistics and data analysis for financial engineering*. Springer, 2011.

[81] T. J. Linsmeier and N. D. Pearson, "Value at risk," *Financial Analysts Journal,* vol. 56, no. 2, pp. 47-67, 2000.

[82] W. H. Woodall, "Control charts based on attribute data: bibliography and review," *Journal of quality technology,* vol. 29, no. 2, pp. 172-183, 1997.

[83] K. Gurney, *An introduction to neural networks*. CRC press, 2014.

[84] C.-S. Cheng, "A neural network approach for the analysis of control chart patterns," *International Journal of Production Research,* vol. 35, no. 3, pp. 667-697, 1997.

[85] T. G. Dietterich, "Ensemble methods in machine learning," in *International workshop on multiple classifier systems*, 2000, pp. 1-15: Springer.

[86] O. F. Beyca, P. K. Rao, Z. J. Kong, S. T. Bukkapatnam, and R. Komanduri, "Heterogeneous sensor data fusion approach for real-time monitoring in ultraprecision machining (UPM) process using non-parametric Bayesian clustering and evidence theory," *IEEE Transactions on Automation Science and Engineering,* vol. 13, no. 2, pp. 1033-1044, 2015.

[87] V. Makis, "Multivariate Bayesian control chart," *Operations Research,* vol. 56, no. 2, pp. 487-496, 2008.

[88] L. J. Wells, J. A. Camelio, C. B. Williams, and J. White, "Cyber-physical security challenges in manufacturing systems," *Manufacturing Letters,* vol. 2, no. 2, pp. 74-77, 2014.

[89] A. E. Elhabashy, L. J. Wells, J. A. Camelio, and W. H. Woodall, "A cyber-physical attack taxonomy for production systems: a quality control perspective," *Journal of Intelligent Manufacturing,* pp. 1-16, 2018.

[90] Z. DeSmit, A. E. Elhabashy, L. J. Wells, and J. A. Camelio, "Cyber-physical vulnerability assessment in manufacturing systems," *Procedia Manufacturing,* vol. 5, pp. 1060-1074, 2016.

[91] L. Sturm, C. Williams, J. Camelio, J. White, and R. Parker, "Cyber-physical vunerabilities in additive manufacturing systems," *Context,* vol. 7, no. 2014, p. 8, 2014.

[92] L. D. Sturm, C. B. Williams, J. A. Camelio, J. White, and R. Parker, "Cyber-physical vulnerabilities in additive manufacturing systems: A case study attack on the. STL file with human subjects," *Journal of Manufacturing Systems,* vol. 44, pp. 154-164, 2017.

[93] H. Turner, J. White, J. A. Camelio, C. Williams, B. Amos, and R. Parker, "Bad parts: Are our manufacturing systems at risk of silent cyberattacks?," *IEEE Security & Privacy,* vol. 13, no. 3, pp. 40-47, 2015.

[94] H. Morgan, H. Levatti, J. Sienz, A. Gil, and D. Bould, "GE Jet engine bracket challenge: a case study in sustainable design," *Sustainable Design and Manufacturing,* pp. 95-107, 2014.

[95] S. B. Kotsiantis, I. Zaharakis, and P. Pintelas, "Supervised machine learning: A review of classification techniques," *Emerging artificial intelligence applications in computer engineering,* vol. 160, pp. 3-24, 2007.

[96] T. Lin and H. Zha, "Riemannian manifold learning," *IEEE Transactions on Pattern Analysis and Machine Intelligence,* vol. 30, no. 5, pp. 796-809, 2008.

[97] Y. Ma and Y. Fu, *Manifold learning theory and applications*. CRC press, 2011.

[98] Y. Bengio, A. Courville, and P. Vincent, "Representation learning: A review and new perspectives," *IEEE transactions on pattern analysis and machine intelligence,* vol. 35, no. 8, pp. 1798-1828, 2013.

[99] J. B. Tenenbaum, V. De Silva, and J. C. Langford, "A global geometric framework for nonlinear dimensionality reduction," *science,* vol. 290, no. 5500, pp. 2319-2323, 2000.

[100] S. T. Roweis and L. K. Saul, "Nonlinear dimensionality reduction by locally linear embedding," *science,* vol. 290, no. 5500, pp. 2323-2326, 2000.

[101] K. Thulasiraman and M. N. Swamy, *Graphs: theory and algorithms*. Wiley Online Library, 1992.

[102] M. Balasubramanian and E. L. Schwartz, "The isomap algorithm and topological stability," *Science,* vol. 295, no. 5552, pp. 7-7, 2002.

[103] K. Q. Weinberger, F. Sha, and L. K. Saul, "Learning a kernel matrix for nonlinear dimensionality reduction," in *Proceedings of the twenty-first international conference on Machine learning*, 2004, p. 106: ACM.

[104] B. Schölkopf, A. Smola, and K.-R. Müller, "Kernel principal component analysis," in *International conference on artificial neural networks*, 1997, pp. 583-588: Springer.

[105] B. Schölkopf, "The kernel trick for distances," in *Advances in neural information processing systems*, 2001, pp. 301-307.

[106] S. Vishwanathan, K. M. Borgwardt, O. Guttman, and A. Smola, "Kernel extrapolation," *Neurocomputing,* vol. 69, no. 7-9, pp. 721-729, 2006.

[107] M. Yaghoobi, D. Wu, and M. E. Davies, "Fast non-negative orthogonal matching pursuit," *IEEE Signal Processing Letters,* vol. 22, no. 9, pp. 1229-1233, 2015.

[108] R. Battiti and F. Masulli, "BFGS optimization for faster and automated supervised learning," in *International neural network conference*, 1990, pp. 757-760: Springer.

[109] T. T. Cai and L. Wang, "Orthogonal matching pursuit for sparse signal recovery with noise," 2011: Institute of Electrical and Electronics Engineers.

[110] Y.-H. Dai, "Convergence properties of the BFGS algoritm," *SIAM Journal on Optimization*, vol. 13, no. 3, pp. 693-701, 2002.

[111] T.-J. Chin and D. Suter, "Out-of-sample extrapolation of learned manifolds," *IEEE Transactions on Pattern Analysis and Machine Intelligence*, vol. 30, no. 9, pp. 1547-1556, 2008.

[112] J. Friedman, T. Hastie, and R. Tibshirani, *The elements of statistical learning*. Springer series in statistics New York, 2001.

[113] B. Schölkopf, A. Smola, and K.-R. Müller, "Nonlinear component analysis as a kernel eigenvalue problem," *Neural computation*, vol. 10, no. 5, pp. 1299-1319, 1998.

[114] D. M. Powers, "Evaluation: from precision, recall and F-measure to ROC, informedness, markedness and correlation," 2011.

[115] P. J. Brockwell, R. A. Davis, and M. V. Calder, *Introduction to time series and forecasting*. Springer, 2002.

[116] A. Silvennoinen and T. Teräsvirta, "Multivariate GARCH models," in *Handbook of financial time series*: Springer, 2009, pp. 201-229.

[117] F. Reif, *Fundamentals of statistical and thermal physics*. Waveland Press, 2009.

[118] P. Whittle, "On stationary processes in the plane," *Biometrika*, pp. 434-449, 1954.

[119] G. E. Box, G. M. Jenkins, G. C. Reinsel, and G. M. Ljung, *Time series analysis: forecasting and control*. John Wiley & Sons, 2015.

[120] R. Tibshirani, "Regression shrinkage and selection via the lasso," *Journal of the Royal Statistical Society. Series B (Methodological)*, pp. 267-288, 1996.

[121] S. Boyd and L. Vandenberghe, *Convex optimization*. Cambridge university press, 2004.

[122] S. Arlot and A. Celisse, "A survey of cross-validation procedures for model selection," *Statistics surveys*, vol. 4, pp. 40-79, 2010.

[123] A. Chatterjee and S. N. Lahiri, "Bootstrapping lasso estimators," *Journal of the American Statistical Association*, vol. 106, no. 494, pp. 608-625, 2011.

[124] B. Spencer Jr, M. E. Ruiz‐Sandoval, and N. Kurata, "Smart sensing technology: opportunities and challenges," *Structural Control and Health Monitoring*, vol. 11, no. 4, pp. 349-368, 2004.

[125] A. C. Davison and D. V. Hinkley, *Bootstrap methods and their application*. Cambridge university press, 1997.

[126] (2018). *May Solutions LLC*. Available: http://www.maysolutionsllc.com/index.html

[127] J. Geng, "Structured-light 3D surface imaging: a tutorial," *Advances in Optics and Photonics*, vol. 3, no. 2, pp. 128-160, 2011.

[128] L. Villalpando, H. Eiliat, and R. Urbanic, "An optimization approach for components built by fused deposition modeling with parametric internal structures," *Procedia CIRP*, vol. 17, pp. 800-805, 2014.

[129] M. S. Tootooni, A. Dsouza, R. Donovan, P. K. Rao, Z. J. Kong, and P. Borgesen, "Classifying the Dimensional Variation in Additive Manufactured Parts From Laser-Scanned Three-Dimensional Point Cloud Data Using Machine Learning Approaches," *Journal of Manufacturing Science and Engineering*, vol. 139, no. 9, p. 091005, 2017.

[130] M. Montazeri and P. Rao, "Sensor-Based Build Condition Monitoring in Laser Powder Bed Fusion Additive Manufacturing Process Using a Spectral Graph Theoretic Approach," *Journal of Manufacturing Science and Engineering*, vol. 140, no. 9, p. 091002, 2018.

[131] M. Khanzadeh, S. Chowdhury, M. A. Tschopp, H. R. Doude, M. Marufuzzaman, and L. Bian, "In-situ monitoring of melt pool images for porosity prediction in directed energy deposition processes," *IISE Transactions*, pp. 1-19, 2018.

[132] B. N. Turner, R. Strong, and S. A. Gold, "A review of melt extrusion additive manufacturing processes: I. Process design and modeling," *Rapid Prototyping Journal*, vol. 20, no. 3, pp. 192-204, 2014.

[133] C. J. Wu and M. S. Hamada, *Experiments: planning, analysis, and optimization*. John Wiley & Sons, 2011.

[134] O. A. Mohamed, S. H. Masood, and J. L. Bhowmik, "Optimization of fused deposition modeling process parameters: a review of current research and future prospects," *Advances in Manufacturing*, vol. 3, no. 1, pp. 42-53, 2015.

[135] K. Chin Ang, K. Fai Leong, C. Kai Chua, and M. Chandrasekaran, "Investigation of the mechanical properties and porosity relationships in fused deposition modelling-fabricated porous structures," *Rapid Prototyping Journal*, vol. 12, no. 2, pp. 100-105, 2006.

[136] M. Mirmehdi, X. Xie, and J. S. Suri, *Handbook of Texture Analysis*. World Scientific, 2008.

[137] R. Walker, P. Jackway, and I. Longstaff, "Recent developments in the use of the co-occurrence matrix for texture recognition," in *IEEE 13th International Conference on Digital Signal Processing*, 1997, vol. 1, pp. 63-65: IEEE.

[138] C. C. Gotlieb and H. E. Kreyszig, "Texture descriptors based on co-occurrence matrices," *Computer Vision, Graphics, and Image Processing*, vol. 51, no. 1, pp. 70-86, 1990.

[139] M. Sonka, V. Hlavac, and R. Boyle, *Image processing, analysis, and machine vision*. Cengage Learning, 2014.

[140] S. H. Peckinpaugh, "An improved method for computing gray-level cooccurrence matrix based texture measures," *CVGIP: Graphical models and image processing*, vol. 53, no. 6, pp. 574-580, 1991.

[141] R. M. Haralick and K. Shanmugam, "Textural features for image classification," *IEEE Transactions on systems, man, and cybernetics*, no. 6, pp. 610-621, 1973.

[142] A. Visioli, *Practical PID control*. Springer Science & Business Media, 2006.

[143] K. H. Ang, G. Chong, and Y. Li, "PID control system analysis, design, and technology," *IEEE transactions on control systems technology,* vol. 13, no. 4, pp. 559-576, 2005.

[144] S. Coxe, S. G. West, and L. S. Aiken, "The analysis of count data: A gentle introduction to Poisson regression and its alternatives," *Journal of personality assessment,* vol. 91, no. 2, pp. 121-136, 2009.

[145] M. Shahrokhi and A. Zomorrodi, "Comparison of PID controller tuning methods," *Department of Chemical & Petroleum Engineering Sharif University of Technology*, 2013.

[146] C.-C. Lee, "Fuzzy logic in control systems: fuzzy logic controller. II," *IEEE Transactions on systems, man, and cybernetics,* vol. 20, no. 2, pp. 419-435, 1990.

[147] R. S. Sutton and A. G. Barto, *Reinforcement learning: An introduction*. MIT press, 2018.

[148] S. J. Pan and Q. Yang, "A survey on transfer learning," *IEEE Transactions on knowledge and data engineering,* vol. 22, no. 10, pp. 1345-1359, 2009.